Aus dem

Laser-Forschungslabor der Laser-Immunologie-Forschungs-Einrichtung
(LIFE-Zentrum) an der Urologischen Klinik
Klinik der Universität München

Direktor: Prof. Dr. med. Christian Stief

Untersuchungen zur Standardisierung der Messung mikroskopischer Strukturen hinsichtlich Fluoreszenzlebensdauer und bildgebender Lumineszenz zur endoskopischen Anwendung

Dissertation
zum Erwerb des Doktorgrades der Humanbiologie
an der Medizinischen Fakultät der
Ludwig-Maximilians-Universität zu München

Vorgelegt von
Christian Freymüller
aus Straubing
2022

Mit Genehmigung der Medizinischen Fakultät
der Universität München

Berichterstatter:	Prof. Dr. rer. biol. hum. Ronald Sroka
Mitberichterstatter:	Prof. Dr. Andreas Leunig
	Prof. Dr. Reinhard Zeidler
Mitbetreuung durch den promovierten Mitarbeiter:	Dr. rer. nat. Adrian Rühm
Dekan:	Prof. Dr. med. Thomas Gudermann
Tag der mündlichen Prüfung:	06.12.2022

b

For **The Rest of the Family**

For **The Cat**

d

Inhaltsverzeichnis

f

1 Publikationsliste

Veröffentlichungen in begutachteten Fachmagazinen

- **C. Freymüller**, S. Ströbl, M. Aumiller, M. Eisel, R. Sroka und A. Rühm, "Development of a microstructured tissue phantom with adaptable optical properties for use with microscopes and fluorescence lifetime imaging systems", *Lasers in Surgery and Medicine*, S. 1–17, 2022, Publisher: John Wiley & Sons, Ltd. DOI: 10.1002/lsm.23556, JIF_{2021}: 4.025.
- T. Kellerer, J. Janusch, **C. Freymüller**, A. Rühm, R. Sroka und T. Hellerer, "Comprehensive investigation of parameters influencing fluorescence lifetime imaging microscopy in frequency- and time-domain illustrated by phasor plot analysis", *International Journal of Molecular Sciences*, Jg. 23, Nr. 24, 2022. DOI: 10.3390/ijms232415885, JIF_{2021}: 6.208.
- M. Aumiller, M. Eisel, C. Heckl, **C. Freymüller**, H. Stepp, R. Sroka und A. Rühm, "Investigations on the temperature dependence of optical tissue parameters in the range from 25°C to 50°C", *in Vorbereitung*, 2022.
- M. Aumiller, S. Quach, **C. Freymüller**, M. Foglar, M. El Fahim, K. Bochmann, R. Forbrig, H. Stepp, R. Sroka, J.-C. Tonn, N. Thon und A. Rühm, "MRI-based analysis of light dosimetry in 5-aminolevulinic acid mediated interstitial photodynamic therapy of maglignant gliomas with monte-carlo simulations", *In Vorbereitung*, 2022.
- S. Kalinina, **C. Freymüller**, N. Naskar, B. von Einem, K. Reess, R. Sroka und A. Rück, "Bioenergetic alterations of metabolic redox coenzymes as NADH, FAD and FMN by means of fluorescence lifetime imaging techniques", *International Journal of Molecular Sciences*, Jg. 22, Nr. 11, S. 5952, 31. Mai 2021. DOI: 10.3390/ijms22115952, JIF_{2021}: 6.208.
- **C. Freymüller**, S. Kalinina, A. Rück, R. Sroka und A. Rühm, "Quenched coumarin derivatives as fluorescence lifetime phantoms for NADH and FAD", *Journal of Biophotonics*, 8. Apr. 2021. DOI: 10.1002/jbio.202100024, JIF_{2021}: 3.390.
- M. Linek, A. Felicio-Briegel, **C. Freymüller**, A. Rühm, A. S. Englhard, R. Sroka und V. Volgger, "Evaluation of hyperspectral imaging to quantify perfusion changes during the modified allen test", *Lasers in Surgery and Medicine*, Jg. 54, Nr. 2, S. 245–255, 2022. DOI: https://doi.org/10.1002/lsm.23479, JIF_{2021}: 4.025.
- M. Eisel, F. Strittmatter, S. Ströbl, **C. Freymüller**, T. Pongratz und R. Sroka, "Comparative investigation of reusable and single–use flexible endoscopes for urological interventions", *Scientific Reports*, Jg. 10, Nr. 1, S. 5701, Dez. 2020, Test. DOI: 10.1038/s41598-020-62657-w, JIF_{2020}: 4.379.
- R. Sroka, N. Dominik, M. Eisel, A. Esipova, **C. Freymüller**, C. Heckl, G. Hennig, C. Homann, N. Hoehne, R. Kammerer, T. Kellerer, A. Lang, N. Markwardt, H. Pohla, T. Pongratz, C.-G. Schmedt, H. Stepp, S. Ströbl, K. Ulaganathan, W. Zimmermann und A. Ruehm, "Research and developments of laser assisted methods for translation into clinical application", *Frontiers of Optoelectronics*, Jg. 10, Nr. 3, S. 239–254, Sep. 2017. DOI: 10.1007/s12200-017-0724-6, JIF_{2017}: 0.92.

Veröffentlichungen in „Conference Proceedings“

- V. Volgger, A. Felicio-Briegel, **C. Freymüller**, A. Rühm, M. Linek und R. Sroka, “Investigation on hyperspectral imaging derived indices for perfusion monitoring ”, in *Translational Biophotonics: Diagnostics and Therapeutics*, Z. Huang und L. D. Lilge, Hrsg., International Society for Optics und Photonics, Bd. 11919, SPIE, 2021, S. 41–42. DOI: 10.1117/12.2614471.
- M. Linek, A. Felicio-Briegel, **C. Freymüller**, A. Rühm, R. Sroka und V. Volgger, “Investigation on hyperspectral imaging derived indices for perfusion monitoring”, in *Biophotonics Congress 2021*, Optica Publishing Group, 2021, OM1E.3. DOI: 10.1364/OMP.2021.OM1E.3.
- **C. Freymüller**, S. Kalinina, A. Rück, R. Sroka und A. Rühm, “Fluorescence lifetime phantoms based on quenched coumarin derivatives”, in *Advances in Microscopic Imaging III*, E. Beaurepaire, A. Ben-Yakar und Y. Park, Hrsg., International Society for Optics und Photonics, Bd. 11922, SPIE, 2021, S. 150–152. DOI: 10.1117/12.2615823.
- **C. Freymüller**, M. Eisel, S. Ströbl, A. Rühm und R. Sroka, “Investigations on thermography in laser medicine”, in *Clinical and Preclinical Optical Diagnostics II*, Optica Publishing Group, 2019, 11079_8. DOI: 10.1117/12.2527128.
- M. Aumiller, A. Rühm, M. Eisel, **C. Freymüller**, H. Stepp, A. Liemert, A. Kienle und R. Sroka, “Individualization of interstitial photodynamic therapy for malignant gliomas”, in *Clinical and Preclinical Optical Diagnostics II*, Optica Publishing Group, 2019, 11079_25. DOI: 10.1117/12.2527115.
- M. Aumiller, M. Eisel, C. Heckl, **C. Freymüller**, H. Stepp, R. Sroka und A. Rühm, “Investigation of changes of optical tissue properties up to 50°C”, in *Biophotonics Congress 2021*, Optica Publishing Group, 2021, JW1A.6. DOI: 10.1364/BODA.2021.JW1A.6.

Konferenzbeiträge

- Mündlicher Vortrag: **C. Freymüller**, T. Kellerer und J. Janusch, “Comparison of FLIM-techniques for metabolic imaging”, Sino-German Workshop, e-Congress, 19.01.2022.
- Poster: **C. Freymüller**, S. Kalinina, A. Rück, R. Sroka und A. Rühm, “Fluorescence lifetime phantoms based on quenched coumarin derivatives”, European Conferences on Biomedical Optics 2021 (ECBO) e-Congress, 20.-24.06.2021, Poster Session II, ETu2A.5.
- Mündlicher Vortrag: **C. Freymüller**, M. Eisel, S. Ströbl, A. Rühm und R. Sroka, “Investigations on thermography in laser medicine”, European Conference on Biomedical Optics 2019, Short Pulsed und Photothermal Applications II (SPPAII), 11079_8, 23.–25.06.2019, München, Deutschland.

Weitere Konferenzbeiträge als Koautor

- Mündlicher Vortrag: M. Aumiller, C. Heckl, S. Quach, M. Eisel, **C. Freymüller**, B. Ertl-Wagner, H. Stepp, N. Thon, R. Sroka und A. Rühm, "Investigation on Changes of Optical Tissue Properties related to iPDT on Malignant Gliomas", PD & PDT Update 2022; Nancy, Frankreich, 24.-28.10.2022.
- Mündlicher Vortrag: A. Rühm, **C. Freymüller**, N. Imberger, S. Kalinina, A. Rück und R. Sroka, "Optical tissue phantoms for 2-photon fluorescence lifetime imaging systems", 16th International conference on Laser Applications in Life Science (LALS), Nancy (France), online, 01-02 April 2022.
- Mündlicher Vortrag: V. Volgger, A. Felicio-Briegel, **C. Freymüller**, A. Rühm, M. Linek und R. Sroka, "Investigation on hyperspectral imaging derived indices for perfusion monitoring", in *European Conferences on Biomedical Optics 2021 (ECBO)*, Optica Publishing Group, 2021, EM3A.4. DOI: 10.1364/ECBO.2021.EM3A.4.
- Mündlicher Vortrag: M. Linek, A. Felicio-Briegel, **C. Freymüller**, A. Rühm, R. Sroka und V. Volgger, "Investigation on hyperspectral imaging derived indices for perfusion monitoring", in *Biophotonics Congress 2021*, Optica Publishing Group, 2021, OM1E.3. DOI: 10.1364/OMP.2021.OM1E.3.
- Mündlicher Vortrag: M. Aumiller, A. Rühm, M. Eisel, **C. Freymüller**, H. Stepp, A. Liemert, A. Kienle und R. Sroka, "Individualization of interstitial photodynamic therapy for malignant gliomas", in *Clinical and Preclinical Optical Diagnostics II*, Optica Publishing Group, 2019, 11079_25. DOI: 10.1117/12.2527115.
- Poster: M. Aumiller, M. Eisel, C. Heckl, **C. Freymüller**, H. Stepp, R. Sroka und A. Rühm, "Investigation of changes of optical tissue properties up to 50°c", in *Biophotonics Congress 2021*, Optica Publishing Group, 2021, JW1A.6. DOI: 10.1364/BODA.2021.JW1A.6.
- Poster: M. Aumiller, M. Eisel, C. Heckl, **C. Freymüller**, A. Rühm, H. Stepp und R. Sroka, "Investigations on the temperature dependence of optical tissue properties in the range of 20° to 50°C", PD & PDT Update 2020; eCongress, 05.-06.11.2020.

2 Abstract

Tumour cells usually have an altered metabolism compared to healthy cells, since irrespective of the availability of oxygen, they prefer to cover their energy requirements by glycolysis instead of the more efficient oxidative phosphorylation (OXPHOS) [1, 2, 3]. The transition from OXPHOS to glycolysis leads to a change in the ratio of free and protein-bound cofactors involved in complex I and II of the respiratory chain, namely nicotinamide adenine dinucleotide (NADH) and flavin adenine dinucleotide (FAD). These endogenous fluorophores are accessible by fluorescence imaging in their reduced (NADH) and oxidized (FAD) forms [4]. Due to the significant change in fluorescence lifetimes of the free and protein-bound forms of NADH and FAD, they are, in principle, suitable for obtaining information about the metabolic state of cells in vivo by means of fluorescence lifetime imaging microscopy (FLIM). However, clinical applications of FLIM are rare and only known in the field of dermatology [5], but they are frequently used in research [6, 7, 8, 9]. Two-photon excitation is preferable for this purpose, due to the longer excitation wavelength and thus increased optical penetration depth. The implementation of this technology in a clinical application requires both a validation of the measurement procedure and suitable artificial tissue phantoms as reproducible measurement objects.

The diagnosis of squamous cell carcinomas, which are predominant in the ear, nose, and throat (ENT) area, requires knowledge of the differentiation of the tumour from normal cells, as well as about the depth of infiltration. Furthermore the differentiation from inflammatory processes is essential. Current diagnostics are done by white light endoscopy and partly by narrow band imaging (NBI), less frequently by optical coherence tomography (OCT) or by fluorescence techniques. The latter three methods enable diagnosis via improved visualisation of structural tissue features compared to white light endoscopy. However, these methods do not provide information about the metabolic state. In the clinic, in addition to endoscopy, a biopsy and time-consuming tissue pathology are required for a systematic diagnosis.

By evaluating the fluorescence lifetimes of free and protein-bound NADH and FAD, a distinction between high-grade and low-grade tumours [6] or different cell types [7, 10] is possible. This evaluation procedure is called metabolic imaging.

Since tumours differ from normal tissue in their metabolism, it is possible to differentiate between the aforementioned tissue states by measuring the metabolic state of cells or tissue. The transfer of metabolic imaging to clinical diagnostics would offer immediate differentiation from inflammation sites, between high-grade and low-grade tumours or the infiltration of the basal membrane. This could be done during the clinical examination and would offer the possibility of a more exact determination of tumour margins. The analysis of the relative proportions of free and protein-bound NADH and FAD in the examined cell area are suitable for this. Four calculation methods of metabolic indices were compared to each other. The published NADH metabolic index [11, 9] (ratio of free to protein-bound NADH) and Fluorescence Lifetime Induced Redox Ratio (FLIRR, hereinafter referred to as FLIRR1, compares protein-bound and free NADH and FAD) [8, 9] were compared with two modifications of the FLIRR1 index, hereinafter referred to as FLIRR2 and FLIRR3, which take free FAD and additionally protein-bound flavin mononucleotide (FMN) into account [9]. By comparing the metabolic indices, a conclusion can be drawn about the

basic suitability of a calculation method for assessing the condition of cells or tissue. However, for development, characterisation and validation of metabolic imaging devices, artificial tissue phantoms showing on one hand side the optical properties of the target fluorophores as well as the optical properties of the target tissue on the other hand side are recommended including reproducible and controllable conditions. Since the optical parameters of tissue samples differ even within the same tissue type of the same species [12], controllable and reproducible optical properties are needed. This technical need can be provided by the development and subsequent use of artificial optical tissue phantoms [13].

In the course of the investigations, two artificial phantoms were developed serving two different requests: one to simulate the fluorescence lifetimes of free and protein-bound NADH and FAD, and one that allows the determination of the imaging depth and optical distortions or resolution of a device without z-stage by the use of fluorescent objects of known size.

Due to their chemical properties the substances NADH and FAD are only suitable as reference standards to a limited extent. This can be deduced also from the varying lifetime data available in literature [14, 15, 16, 17] and their dependence on the concentration [18] and the pH value [16]. Interestingly coumarin 1 and coumarin 6 have been identified as fluorophores with spectral properties sufficiently similar to those of NADH and FAD, thus their quenching properties have been investigated. Based on a modified Stern-Volmer equation, the required quencher concentrations to represent the fluorescence lifetimes of free and protein-bound NADH and FAD were calculated and experimentally tested in the case of coumarin 1. The stability of the coumarin 1 solution was tested over a period of 41 days. Fluorophore solutions based on coumarin 6 as a substitute for FAD were investigated in a cooperation with the Multiphoton Imaging Laboratory of the Munich University of Applied Sciences (AG Hellerer) [19].

In contrast to research microscopes, endoscopic systems in medicine are usually lacking the capability to precisely adjust the position of the object plane on the scale of the anatomical structures of the mucous membranes. Automatic focusing to a certain tissue depth is therefore not possible with a commercially available endoscope. For the application to metabolic imaging, an optical resolution in x, y, and z in the range of the size of mitochondria (approximately $1\,\mu m$ diameter) was aimed for. The challenge is that the substances usually involved in optical phantoms are of similar size [13].

The solution was a staircase-like structure, carved out of a glass body by laser microstructuring, beginning from the surface into the glass volume. With the stair-like structure, a depth range up to approximately $250\,\mu m$ in $5\,\mu m$ steps can be covered. The staircase structure was written into glass slides (n=10) by laser microstructuring and characterised in terms of step height, step length, surface texture and total depth. The tread surfaces where coated with fluorescent polystyrene microspheres of $1\,\mu m$ diameter. The carved out volume was filled with a substance with known reduced scattering coefficient μ_s' for the wavelengths $780\,nm$ and $880\,nm$, according to literature values [20] for the mucosa of human maxillary sinuses. For this cover layer, the concentration ratios of a hydrogel solution mixed with a suspension of non-fluorescent polystyrene microspheres as scattering centres were determined via an optimisation program, based on a published code [21, 22] for Mie scattering [23] calculations.

The performances of the artificial phantoms were characterised with a multiphoton FLIM

microscope and a confocal microscope with regard to the achievable imaging depth, distinguishability of the stairs and their long-time stability. Furthermore, images of the structured phantoms created with all used devices were compared.

The investigations carried out within the framework of the present dissertation showed the challenges as well as the limitations of phantoms for simulating the free and protein-bound states of the endogenous fluorophores NADH and FAD with a longterm-stability of more than 40 days. In addition, the manufacturing challenges as well as the limitations of a tissue mimicking phantom with the required x, y, z-resolution were investigated. By means of such a phantom, the maximum imaging depth as well as optical distortion effects could be comparatively examined on two different microscopy systems and an endoscopic system.
Based on these developments, protocols for the validation or comparison of dedicated microscope and endoscopic devices can be defined, in order to achieve comparability of reported results and device characteristics. Consequently, with regard to clinical application, the results of metabolic imaging may become more reliable, so that the value of this technique as a diagnostic tool can be further improved.

3 Zusammenfassung

Tumorzellen weisen in der Regel einen veränderten Stoffwechsel im Vergleich zu gesunden Zellen auf. Unabhängig von der Verfügbarkeit von Sauerstoff decken sie ihren Energiebedarf bevorzugt über Glykolyse und nicht über die effektivere oxidative Phosphorellierung (OXPHOS) [1, 2, 3]. Dieser Übergang von OXPHOS zu Glykolyse geht mit einer Änderung des Anteils der freien und proteingebundenen, am Komplex I und II der Atmungskette beteiligten, Kofaktoren Nicotinamidadenindinukleotid (NADH) und Flavin-Adenin-Dinukleotid (FAD) einher. Als endogene Fluorophore sind diese in ihrer reduzierten, NADH, und oxidierten, FAD, Form einer Fluoreszenzbildgebung zugänglich [4]. Da sich die Fluoreszenzlebensdauern der freien und proteingebundenen Formen von NADH und FAD signifikant ändern, ist deren Bestimmung über Fluoreszenzlebensdauer-Mikroskopie (Fluorescence Lifetime Imaging Microscopy, FLIM) grundsätzlich geeignet, um in vivo Informationen über den Stoffwechselzustand von Zellen zu erlangen. Jedoch findet FLIM gegenwärtig fast ausschließlich in der Forschung Anwendung [6, 7, 8, 9], eine klinische Anwendung in der Diagnostik ist selten und nur in der Dermatologie [5] bekannt. Aufgrund der höheren Eindringtiefe und Anregungswellenlängen im infraroten Spektralbereich ist eine Zwei-Photonen-Anregung hierfür vorzuziehen.

Die Translation dieser Technologie in eine klinische Anwendung erfordert sowohl eine Validierung des Messverfahrens als auch die Bereitstellung von geeigneten künstlichen Gewebephantomen als reproduzierbare Messobjekte. In der vorliegenden Arbeit erfolgt dies mit dem Ziel der endoskopischen Anwendung im HNO-Bereich, ist aber prinzipiell auf andere Gebiete übertragbar.
Bei der Diagnose der im HNO-Bereich dominierenden Plattenepithelkarzinome spielt die Kenntnis der Differenzierung der Tumorzellen sowie der Infiltrationstiefe und die Abgrenzung zu entzündlichen Prozessen eine entscheidende Rolle. Die gegenwärtige Diagnostik erfolgt primär über Weißlicht-Endoskopie und teilweise über Narrow-Band-Immaging (NBI), selten über Optical Coherence Tomography (OCT) oder über Fluoreszenzverfahren. Die letzteren drei Verfahren ermöglichen eine Diagnose über eine verbesserte Darstellung von Gewebestrukturen im Vergleich zur Weißlicht-Endoskopie. Diese Verfahren geben jedoch keinen Aufschluss über den Stoffwechselzustand einer Zelle. In der Klinik ist zusätzlich zur Endoskopie eine Biopsie und zeitaufwändige Gewebepathologie für eine fundierte Diagnose erforderlich. Durch die Auswertung der Fluoreszenzlebensdauern von freiem und proteingebundenem NADH und FAD konnte gezeigt werden, dass eine Unterscheidung sowohl zwischen verschiedenen Zelltypen [7, 10] als auch hochgradigen und niedriggradigen Tumoren prinzipiell möglich ist [6]. Dieses Auswerteverfahren wird als metabolische Bildgebung bezeichnet.

Der Vorteil einer Übertragung der metabolischen Bildgebung in die klinische Diagnostik läge darin, noch während der Untersuchung, eine Unterscheidung zwischen Normalgewebe, einer Entzündung und hochgradigem oder niedriggradigem Tumor zur ermöglichen, beziehungsweise Aussagen über eine Infiltration der Basalmembran treffen zu können. Zusätzlich würde sich die Möglichkeit der exakteren Bestimmung von Tumorrändern als es über eine Biopsie oder gegebenenfalls anderen optische Methoden möglich ist eröffnen. Da sich Tumore in ihrem Metabolismus von normalem Gewebe unterscheiden, ist über die Messung des metabolischen Zustands von Zellen beziehungsweise Gewebe grundsätzlich

eine Unterscheidung zwischen den vorgenannten Gewebezuständen möglich. Hierfür eignet sich die Bestimmung der relativen Anteile von freiem und proteingebundenem NADH und FAD im untersuchten Zellgebiet.
Es wurden vier Berechnungsverfahren von metabolischen Indizes untereinander verglichen. Die publizierten, als NADH Metabolic Index [11, 9] (setzt den Anteil von freiem zu proteingebundenem NADH ins Verhältnis) und Fluorescence Lifetime Induced Redox Ratio [8, 9] (FLIRR; im Folgenden FLIRR1 genannt; setzt proteingebundenes und freies NADH und FAD ins Verhältnis) bekannten Berechnungsverfahren wurden mit zwei Abwandlungen des FLIRR1-Indices, im folgenden FLIRR2 und FLIRR3 genannt, welche freies FAD und zusätzlich proteingebundenes Flavinmononukleotid (FMN) berücksichtigen [9], verglichen.
Durch den Vergleich der metabolischen Indices kann eine Aussage über die grundsätzliche Eignung eines Berechnungsverfahrens zur Bewertung des Zustandes von Zellen oder Gewebe getroffen werden. Diese Erkenntnis alleine ist jedoch nicht für die Entwicklung, Charakterisierung und Validierung eines Gerätes ausreichend.
Da sich die optischen Parameter von Probengeweben, auch innerhalb desselben Gewebetyps und der selben Spezies, unterscheiden [12], werden kontrollierbare und wiederholbare Eigenschaften, wie sie artifizielle Gewebephantomen zur Verfügung stellen, benötigt [13]. Dies wird in der Regel durch die Nutzung von künstlichen (optischen) Gewebephantomen sichergestellt. Im Rahmen der Untersuchungen wurden zwei, unterschiedliche Zwecke erfüllende, künstliche Phantome entwickelt: Eines zur Simulation der Fluoreszenzlebensdauern von freiem und proteingebundenem NADH und FAD und eines, welches über fluoreszierende Objekte bekannter Größe, die Bestimmung der Bildgebungstiefe und gegebenenfalls optischer Verzerrungen oder der Auflösung eines Gerätes ohne z-Stage erlaubt.

Die Substanzen NADH und FAD sind nur bedingt als Referenzstandard geeignet, da die in der Literatur angegebenen Werte zur Fluoreszenzlebensdauer zum Teil erheblich schwanken [14, 15, 16, 17]. Außerdem besteht eine Abhängigkeit der Fluoreszenzlebensdauer von der Konzentration [16] und dem pH-Wert [18]. Coumarin 1 und Coumarin 6 wurden als Fluorophore mit monoexponentiellem Abklingverhalten und hinreichend ähnlichen spektralen Eigenschaften zu NADH und FAD identifiziert und ihre Quencheigenschaften untersucht.
Auf der Basis einer modifizierten Stern-Volmer-Gleichung wurden die notwendigen Quencherkonzentrationen, um die Fluoreszenzlebensdauern von freiem und proteingebundenem NADH und FAD nachzustellen, ermittelt und im Falle von Coumarin 1 als Substituat für NADH getestet. Weiterhin wurde die Stabilität der Coumarin 1 Lösungen für einen Zeitraum von 41 Tagen verifiziert.
Die auf Coumarin 6, als Substituat für FAD, basierenden Fluorophorlösungen wurden im Rahmen einer Kooperation mit dem Multiphoton Imaging Labor der Hochschule München (AG Hellerer) für angewandte Wissenschaften untersucht [19].
Im Gegensatz zu Forschungsmikroskopen verfügen endoskopische Systeme in der Medizin in der Regel nicht über die Möglichkeit zur präzisen Verstellung der Position der Objektebene in der Größenordnung der anatomischen Strukturen der Schleimhäute. Eine automatische Fokussierung in eine gewisse Gewebetiefe ist mit einem handelsüblichen Endoskop nicht möglich.

Für die Anwendung zur metabolischen Bildgebung wurde ein Auflösungsvermögen im Bereich der Größe von Mitochondrien (ca. 1 μm Durchmesser) angestrebt. Damit ist die optische Auflösung des zu untersuchenden Gerätes in der Größenordnung der, in der Regel in optischen Phantomen eingesetzten Substanzen, um Streuung kontrolliert zu erzeugen [13].
Mit dem Ziel ein Phantom zu entwickeln, welches sowohl mit einem Forschungsmikroskop als auch mit einem Endoskopsystem verwendet werden kann, wurde in einen Glaskörper eine treppenartige Struktur von der Oberfläche aus in das Glasvolumen hineingearbeitet. Mit dieser treppenartigen Struktur kann ein Tiefenbereich bis ca. $250\mu m$ in $5\mu m$ Schritten abgedeckt werden. Die Treppenstruktur wurde mittels Laser-Mikrostrukturierung in Glas-Objektträger (n=10) geschrieben und hinsichtlich der Stufenhöhe, Stufenlänge, Oberflächenbeschaffenheit und Gesamttiefe charakterisiert.
Fluoreszierende Strukturen wurden durch eine Beschichtung der Treppenstufenflächen mit fluoreszierenden Polystyrene Microspheres von 1 μm Durchmesser erzeugt. Das herausgearbeitete Volumen wurde später mit einer Substanz mit bekanntem reduziertem Streukoeffizienenten μ_s' für die Wellenlängen $780\,nm$ und $880\,nm$ aufgefüllt. Für diese Deckschicht wurden die Konzentrationsverhältnisse einer Hydrogellösung mit einer Suspension nicht fluoreszierenden Polystyrene Microspheres als Streuzentren über ein Optimierungsprogramm basierend auf einem publizierten Code [21, 22] zur Berechnung von Mie-Streuung [23] nach Literaturwerten [20] für die Schleimhaut der humanen Kieferhöhlen bestimmt.
Die künstlichen Phantome wurden mit einem Multiphotonen-FLIM-Mikroskop und einem Konfokalkmikroskop hinsichtlich der erreichbaren Bildgebungstiefe, Unterscheidbarkeit der Stufen und ihrer Alterungsstabilität charakterisiert. Weiterhin wurden Aufnahmen eines der Phantome mit einem modifizierten FLIM-Tomographen [24] (MPTFlex, Jenlab GmbH, Berlin), an welchen ein Mikro-Endoskop adaptiert wurde, mit den Aufnahmen der beiden Mikroskopsysteme verglichen.

Die im Rahmen der vorliegenden Dissertation durchgeführten Untersuchungen zeigten die Fertigungsmöglichkeiten und Limitationen von Phantomen zur Simulation der freien und proteingebundenen Zustände der endogenen Fluorophore NADH und FAD. Die Phantome blieben, im Gegensatz zu NADH und FAD Lösungen, über einen Zeitraum von mehr als 40 Tagen stabil. Mittels eines Zweiten, durch Laser-Mikrostrukturierung erzeugten künstlichen Gewebephantoms, konnten Verzeichnungseffekte, sowie maximale Bildgebungstiefe, auch im Vergleich zwischen zwei unterschiedlichen Mikroskopiesystemen und einem endoskopischen System, analysiert werden.
Zusammenfassend konnte mit den durchgeführten Untersuchungen und Entwicklungen ein wesentlicher Beitrag für Vergleichs- und Validierungsverfahren von bildgebenden Systemen in der Biophotonik geleistet werden.

4 Untersuchungen zur Standardisierung der Messung mikroskopischer Strukturen hinsichtlich Fluoreszenzlebensdauer und bildgebender Lumineszenz zur endoskopischen Anwendung

Die präsentierte Arbeit wird als kumulative Dissertation bestehend aus drei publizierten Originalmanuskripten bei der medizinischen Fakultät der Ludwig-Maximilians-Universität zu München eingereicht. Die Manuskripte beinhalten Untersuchungen zu Designmöglichkeiten und zur Entwicklung von künstlichen Fluoreszenz-Gewebephantomen, sowie zur metabolischen Bildgebung. Diese artifiziellen Phantome sollen sowohl für die Charakterisierung von Mikro-Endoskopischen Fluoreszenz-Lebensdauer-Messsystemen als auch von Forschungsmikroskopen Anwendung finden.
Die Arbeit entstand im Rahmen des Forschungsprojektes OMOXI [25]. Ziel von OMOXI war es, eine existierende Technologie zur Fluoreszenzlebensdauer-Messung in der Dermatologie [5, 24] endoskopisch für den Bereich des Rachens und Kehlkopfes nutzbar zu machen. Übergeordnetes Ziel ist eine Verbesserung der Diagnostik und Therapie. Um dies zu ermöglichen sollte das vorhandene System um ein neu zu entwickelndes Endoskop und der Möglichkeit zur metabolischen Bildgebung erweitert werden. Für die Entwicklung und Testung eines solchen Gerätes sind geeignete Referenzmaterialien und optische Gewebephantome notwendig, um reproduzierbare, vergleichbare Messbedingungen sicherstellen zu können [13].
Die Entwicklung und Validierung eines geeigneten Verfahrens zur Berechnung von metabolischen Indizes erfolgte in Zusammenarbeit mit der AG Rück der Core Facility Konfokale und Multiphotonen Mikroskopie der Universität Ulm. Im Rahmen der Kooperation wurden an Monokulturen und Kokulturen von HaCaT (immortalized keratinocyte) und SCC4 (human oral squamous carcinoma) Zellen Fluoreszenzlebensdauermessungen an NADH und FAD durchgeführt. Es wurden verschiedene publizierte Berechnungsverfahren von metabolischen Indices anhand der Messungen an HaCaT und SCC4 Zellen mit neu entwickelten Indices verglichen. Darüber hinaus wurden auf Basis der verglichenen Algorithmen aus mikroskopischen FLIM-Aufnahmen der Zellen Falschfarb-2D-Bilder der metabolischen Indices erzeugt und deren visuelle Erscheinung verglichen.
Für die metabolische Bildgebung, die mit der Arbeit von Britton Chance et.al [26] ihren Anfang nahm, sind die endogenen Fluorophore NADH und FAD relevant. Diese Fluorophore sind aufgrund ihrer Eigenschaften in Lösung nur bedingt als Referenz für die Charakterisierung eines Fluoreszenzlebensdauer-Messsystems geeignet, da die in der Literatur angegebenen Werte zur Fluoreszenzlebensdauer zum Teil erheblich schwanken.
Die angegebenen Werte zur Fluoreszenzlebensdauer, in vitro und in Lösung, für freies NADH schwanken zwischen ca. $140\,ps - 2400\,ps$ [27, 28, 29, 30, 17] und für FAD zwischen ca. $2000\,ps - 2820\,ps$ [31, 14, 32, 6, 16, 30]. Ebenso unterscheidet sich in der Literatur, für NADH bis zu drei [17] und für FAD bis zu fünf [14, 15, 16], die Anzahl von angefitteten Exponentialkomponenten. Zusätzlich ist eine Abhängigkeit der Fluoreszenzlebensdauern vom pH-Wert und der Konzentration bekannt [18, 16].
Die generelle Empfehlung für die Eigenschaften eines Fluoreszenzlebensdauer-Standards beinhaltet jedoch monoexponentielles Abklingverhalten [4, 33]. Um diesem Umstand zu begegnen, wurden auf Coumarin-Derivaten basierende künstliche Phantome, welche die

spektralen und zeitlichen Fluoreszenzeigenschaften von NADH und FAD nachbilden, entwickelt. Hierzu wurden Coumarin 1 und Coumarin 6 als geeignet identifiziert, ihre Fluoreszenzeigenschaften (spektral und temporal) untersucht und mittels eines Quenchers (4-Hydroxy-TEMPO) an die Fluoreszenzlebensdauern von NADH und FAD in ihrer freien und proteingebundenen Form angepasst.
Ziel des Projektes ist die Übertragung der metabolischen Bildgebung von der Zellkultur in die medizinische Diagnostik und damit die Messung an Gewebe. Deshalb wurde ein künstliches Gewebephantom entwickelt und charakterisiert. Das entwickelte Gewebephantom eignet sich zum Vergleich von endoskopischen Systemen die nicht, wie bei einem Forschungsmikroskop üblich, über eine integrierte Einrichtung zum Positionieren in x,y und z-Richtung (Stage) verfügen.
Hierzu wurde eine mittels Laser mikrostrukturierte Glasoberfläche mit fluoreszierenden Polystyrene Microspheres von 1 μm Durchmesser beschichtet und mit einer Suspension mit bekannten optischen Eigenschaften (Streuung, Absorption), bestehend aus nicht fluoreszierenden Polystyrene Microspheres in einem Hydrogel bedeckt und mit einem Deckglas versiegelt. Die Mikrostrukturierung erlaubt die Bestimmung der Tiefe innerhalb des künstlichen Gewebephantoms aus welcher ein Bild erzeugt wird. Durch die regelmäßige Struktur sind Aussagen über die mit einem bestimmten System erreichbare Tiefe, über die Abbildungsqualität des untersuchten optischen Systems sowie ein Vergleich verschiedener Systeme untereinander, z.B. zwischen einem Mikroendoskop für den in vivo Einsatz und einem Forschungsmikroskop, möglich.

4.1 Tumore des Hals- Rachen-Raumes

Bei Tumoren der Mundhöhle und des Rachenraumes, ICD-10 C00-C14 [34] sowie des Kehlkopfes (Larynxkarzinom), ICD-10 C32 [34], handelt es sich zumeist [35] um maligne Neubildungen. In Mundhöhle und Rachenraum handelt es sich in den meisten Fällen um (von den Naso-, Oro- und Hypopharynx-Schleimhäuten ausgehende) Plattenepithelkarzinome [34, 36] (Squamous cell carcinoma of the head and neck (SCCHN)[37]) und in seltenen Fällen (ca. 3%) um Adenokarzinome, welche jedoch primär die Speicheldrüsen betreffen [34]. Im Bereich des Kehlkopfes treten nahezu ausschließlich Plattenepithelkarzinome [34] auf. Die wichtigsten Risikofaktoren, sowohl im Bereich Mundhöhle und Rachen-Raum als auch beim Kehlkopf, stellen alle Formen des Tabak- und Alkoholkonsums dar [34, 36, 37, 38]. Infektionen mit humanen Papillomaviren (HPV) gelten als ein weiterer Risikofaktor für die Bildung von malignen Neoplasien im Bereich des Oropharynx (Mundrachen) [34, 37] und geringgradig auch im Kehlkopfbereich [34]. Die Faktoren Alkohol- und Tabakkonsum können sich, wenn sie zusammentreffen, verstärken und andere Faktoren (berufliche Exposition zu Stäuben, ionisierende Strahlung, Teerprodukte, etc.) gegebenenfalls überlagern [34].
Insgesamt erkranken Männer häufiger an Tumoren in der Mundhöhle, dem Rachen und dem Kehlkopf als Frauen [34, 38, 36]. Die weltweite Inzidenz für SCCHN im Jahr 2018 betrug ca. 700.000 mit einer angenommenen Sterberate von 350.000 [37]. Die Inzidenz für Neuerkrankungen im Bereich Mundhöhle und Rachen lag in Deutschland im Jahr 2018 bei 10,7/100.000 für Frauen und 24,0/100.000 für Männer mit einem mittleren Erkrankungsalter für Frauen von 66 und Männern von 64 Jahren [34] und stellen damit die 7. häufigste maligne Tumorerkrankung bei Männern dar [36]. Die 5-Jahres-Überlebensrate

ist bei Frauen mit 55% etwas höher als mit 46% bei Männern [36]. Beim Larynxkarzinom, dem dritthäufigsten bösartigen Tumor im Kopf-Hals-Bereich [39], unterscheiden sich die Inzidenzen mit 1,3/100.000 bei Frauen und 6,8/100.000 bei Männern im Jahr 2018 erheblich [34]. Im Vergleich zu 2016 war die Inzidenz bei Männern leicht rückläufig (8,0/100.000), wohingegen sie bei den Frauen weitgehend unverändert blieb (1,4/100.000) [38]. Das mittlere Erkrankungsalter 2018 lag bei 66 Jahren bei Frauen und 67 Jahren bei Männern und die absolute 5-Jahres-Überlebensrate bei Frauen bei 59% und 56% bei Männern [34]. Da die Behandlung von Tumorvorstufen und Tumorfrühstadien die Heilungsaussichten verbessern kann, ist eine Früherkennung von Bedeutung [39, 40].

4.2 Diagnostik

Plattenepithelkarzinome im Bereich der Mundhöhle, des Rachens oder Kehlkopfes, können sich durch unspezifische und sich zum Teil überschneidende Symptome wie Schluckbeschwerden, Heiserkeit, Schwierigkeiten beim Sprechen, Fremdkörpergefühl, Schwellungen im Halsbereich oder Leukoplakien (weißliche Auflagerung/Läsion der Schleimhaut die eine Präkanzerose darstellen kann) [37, 39, 40] bemerkbar machen. Bestehen diese Symptome länger als zwei [40] beziehungsweise vier Wochen [39] wird eine Untersuchung durch einen Facharzt zur weiteren Abklärung empfohlen, um eine Verwechslung mit z.B. einer Parodontitis, Lymphadenitis [40] oder einer Laryngitis [39] auszuschließen.
Die Untersuchung des Kehlkopfes erfolgt endoskopisch. Diese kann entweder mit einem starren Endoskop über die Mundhöhle oder mit einem flexiblen Rhino-Laryngoskop über die Nase erfolgen [39]. Bei begründetem Karzinomverdacht sollte eine Panendoskopie erfolgen. Diese dient sowohl der Diagnosesicherung (Probebiopsie mit anschließender histopathologischer Untersuchung) als auch der Ausdehnungsdiagnostik für die folgende Therapieplanung. Zudem dient die Panendoskopie auch zum Ausschluss eines simultanen Zweitkarzinoms.
Neben dem Goldstandard, der Panendoskopie mit Probebiopsie und anschließender histopathologischer Untersuchung, haben in den letzten Jahrzehnten endoskopische Verfahren wie Narrowband-Imaging (NBI) [41, 42, 43], Chromoendoskopie [44], Autofluoreszenz-Endoskopie [45, 46], endoskopische optische-Kohärenztomographie (OCT) [47, 48, 39] sowie die Konfokale-Endomikroskopie [49, 50] zunehmend Anwendung gefunden.
Eine weitere Bildgebung erfolgt in der Regel in Form von Magnet-Resonanz-Tomographie (MRT), Computer-Tomographie (CT) oder Positronen-Emissions-Tomographie (PET) zur Bestimmung der Ausdehnung und Lage des Tumors [39, 40], sowie zum Ausschluss von Fernmetastasen. Die Einteilung des Tumors (Staging) nach seiner Ausdehnung erfolgt auf der Basis der klinischen Untersuchung und der Bildgebung anhand der UICC-TNM-Classification of malignant tumors [39, 40, 51]. Hierbei beschreibt T (=Tumor) die Größe und Ausbreitung des Tumors, N (=Nodes) das Vorliegen von Lymphknotenmetastasen und M (=Metastasis) die Existenz von Fernmetastasen [51]. An den tumorverdächtigen Stellen wird in der Regel eine Gewebeprobe (Biopsie) entnommen und histopatholgisch zur Bestimmung der Entität und Differenzierung G (=Grading) des Tumorgewebes untersucht. Je Histologie und lokoregionärer Ausdehnung des Tumors sowie dem Zustand des Patienten ergeben sich als Behandlungsmöglichkeiten die chirurgische Resektion, die Strahlentherapie, gegebenenfalls in Kombination mit einer Chemotherapie, beziehungsweise die Kombinationen dieser Verfahren [39, 40].

In der Diagnostik und Therapie von Neoplasien in der Mundhöhle und im Rachenraum, vor allem jedoch im Larynx-Bereich, spielen endoskopische Methoden, als etablierte Verfahren im medizinischen Bereich [52, 53], eine bedeutende Rolle. In den meisten Fällen handelt es sich hierbei um Weißlicht-Endoskopie [54]. Es ist jedoch zur Therapievorbereitung eine Biopsie mit histologischer Untersuchung vorteilhaft, da über endoskopische Verfahren alleine in der Regel eine Unterscheidung zum Beispiel zwischen entzündlichen Prozessen oder einer malignen Neoplasie schwierig ist. Zudem können keine ausreichenden Informationen über Ausdehnung, Infiltrationstiefe und vor allem den Differenzierungsgrad von Tumorzellen gewonnen werden. Eine histopathologische Untersuchung bedeutet teilweise einen erheblichen Zeitaufwand und geht mit einem zeitlichen Abstand zwischen Endoskopie und Diagnosestellung einher [55]. Um diesen Zeitaufwand und zeitlichen Abstand zu verringern gibt es Bestrebungen mehr als die mit Weißlicht-Endoskopie alleine zugänglichen Informationen zu erhalten. Ansatzmöglichkeiten hierfür sind zum Beispiel eine Verbesserung der Farbkontraste zur Sichtbarmachung von Oberflächenstrukturen, morphologische Eigenschaften von Gefäßen, Darstellung biochemischer Eigenschaften, gewebespezifische Fluoreszenz und ähnliches.
Verfahren mit dem Ziel eine Diagnosestellung bereits in vivo und ohne Biopsie und histopathologische Untersuchung während der Endoskopie zu ermöglichen werden als optische Biopsie bezeichnet [55]. Sie sind Gegenstand der aktuellen Entwicklung, Studien zur Validierung und Etablierung sind Gegenstand aktueller Forschung [56, 57].

Es lassen sich grundlegend verschiedene Typen von Endoskopieverfahren anhand von Beispielen wie folgt unterscheiden: Eine Verbesserung des Kontrastes oder der Hervorhebung von Oberflächenstrukturen hat beispielsweise die Chromoendoskopie zum Ziel. Hierbei wird die zu untersuchende Schleimhaut mit einem Farbstoff, zum Beispiel eine Jod-Lösung oder Indigocarmin [44, 58], benetzt, um so die Schleimhautstruktur kontrastreicher darzustellen.
Eine weitere Möglichkeit stellt das NBI dar [49]. Im Gegensatz zur Weißlicht-Remission werden beim NBI zwei schmalbandige Wellenlängenbereiche im blauen, $(415 \pm 15)\,nm$, und grünen, $(540 \pm 15)\,nm$, Spektralbereich für die Beleuchtung genutzt [49, 54]. Diese liegen in den Absorptionsbereichen von Hämoglobin zwischen $400\,nm - 430\,nm$ und $540\,nm - 580\,nm$ [59]. Durch die erhöhte Absorption von Hämoglobin in den Gefäßen gegenüber dem umliegenden Gewebe wird der Kontrast so erhöht, dass die Gefäße gegenüber dem umliegenden Gewebe dunkler erscheinen [49, 54]. Die optischen Eindringtiefen für Licht der Wellenlängen $415\,nm$ und $540\,nm$ in Schleimhaut sind unterschiedlich, am Beispiel der menschlichen Kieferhöhlenschleimhaut ca. $400\,\mu m$ und ca. $1000\,\mu m$ [60] für die genannten Wellenlängen, wodurch die Kapillaren unterschiedlicher Gewebetiefen differenziert dargestellt werden können. Eine Beurteilung der Neoplasie und deren Ausmaß sowie des Grads der Malignität erfolgt über die Morphologie der Gefäßstrukturen. Durch die Nutzung der Hämoglobin-Absorptionsbereiche sind Gefäßneubildungen, sowie die Ausprägung von charakteristischen Kapillarschlingen, den Intraepithelial Papillary Capillary Loops (IPCL), hervorgehoben [61, 62, 54].

Fluoreszenztechniken eignen sich ebenfalls, um zusätzliche Informationen über die endoskopisch untersuchten Bereiche zu erlangen [49].
Bei der Autofluoreszenz-Endoskopie werden intrinsische Fluorophore wie z.B. Elastin, Keratin, Porphyrine, NADH und FAD [49] mit blauem Licht (Wellenlängenbereich $375\,nm$

bis 440 nm [49, 45]) angeregt. Dies führt bei gesunder Schleimhaut zu einer grünen Fluoreszenz mit einem Fluoreszenzmaximum bei einer Wellenlänge von 511 nm [45] bis 515 nm [63]. Eine Verdickung der Epithelschicht, wie bei einer beginnenden Neoplasie, kann durch erhöhte Absorption von Anregungs- und Fluoreszenz-Licht, zu einer Reduktion der Fluoreszenzintensität führen und die Neoplasie erscheint dunkler als das umgebende Gewebe oder, je nach Ausprägung, gegebenenfalls rosa oder rötlich [45, 64].
5-Aminolävulinsäure (5-ALA) induzierte Protoporphyrin IX (PPIX) Fluoreszenz ist eine weitere Methode zur Fluoreszenz-Diagnostik [49]. Hierzu wird vor der Untersuchung eine 5-ALA Lösung auf die zu untersuchende Schleimhaut appliziert. Dies führt zu einer Akkumulation von PPIX in neoplastischen Zellen [65]. Bei einer anschließenden Endoskopie mit Anregungslicht im Wellenlängenbereich von 375 nm bis 400 nm zeigen so angefärbte neoplastische Bereiche eine rötliche PPIX Fluoreszenz [65]. Ursprünglich für die Harnblasendiagnostik entwickelt [66, 67, 68], wird diese Methode nun in andere Fachbereiche übertragen.
Interferenztechniken bzw. mikroskopische Techniken ermöglichen es, aus unterschiedlichen Gewebetiefen morphologische Informationen zu erhalten. Hier spielen vor allem die auf Interferenz basierende OCT und die sondenbasierte Endo-Konfokalmikroskopie eine Rolle [39]. OCT erlaubt die in vivo 3D-Darstellung von Gewebe mit einer Auflösung von ca. 10 μm [47, 69] aus Tiefen von bis zu 3 mm in streuendem Gewebe [70], und findet hauptsächlich in der Ophtalmologie [71] Anwendung. Anwendungen der OCT in der HNO sind in der Validierungsphase [56, 72, 73, 74]. Konfokale Endomikroskopie [75, 57, 50], welche die Funktionalität eines Konfokalmikroskopes über eine Sonde zusammen mit einem Endoskop nutzbar macht, findet ebenfalls in der klinischen Forschung Anwendung. Die oben genannten Verfahren geben in der Regel morphologische Aufschlüsse und keine oder beschränkt biochemische Information über das untersuchte Gewebe. Mit der im HNO-Bereich bereits genutzten Konfokalen-Endomikroskopie sind beschränkt Informationen über die Differenzierung von Tumorzellen und damit zur Malignität zugänglich [57, 49, 76].
Zusätzliche diagnostisch relevante Informationen lassen sich mittels optischer Methoden aus der Kenntnis des Zellstoffwechsels gewinnen. Hierzu ist jedoch eine spezifische Färbung des Gewebes notwendig, was einen zusätzlich invasiven Prozess bedeutet, bei welchem auf die Biokompatibiltät der Farbstoffe zu achten ist. Alternativ können in den Stoffwechselprozess der Zellen involvierte fluoreszierende Stoffwechselprodukte, wie beispielsweise NADH und FAD, genutzt werden [6, 8, 9]. Ein auf Zwei-Photonen-Fluoreszenzlebensdauer-Mikroskopie basierendes Verfahren [5] ist in der Dermathologie zugelassen und dient als Plattform (MPTFlex [24]) für die Untersuchung der Übertragbarkeit in ein endoskopisches System für den HNO-Bereich.

4.3 Fluoreszenzlebensdauer intrinsischer Fluorophore

Im Vergleich zu Normalgewebe zeigen Tumorzellen in der Regel eine Veränderung in ihrem Glukose-Stoffwechsel der als Warburg-Effekt bekannt ist [1]. Sie betreiben, unabhängig von der Verfügbarkeit von Sauerstoff, bevorzugt die ineffektivere Glykolyse anstatt der oxidativen Phosphorylierung (OXPHOS) zur Energiegewinnung [1, 2]. Ob dieses geänderte Verhalten Ursache oder Folge der Tumorentwicklung ist, wird bis in die Gegenwart unterschiedlich diskutiert [77, 78, 79, 80].

Die in den Komplexen I und II der Atmungskette involvierten Koenzyme NADH und FAD zeigen eine relative starke Änderung, im Bereich von ca. 2 ns, der jeweiligen Fluoreszenzlebensdauer in Abhängigkeit ob sie frei oder proteingebunden vorliegen [6, 81, 9]. Eine Verschiebung des Fluoreszenzspektrums, im Falle von NADH eine Blauverschiebung um ca. 10 nm zwischen freiem und proteingebundenem NADH [82], ist im Vergleich zur Veränderung der Fluoreszenzlebensdauer schwer zu bestimmen [11]. Für FAD ist eine Verschiebung des Fluoreszenzspektrums nicht dokumentiert [83], eine Unterscheidung zwischen der freien und proteingebundenen Form ist nur über die Fluoreszenzlebensdauer möglich [81, 9].

Bei vermehrter Glykolyse ist eine Erhöhung des Anteils von freiem NADH, bei vermehrter oxidativer Phosphorylierung eine Erhöhung des gebundenen NADH und FAD Anteils in Zellkulturen messbar [84]. Die genaue Rolle und das Verhalten von FAD ist nicht eindeutig geklärt und Gegenstand aktueller Diskussion [9]. Widersprüchlich erscheinende Aussagen könnten in der (unabsichtlichen) Einbeziehung von FMN begründet sein [9], welches im selben Spektralbereich wie FAD fluoresziert [85], jedoch eine längere Fluoreszenzlebensdauer als FAD aufweist [9]. Es konnte gezeigt werden, das über die Änderung der Verhältnisse der freien und proteingebundenen Fluorophore NADH und FAD eine Unterscheidung zwischen normalen Zellen und Tumorzellen in Zellkulturen [9] und im Tiermodell möglich ist [6, 86, 87, 88].
Die Bestimmung der Fluoreszenzlebensdauer kann mit zwei Methoden erfolgen. Bei der Frequency Domain (FD) Methode erfolgt die Anregung mit einer, beispielsweise sinusförmig, in der Intensität modulierten Lichtquelle, vorzugsweise einem Laser, und es wird die Amplitude und Phasenlage des Fluoreszenzsignals jeweils relativ zur Anregung gemessen. Aus der Phasenlage und Amplitude kann dann die Fluoreszenzlebensdauer bestimmt werden [89]. Zur Diskussion von Vor- und Nachteilen dieser und der nachfolgend beschriebenen Methode wird auf die Literatur verwiesen [81, 90].
Die zweite und in der vorliegenden Arbeit verwendete Methode ist die zeitkorrelierte Einzelphotonenzählung (Time-Correlated Single Photon Counting, TCSPC) [91] welche in ein konfokales Laser-Scan-Mikroskop integriert werden kann [92, 93]. Hierbei erfolgt die Fluoreszenzanregung mit Ein-Photonen-Anregung oder mit Zwei-Photonen-Anregung über einen Ultrakurzpuls-Laser mit einer Pulsdauer kleiner 100 ps. Die Repetitionsrate ist dabei in beiden Fällen üblicherweise 80 MHz. Eine geeignete Kombination aus Detektor und Messelektronik bestimmt den Zeitabstand zwischen dem Anregungspuls und dem ersten am Detektor eintreffenden Fluoreszenzphoton. Dies wird für jedes Pixel des aufzunehmenden Bildes viele Male wiederholt und für jedes Pixel die Zeitdifferenz zwischen den Anregungspulsen und den ankommenden Photonen gespeichert, sodass ein Histogramm Ankunftszeit vs. Photonenzahl entsteht [93]. Da der Anregungspuls $E(t)$ als Funktion der Zeit t nicht infinitesimal kurz ist, stellt er keine δ-Distribution [91] dar. Auch der Detektor sowie die zugehörige Elektronik weisen keine infinitesimal kurzen Reaktionszeiten auf. Die sich ergebende Summe der elektronischen und optischen Charakteristiken des Messsystems, der sogenannten Instrumental Response Function (IRF), kann somit als die Übertragungsfunktion $H(t)$ des Messsystems verstanden werden [91]. Die gemessene Abklingkurve $I_F(t)$ ist daher die Faltung des originalen Abklingverhaltens $I_0(t)$ des vermessenen Fluorophors mit der IRF. Die IRF kann entweder gemessen [94, 93] oder aus

den Abklingkurven synthetisiert werden [93]. Durch eine Entfaltungsoperation der Zeitverläufe jedes Pixels mit der IRF kann annähernd das ursprüngliche Abklingsignal $I(t)$ zurückgewonnen werden [94, 95, 96, 93, 97]. In Abbildung 1 ist der Verlauf der Abklingkurven vereinfacht für eine kurze, τ_1, und eine lange, τ_2, Abklingzeit mit verschiedenen Amplituden a_1 und a_2 und die Überlagerung $I_{\tau_1/\tau_2}(t) = I_{\tau_1}(t) + I_{\tau_2}(t)$ der kurzen und langen Abklingzeit ohne Faltung mit einer IRF dargestellt.

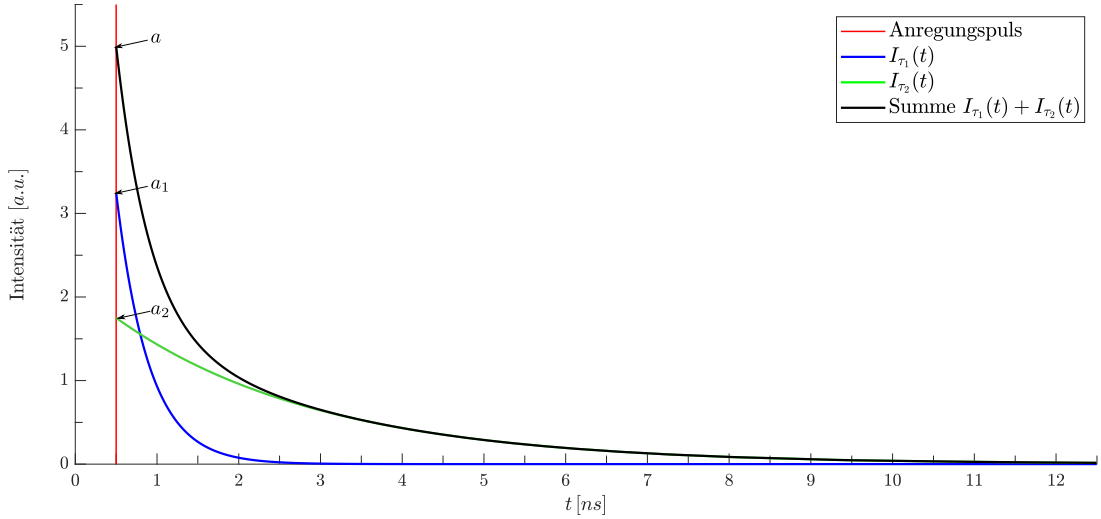

Abbildung 1: Schematische Darstellung von Abklingkurven und deren Überlagerung, ohne Faltung mit IRF; kurze Abklingzeit τ_1 mit Amplitude a_1 und lange Abklingzeit τ_2 mit Amplitude a_2 sowie die Überlagerung (Summe) $I_{\tau_1/\tau_2}(t) = I_{\tau_1}(t) + I_{\tau_2}(t)$; Fluoreszenzanregung bei $t = 0{,}5\,ns$

Die Bestimmung der Fluoreszenzlebensdauer(n) τ_i und der anteiligen Amplitude(n) a_i erfolgt durch die mathematische Anpassung einer Fitfunktion, bestehend aus einer oder mehreren Exponentialfunktionen, der in Gleichung (1) beschriebenen Form [91, 93, 9] an die Abklingkurve $I(t)$,

$$I\,(t) = \sum_{i=1}^{n} a_i e^{-\frac{t}{\tau_i}} \tag{1}$$

da sich je nach Komplexität des Abklingverhaltens des untersuchen Fluorophor/Gewebes-Systems eine Überlagerung mehrerer Abklingkurven ergeben kann. In der Regel erfolgt ein Fit mit maximal drei Komponenten [93], es ist jedoch auch ein Fit mit mehr Komponenten möglich [98].
Der Index $_1$ also τ_1 und a_1 wird hierbei mit der kürzesten Lebensdauer, Index $_2$ also τ_2 und a_2 mit der zweitkürzesten Fluoreszenzlebensdauer und fortführend assoziiert. Die zeitabhängige Gesamtintensität $I\,(t)$ eines Pixels setzt sich also aus der Überlagerung von Exponentialfunktion mit den Abklingzeiten τ_i und den Amplituden a_i nach Gleichung (2) [91, 93] zusammen.

$$a = \sum_{i=1}^{n} a_i \tag{2}$$

Hieraus kann mit der Bedingung nach Gleichung (3)

$$\sum_{i=1}^{n} a_{i\%} = 100\% \tag{3}$$

der prozentuale Anteil $a_{i\%}$ einer Substanz einer bestimmten Fluoreszenzlebensdauer τ_i ermittelt und für weitere Berechnungen herangezogen werden. Für die metabolische Bildgebung wird auf diese Weise, über die unterschiedlichen Fluoreszenzlebensdauern von freiem und proteingebundenem NADH und FAD, der jeweilige Anteil $NADH_{a_{1\%}}$ und $NADH_{a_{2\%}}$ sowie $FAD_{a_{1\%}}$ und $FAD_{a_{2\%}}$ und so fort bestimmt [6, 81, 9].
Die hierfür erforderliche Fluoreszenz kann durch Ein- oder Zwei-Photonen-Anregung erzeugt werden. Die erforderliche Ein-Photonen-Anregungswellenlänge für NADH liegt mit ca. $350\,nm - 400\,nm$ [99, 100, 17] im Ultraviolett-Bereich (UV) und ist damit potentiell gewebeschädigend. Ebenso sind aufgrund der höheren Absorption, vor allem durch Hämoglobin [101], und die größere Mie-Streung [23] von Gewebe im UV-Bereich nur geringe optische Eindringtiefen in diesem Wellenlängenbereich zu erreichen. Bei der Zwei-Photonen-Anregung liegt die Anregungswellenlänge beim doppelten der Ein-Photonen-Anregungswellenlänge. Im Rahmen der vorliegenden Arbeit wird zur Zwei-Photonen-Anregung von NADH eine Wellenlänge von $\lambda_{ex} = 780\,nm$ und für FAD von $\lambda_{ex} = 880\,nm$ verwendet und somit das diagnostische Fenster in Gewebe im nahen Infrarotbereich [12, 102] für eine erhöhte optische Eindringtiefe genutzt. Um für die Diagnostik relevante Informationen zu erhalten, ist eine hohe Eindringtiefe und damit die Möglichkeit der Bilderzeugung bis in den Bereich der Basalmembran hinein vorteilhaft. Bei Zwei-Photonen-Anregung kann eine Eindringtiefe von etwa 2 bis 3 mal der mittleren freien Weglänge [103, 104, 105] erreicht werden. Die mit Zwei-Photonen-Anregung erreichbare Eindringtiefe entspricht damit ca. dem dreifachen der mit Konfokalmikroskopie und Ein-Photonen-Anregung erreichbaren Tiefe [104]. In ex vivo Gewebe der menschlichen Zunge sind hier mit Zwei-Photonen-Anregung Tiefen von größer $300\,\mu m$ [105] erreichbar, in vitro kann im Tiermodell im Neocortex eine Tiefe von bis zu $1\,mm$ erreicht werden [106, 107, 108]. Die erreichbare Tiefe ist neben den Streueigenschaften des untersuchten Gewebes auch von Parametern wie der Anregungswellenlänge, Anregungspulsdauer und der verfügbaren Anregungslaserleistung abhängig [108]. Aufgrund der höheren erreichbaren Eindringtiefe in Gewebe und der Vermeidung von UV-Anregung ist die Zwei-Photonen-Anregung für metabolische Bildgebung gegenüber der Ein-Photonen-Anregung zu bevorzugen.
Die Möglichkeit der Zwei-Photonen-Anregung wurde 1931 von Maria Göppert-Mayer theoretisch beschrieben [109], im Jahr 1961 erstmals demonstriert [110] und wird seit Anfang der 1990er Jahre in der Laser-Scan-Mikroskopie eingesetzt [111]. Zur Realisation der Zwei-Photonen-Anregung ist die Anregung des elektronischen Zustandes eines Fluorophors mit zwei Photonen innerhalb eines Zeitfensters von $10^{-16}\,s - 10^{-17}\,s$ [112] notwendig. Um die notwendigen kurzen Pulsdauern von etwa $100\,ps$ zu erreichen wurden anfangs Farbstofflaser, später Titan-Saphir-Laser verwendet. Zunehmend finden, wenn keine Durchstimmbarkeit sondern nur eine Wellenlänge erforderlich ist, Faserlaser Anwendung. Die ersten Zwei-Photonen-Mikroskopaufnahmen von lebenden Zellen entstanden durch Anregung mit einem Farbstofflaser im Jahre 1990 [111]. Die Technologie wurde seither kontinuierlich weiterentwickelt und findet heute, vor allem auf Grund der Möglichkeit lebende Zellen zu untersuchen, vielfältige Anwendungen in den Lebenswissenschaften (Zellkultur, in vivo teilweise in Mäuse/Ratten Gehirn mit Fasersonden [113]).

4.4 Metabolische Bildgebung

Informationen über den Oxidations- und Reduktions-Zustand von Gewebepräparaten können über die Fluoreszenzintensitäten von NADH und FAD [26], welche jedoch schwierig zu messen sind, gewonnen werden. Spektrale Messungen zur Bestimmung der Anteile von gebundenem und freiem NADH und FAD stehen vor der Herausforderung, die geringe spektrale Verschiebung von ca. 10 nm [82] zwischen den Fluoreszenzspektren der beiden Formen nachzuweisen, verfügen aber in der Regel nicht über die hierzu notwendige Sensitivität [11]. Während Messungen der Fluoreszenzintensität von Faktoren wie Konzentration, Gewebedicke, Aufbau, etc. abhängen, sind Messungen der Fluoreszenzlebensdauer von diesen Faktoren weitestgehend unabhängig [4].
Durch die Messung der individuellen Fluoreszenzlebensdauern der freien und proteingebundenen Formen von NADH und FAD ist eine Unterscheidung jedoch möglich [10, 87, 9]. Aus den prozentualen Amplitudenanteilen $a_{i\%}$ der FLIM-Fitfunktionen lässt sich mittels geeigneter mathematischer Verfahren [114, 10, 8, 9] ein metabolischer Index als Kenngröße berechnen, welcher Rückschlüsse auf den Stoffwechselzustand der untersuchten Zellen beziehungsweise des Gewebes erlaubt. Einen weitergehenden Überblick über metabolische Bildgebungsverfahren liefert [115].
Im Rahmen des übergeordneten Projektes OMOXI zur Integration eines Faserlasers in eine existierende Technologie zur Fluoreszenzlebensdauertomographie der Haut [5, 24], wurde durch einen Industriepartner (TOPTICA Photonics AG, Gräfelfing) ein Faserlaser zur simultanen Anregung von NADH und FAD [116] mit den in Tabelle 1 beschriebenen Parametern entwickelt und in den FLIM-Tomographen MPTflex [24] sowie das Multiphotonen-FLIM-Mikroskop der AG Rück an der Universität Ulm integriert.

Wellenlänge $[nm]$	Pulsdauer $[fs]$	Ausgangsleistung $[mW]$
780	< 150	> 300
880	< 100	> 200

Tabelle 1: Spezifizierte Laserparameter für den vom Industriepartner TOPTICA Photonics entwickelten Faserlaser zur simultanen Anregung von NADH und FAD; Repetitionsrate 80 MHz, Strahldurchmesser 1,2 mm

Über den Industriepartner TOPTICA Photonics erfolgte die Entwicklung eines für die FLIM-Bildgebung geeigneten Endoskops mit den in Tabelle 2 genannten Spezifikationen, das an den Tomographen MPTflex adaptiert wurde. Der Vergleich von Aufnahmen mit dem so modifizierten MPTflex mit den von zwei Forschungsmikroskopen erzeugten Aufnahmen wird im dritten Manuskript dieser Arbeit beschrieben [117].

Durchmesser $[mm]$	Länge $[mm]$	Numerische Apertur (NA)	Arbeitsabstand $[\mu m]$
10	250	$> 0{,}5$	$\approx 50 - 100$

Tabelle 2: Spezifizierte Parameter des vom Industriepartner TOPTICA Photonics spezifizierten Endoskops zur Adaption an den MPTflex-Tomographen

Da in der Literatur mehrere Algorithmen für die Berechnung von metabolischen Indices bekannt sind [26, 10, 8], erfolgte in enger Kooperation mit der AG Rück eine Untersuchung

publizierter sowie neu entwickelter Algorithmen zur Berechnung metabolischer Indices. Da für diagnostische Zwecke ein bildgebendes Verfahren von Interesse ist, wurden auf Pixelbasis über das gesamte Bild metabolische Indizes der beschriebenen Algorithmen [9] erstellt. Die pixelgenaue Angabe des metabolischen Index kann insbesondere für die Beurteilung von Tumorgrenzen relevant werden. Ziel dieser und weitergehender Untersuchungen ist die Identifizierung und Validierung von Algorithmen und Darstellungsmöglichkeiten für die metabolische Bildgebung.

Der Arbeit erstes, in Kooperation mit der AG Rück der Universität Ulm entstandenes, Manuskript beschäftigt sich mit der Validierung von zwei publizierten sowie zwei neu entwickelten, FMN einbeziehenden, Berechnungsverfahren für metabolische Indices am Beispiel von Zellkulturen. Hierzu wurden FLIM-Messungen an Zellkulturen von HaCaT-Zellen und SCC4-Zellen sowie an Kokulturen beider Zelltypen durchgeführt. Aus den ermittelten Amplitudenanteilen der freien und gebundenen Fluorophore NADH und FAD wurden in der Literatur bekannte, sowie neu entwickelte metabolische Indices berechnet und miteinander verglichen. Aus den FLIM-Messdaten wurden zusätzlich Falschfarb-2D Bilder der Indices der Zellkulturen erstellt und diese zusätzlich visuell verglichen. Weiterhin wird der Einfluss von FMN sowohl auf die FLIM Messungen als auch auf die Berechnung von metabolischen Indices diskutiert.

4.5 Künstliche Gewebephantome

Um die metabolische Bildgebung in eine klinische Anwendung zu übertragen, ist die Validierung des Verfahrens sowie der entwickelten Gerätetechnik notwendig. Dies kann in der Regel nicht erst unmittelbar am Patienten erfolgen. Humane Gewebepräparate, beziehungsweise tierisches Gewebe vom Schlachthof, sind aufgrund der hohen Variabilität der optischen Eigenschaften (Streukoeffizient, Absorptionseigenschaften, etc.) zwischen Gewebeproben, selbst beim gleichen Gewebetyp derselben Spezies [118, 119], nicht zur Verwendung für eine Validierung geeignet, da reproduzierbare Ergebnisse nicht erwartet werden können. Bei der Entwicklung und Testung, sowie für die Zulassung und den Vergleich medizinischer Diagnosesysteme, sind reproduzierbare Messungen an künstlichen Konstrukten mit kontrollierbaren und reproduzierbar herstellbaren (optischen) Eigenschaften notwendig [13]. Dabei handelt es sich um sogenannte künstliche optische Gewebephantome, welche die für die jeweilige Untersuchung relevanten Eigenschaften, in diesem Fall Absorption, Streuung sowie spektrale und zeitliche Fluoreszenzeigenschaften, reproduzierbar und kontrollierbar darstellen [13]. Es können beispielsweise feste Phantome auf Agar-Basis mit Polystyrene Microspheres [120, 104] (nicht fluoreszierende Polystyrene Microspheres als Streuzentrum; fluoreszierende Polystyrene Microspheres zur Bildgebung), Gold-Nanopartikel [121] oder flüssig-Phantome [122] genutzt werden. Andere Phantomentwicklungen sind für spezielle Fluoreszenzkamerasysteme geeignet [123, 124] oder bilden Gewebe [30, 125] bzw. Hautstrukturen nach [126].
Welche Art von Phantom für den jeweiligen Verwendungszweck geeignet ist, ist vom Experiment abhängig. Artifizielle Fluoreszenzphantome können in Fluorophorlösungen und solche mit örtlich fixierten Fluoreszenzzentren eingeteilt werden. Im vorliegenden Projekt war die Frage zu lösen, ob eine Fluorophorlösung, in der nur spektrale Eigenschaften

nachgestellt werden müssen, ausreichend ist oder ob zusätzlich der Einfluss von Gewebeeigenschaften (Absorption, Streuung) berücksichtigt werden muss. Während der Untersuchungen zu dieser Arbeit zeigte sich, das auch örtlich lokalisierte Fluoreszenz- und Streueigenschaften benötigt werden.
Im Rahmen dieses Promotionsvorhabens wurden zwei künstliche Gewebephantome entwickelt: Mit Phantom 1 können die zeitlichen und spektralen Eigenschaften der Fluoreszenz von freiem und proteingebundenem NADH und FAD hinreichend genau nachbildet werden. Mit Phantom 2, einem 3-Dimensional strukturierten Phantom, kann der Einfluss der Streueigenschaften eines bestimmten Gewebetyps auf die erreichbare Bildgebungstiefe untersucht werden. Hierzu wurden auf einer treppenartigen Glasstruktur in Tiefen zwischen $0\,\mu m$ bis ca. $250\,\mu m$ unter der Oberfläche des Phantoms fluoreszierende Polystyrene Microspheres in ca. der Größe von Mitochondrien fixiert. Der Raum oberhalb einer jeden Stufe wurde mit einem Medium ausgefüllt, welches die optischen Einschaften von Gewebe aufweist. Solche Phantome erlauben einen Vergleich von optischen Messsystemen hinsichtlich ihrer Abbildungsqualität sowie der erreichbaren Abbildungstiefe in streuendem Gewebe.

Die Fluorophore NADH und FAD sind Aufgrund der Abhängigkeit ihrer Fluoreszenzlebensdauer und Intensität von Faktoren wie zum Beispiel Konzentration [18], pH-Wert [16], Oxidationszustand [4] und der geringen Haltbarkeit in Lösung (Stunden bis maximal ein Tag, beziehungsweise ca. zwei Monate bei $-20°C$) als Fluoreszenzlebensdauerreferenz ungenügend geeignet. Ferner bestehen bei diesen Fluorophoren Mess- und Auswertetechnisch weitere, bereits in der Literatur beschriebene Hindernisse zur Verwendung als Referenzsubstanz [127].
Im Rahmen dieser Arbeit zeigte sich weiterhin, dass in der Literatur häufig für die selben Fluorophore unterschiedliche Fluoreszenzlebensdauern beziehungsweise eine unterschiedliche Anzahl an Exponential-Komponenten angegeben werden [14, 15, 16, 17]. Für eine Verwendung als Standard wird jedoch ein monoexponentielles Abklingverhalten empfohlen [4, 33]. In einer Kooperation mit der AG Hellerer (Multiphoton Imaging Labor der Hochschule München für angewandte Wissenschaften) wurden die Einflussfaktoren auf FLIM-Messungen weitergehend untersucht [19].

Das zweite Manuskript der Dissertation beinhaltet die Entwicklung von auf Coumarin 1 und Coumarin 6 basierenden künstlichen Phantomen. Die Phantome zeigen die spektralen und zeitlichen Eigenschaften der Fluoreszenz der freien und proteingebundenen Formen von NADH und FAD. Ferner eignen sie sich zur Validierung von Messsystemen für Fluoreszenzlebensdauer und/oder zur metabolischen Bildgebung. Die entwickelten Phantome basieren auf mit 4-Hydroxy-TEMPO gequenchten Coumarin 1 und Coumarin 6 Lösungen. Sie sind prinzipiell auf alle Fluoreszenzlebensdauern zwischen ca. 200 *ps* und den ungequenchten Lebensdauern der Fluorophore Coumarin 1 und 6 von ca. 3000 *ps* und ca. 2500 *ps* einstellbar.

Die beschriebenen Fluoreszenzlebensdauerphantome bestehen aus homogenen, strukturlosen Lösungen und eignen sich damit nicht zur Bestimmung der Lage der Fokalebene eines Messsystems. Die Ermittlung der maximalen, mit einer physiologisch verträglichen Anregungsleistung, erreichbaren Bildgebungstiefe innerhalb von realem, streuendem, Gewebe

oder einem artifiziellen Gewebephantom ist somit mit ihnen nicht möglich. Für die diagnostische/klinische Anwendung eines mikroskopischen- oder mikro-endoskopischen Systems ist die Information, bis in welche Gewebeschichten (Tiefe) eine Tumorausbreitung stattfand jedoch von Bedeutung [39, 40]. Für die Entwicklung eines diagnostischen Systems werden Referenzen benötigt, die den Abgleich mit zuvor gestellten Anforderungen ermöglichen. Diese sollen ebenfalls für den Vergleich mit weiteren Systemen geeignet sein. In der Literatur beschriebene Referenzsysteme [124, 123] zur Charakterisierung von bildgebenden Systemen wurden für makroskopische Weitfeldtechniken entwickelt und sind für mikroskopische Anwendungen ungeeignet. Dies gilt ebenso für das, vielfach zur Bestimmung der optischen Auflösung verwendete, 1951 USAF resolution test chart [128, 129], da mit diesem keine Information über die Position der Fokalebene in Gewebe abgeleitet werden kann.
Ein artifizielles Gewebephantom zur Charakterisierung eines endoskopischen Systems zur metabolischen Bildgebung sollte somit folgende Eigenschaften aufweisen:

- Lokalisierte, fluoreszierende, NADH und FAD simulierende, Strukturen in der Größenordnung von Zellen beziehungsweise Mitochondrien
- Ausdehnung in z-Richtung entsprechend der zu erwartenden, maximalen Bildgebungstiefe von Zwei-Photonen-Mikroskopie von ca. 300 μm [105] in streuendem Gewebe

Zur Charakterisierung eines endoskopischen Systems ist daher eine Neuentwicklung beziehungsweise ein anderer Ansatz notwendig.
Im Gegensatz zu Forschungsmikroskopen verfügen in der medizinischen Diagnostik eingesetzte Endoskope weder über einen Mikroskoptisch zur x, y-Positionierung einer Probe, noch über einen z-Trieb zum Verfahren des Objektives und damit zur Verschiebung der Fokalebene innerhalb der zu untersuchenden Probe. Um die Position der Fokalebene, sowohl bei einem Forschungsmikroskop als auch bei einem endoskopischen System, mit dem selben Phantom bestimmen zu können, wurde ein mikrostrukturiertes künstliches Gewebephantom mit modifizierbaren optischen Eigenschaften und fluoreszierenden Strukturen entwickelt. Hierfür wurde eine treppenförmige Struktur mittels Femtosekunden-Laser in einen Objektträger eingearbeitet (Einzel-Stufentiefe ca. 5 μm, Stufenlänge ca. 200 μm, maximale Tiefe ca. 250 μm). Die jeweiligen Treppenstufenflächen wurden mit fluoreszierenden Polystyrene Microspheres in der Größe von Mitochondrien (ca. 1 μm Durchmesser) beschichtet. Die spektralen Eigenschaften der Polystyrene Microspheres ähneln denjenigen von NADH und FAD hinsichtlich ihres Anregungs- und Fluoreszenz-Spektrums. Das herausgearbeitete Volumen oberhalb der Treppenstufen kann zum Zwecke der Gewebesimulation mit einer Mischung bestehend aus einem Hydrogel und einer Suspension nicht fluoreszierender Polystyrene Microspheres als Streuzentren aufgefüllt werden. Für die experimentelle Nachahmung der Streueigenschaften von Schleimhaut der humanen Kieferhöhle [20] bei 780 nm und 880 nm wurde mit einem Optimierungsprogramm, basierend auf einem Berechnungsprogramm [21, 22] zur Mie-Streuung [23], das notwendige Volumenverhältnis von Hydrogel und Polystyrene Microspheres ermittelt. Die Suspensionen wurden mit einem Aufbau zur Messung von optischen Gewebeeigenschaften validiert [119]. Die Strukturierung des Phantoms erlaubt Aufschluss über die Tiefenposition der Fokalebene unterhalb der Phantomoberfläche. Die optischen Eigenschaften der Suspension ermöglichen einerseits die Simulation des Zielgewebes, andererseits kann der Einfluss

der Suspension auf die Fluoreszenzsignale untersucht werden.

Das dritte Manuskript beinhaltet die Entwicklung und Charakterisierung eines für mikroskopische und endoskopische Systeme geeigneten künstlichen Gewebephantoms zur Ermittlung der Fokusposition bis zu einer Tiefe von ca. 250 μm in 5 μm Schritten mit darüberliegenden, einstellbaren, optischen Eigenschaften. Hierfür wurde eine treppenförmige Struktur entworfen und mittels Laser-Mikrostrukturierung in Glaskörpern (Objektträger, n=10) hergestellt. Die so erhaltenen treppenförmigen Mikrostrukturen in den Objektträgern wurden hinsichtlich Stufenhöhe, Stufenlänge, Anzahl unterscheidbarer Stufen, Oberflächenbeschaffenheit und Gesamttiefe charakterisiert. Fluoreszierende Strukturen in der Größe von 1 μm wurden mittels Beschichtung der Treppenstufen mit fluoreszierenden Polystyrene Microspheres hergestellt. Die Streueigenschaften von Gewebe wurden durch Auffüllen des Volumens oberhalb der treppenartigen Struktur mit einer Mischung aus einem Hydrogel und einer Suspension aus nicht fluoreszierenden Polystyrene Microspheres realisiert. Der Gesamtaufbau des Phantoms wurde mit zwei Mikroskopsystemen charakterisiert. Seine Alterungsbeständigkeit wurde untersucht, sowie die Möglichkeit unterschiedliche Systeme zu vergleichen an einem Beispiel demonstriert. Aufgrund der regelmäßigen, durch die Charakterisierung bekannten, Dimensionen der Treppenstruktur konnte darüber hinaus die Möglichkeit gezeigt werden, mit diesem Phantom Unterschiede in der Bildqualität (Verzerrungen) zwischen einem Forschungsmikroskop und dem im Rahmen des Projektes entwickelten Endoskops zu erkennen und mögliche Ursachen zu identifizieren. Die regelmäßige Struktur ermöglicht die Bestimmung der Lage der Fokalebene eines Endoskopiesystems ohne z-Stage relativ zur Phantomoberfläche und damit die Ermittlung der (maximalen) Bildgebungstiefe.

5 Originalmanuskripte

- **C. Freymüller**, S. Ströbl, M. Aumiller, M. Eisel, R. Sroka und A. Rühm, "Development of a microstructured tissue phantom with adaptable optical properties for use with microscopes and fluorescence lifetime imaging systems", *Lasers in Surgery and Medicine*, S. 1–17, 2022, Publisher: John Wiley & Sons, Ltd. DOI: 10.1002/lsm.23556, JIF_{2021}: 4.025.
- S. Kalinina, **C. Freymüller**, N. Naskar, B. von Einem, K. Reess, R. Sroka und A. Rück, "Bioenergetic alterations of metabolic redox coenzymes as NADH, FAD and FMN by means of fluorescence lifetime imaging techniques", *International Journal of Molecular Sciences*, Jg. 22, Nr. 11, S. 5952, 31. Mai 2021. DOI: 10.3390/ijms22115952, JIF_{2021}: 6.208.
- **C. Freymüller**, S. Kalinina, A. Rück, R. Sroka und A. Rühm, "Quenched coumarin derivatives as fluorescence lifetime phantoms for NADH and FAD", *Journal of Biophotonics*, 8. Apr. 2021. DOI: 10.1002/jbio.202100024, JIF_{2021}: 3.390.

5.1 Bioenergetic Alterations of Metabolic Redox Coenzymes as NADH, FAD and FMN by Means of Fluorescence Lifetime Imaging Techniques

S. Kalinina, **C. Freymüller**, N. Naskar, B. von Einem, K. Reess, R. Sroka und A. Rück, "Bioenergetic alterations of metabolic redox coenzymes as NADH, FAD and FMN by means of fluorescence lifetime imaging techniques", *International Journal of Molecular Sciences*, Jg. 22, Nr. 11, S. 5952, 31. Mai 2021. DOI: 10.3390/ijms22115952, JIF_{2021}: 6.208.

Kurzfassung: Fluoreszenz-Lebensdauer-Bildgebung (Metabolisches FLIM) wird in den Lebenswissenschaften und in der medizinischen Forschung häufig für die Darstellung des bioenergetischen Zustands, in welchem sich Zellen und Gewebe befinden, verwendet. Hierbei ist die Fluoreszenzlebensdauer der Koenzyme NADH und FAD als Indikator für den Zellstoffwechsel allgemein akzeptiert. Für die Berechnungen werden die prozentualen Amplitudenanteile $a_{i\%}$ aus dem mathematischen Fitprozess an die Abklingkurven von NADH und FAD verwendet.
Der für die Berechnung und Darstellung des Redoxverhältnisses verwendete FLIRR-Index (FLIRR1; proteingebundenes NAD(P)H im Verhältnis zu proteingebundenem FAD) wurde um weitere FLIM-Daten von NAD(P)H und den Flavinen FAD und FMN um die Indices FLIRR2 und FLIRR3 erweitert. Es wird ein zwei Komponenten Exponentialfit für NAD(P)H und ein drei Komponenten Exponentialfit für die Flavine verwendet. Anhand von SCC4 (human oral squamous carcinoma cell) und HaCaT (immortalized keratinocyte cell) Zellkulturen wurden die Indizes FLIRR1 , FLIRR2 (proteingebundenes NAD(P)H im Verhältnis zu freiem FAD) und FLIRR3 (proteingebundenes NAD(P)H im Verhältnis zu proteingebundenem FMN) berechnet und mit dem NAD(P)H metabolischen Index (Verhältnis von proteingebundenem NAD(P)H zu freiem NAD(P)H) verglichen. Weiterhin wurde ein Berechnungsverfahren entwickelt, um aus FLIM-Aufnahmen von SCC4-Zellen, HaCaT-Zellen und Kokulturen der beiden Zelltypen 2D-Falschfarbbilder der FLIRR1 bis FLIRR3 Indizes und des NAD(P)H metabolischen Index zu erzeugen und so Unterschiede im Zellmetabolismus zu visualisieren.

Der Anteil von Christian Freymüller war die Überprüfung der Rohdaten, Unterstützung bei der Auswertung und Dateninterpretation, Export der FLIM-Berechnungen und die Diskussion der untersuchten Indizes. Darüber hinaus die alleinige Entwicklung und Umsetzung eines Algorithmus (Aufbau siehe Supplementary Material Seite 46) in Matlab (The MathWorks Inc., Natick, USA) zur 2D-Berechnung der FLIRR1 bis FLIRR3 Indizes und des NAD(P)H metabolischen Index der FLIM-Messungen an den verwendeten Zellkulturen und deren konsistenter Falschfarb-2D-Darstellung, sowie Erstellung der entsprechenden Teile des Manuskripts.

International Journal of
Molecular Sciences

MDPI

Article

Bioenergetic Alterations of Metabolic Redox Coenzymes as NADH, FAD and FMN by Means of Fluorescence Lifetime Imaging Techniques

Sviatlana Kalinina [1,*], Christian Freymueller [2,3], Nilanjon Naskar [1], Bjoern von Einem [4], Kirsten Reess [1], Ronald Sroka [2,3] and Angelika Rueck [1,*]

[1] Core Facility Confocal and Multiphoton Microscopy, Ulm University, Albert-Einstein-Allee 11, 89081 Ulm, Germany; nilanjon.naskar@uni-ulm.de (N.N.); kirsten.reess@uni-ulm.de (K.R.)
[2] Laser-Forschungslabor, LIFE Center, University Hospital, LMU Munich, Fraunhoferstrasse 20, 82152 Planegg, Germany; christian.freymueller@med.uni-muenchen.de (C.F.); ronald.sroka@med.uni-muenchen.de (R.S.)
[3] Department of Urology, University Hospital, LMU Munich, Marchioninistraße 15, 81377 Munich, Germany
[4] Zentrum Biomedizinische Forschung (ZBMF), Department of Neurology, Ulm University, Helmholtzstrasse, 8/1, 89081 Ulm, Germany; bjoern.von-einem@uni-ulm.de
* Correspondence: sviatlana.kalinina@uni-ulm.de (S.K.); angelika.rueck@uni-ulm.de (A.R.)

Abstract: Metabolic FLIM (fluorescence lifetime imaging) is used to image bioenergetic status in cells and tissue. Whereas an attribution of the fluorescence lifetime of coenzymes as an indicator for cell metabolism is mainly accepted, it is debated whether this is valid for the redox state of cells. In this regard, an innovative algorithm using the lifetime characteristics of nicotinamide adenine dinucleotide (phosphate) (NAD(P)H) and flavin adenine dinucleotide (FAD) to calculate the fluorescence lifetime induced redox ratio (FLIRR) has been reported so far. We extended the FLIRR approach and present new results, which includes FLIM data of the various enzymes, such as NAD(P)H, FAD, as well as flavin mononucleotide (FMN). Our algorithm uses a two-exponential fitting procedure for the NAD(P)H autofluorescence and a three-exponential fit of the flavin signal. By extending the FLIRR approach, we introduced FLIRR1 as protein-bound NAD(P)H related to protein-bound FAD, FLIRR2 as protein-bound NAD(P)H related to free (unbound) FAD and FLIRR3 as protein-bound NAD(P)H related to protein-bound FMN. We compared the significance of extended FLIRR to the metabolic index, defined as the ratio of protein-bound NAD(P)H to free NAD(P)H. The statistically significant difference for tumor and normal cells was found to be highest for FLIRR1.

Keywords: FLIM; NAD(P)H; FAD; FMN; NAD(P)H metabolic index; FLIRR index; extended FLIRR; cell metabolism; OXPHOS; glycolysis

Citation: Kalinina, S.; Freymueller, C.; Naskar, N.; von Einem, B.; Reess, K.; Sroka, R.; Rueck, A. Bioenergetic Alterations of Metabolic Redox Coenzymes as NADH, FAD and FMN by Means of Fluorescence Lifetime Imaging Techniques. *Int. J. Mol. Sci.* **2021**, *22*, 5952. https://doi.org/10.3390/ijms22115952

Academic Editor: Enrique Meléndez-Hevia

Received: 18 May 2021
Accepted: 28 May 2021
Published: 31 May 2021

1. Introduction

A common property during tumor development and other diseases is altered energy metabolism, which can lead to a switch between oxidative phosphorylation (OXPHOS) and a glycolytic profile. Fluorescence lifetime imaging (FLIM) of metabolic coenzymes i.e., NAD(P)H (nicotinamide adenine dinucleotide (phosphate)) and FAD (flavin adenine dinucleotide), is now widely accepted to be one of the most important methods for metabolic imaging. It could be demonstrated that time-correlated single photon counting (TCSPC) techniques can separate different decaying compounds with high spatial and temporal resolution [1]. Various algorithms are developed to get reproducible and convincing results (for review see [2]). The correct interpretation of the cellular redox state and the correlation with the fluorescence lifetime τ of the coenzymes is, however, still debated. In 1979, Britton Chance replaced the biochemically defined redox ratio of NAD(P)H related to NAD^+ to a measure, defined as NAD(P)H related to FAD^+, the so-called optical redox ratio which uses only fluorescent parameters [3]. This intensity-based optical redox ratio determines

the redox ratio of cells and distinguishes oxidized from reduced states. A correlation with the fluorescence lifetime is valid only for special conditions if the NADH/NAD^+ pool is stable [3]. However, NAD^+ can be metabolized in different reactions, leading to a change in the redox ratio but not necessarily in the fluorescence lifetime, which is only an indicator of cell metabolism [4–6]. In contrast, a change in the NADH/NAD^+ ratio which affects the binding dynamics of NADH-related enzymes can change the lifetime components of NADH [7,8]. Therefore, a careful interpretation of the redox state is needed when comparing the fluorescence lifetime of different cell systems. New algorithms are needed to circumvent these problems, and to image cell metabolism and redox state from fluorescence lifetimes in complex cellular systems. In this regard, results published so far will be summarized and new approaches will be discussed. In this work, the significance of a metabolic index based on NAD(P)H FLIM will be explained and the results will be compared to the fluorescence lifetime induced redox ratio (FLIRR) where FLIM parameters of NAD(P)H and FAD are related [9]. In contrast to invasive biochemical methods, including chromatography analysis, the optical techniques of measuring the metabolic index based on NAD(P)H FLIM, as well as FLIRR is a non-invasive straightforward and direct technique, allowing on-line visualization of the redox state.

Coenzymes that are involved in energy metabolism belong to the NAD(P)H and flavin family, as FAD and FMN (flavin mononucleotide). Their spectral and lifetime characteristics that are found in the literature [10–15] are the results of their chemical structures summarized in Figure 1.

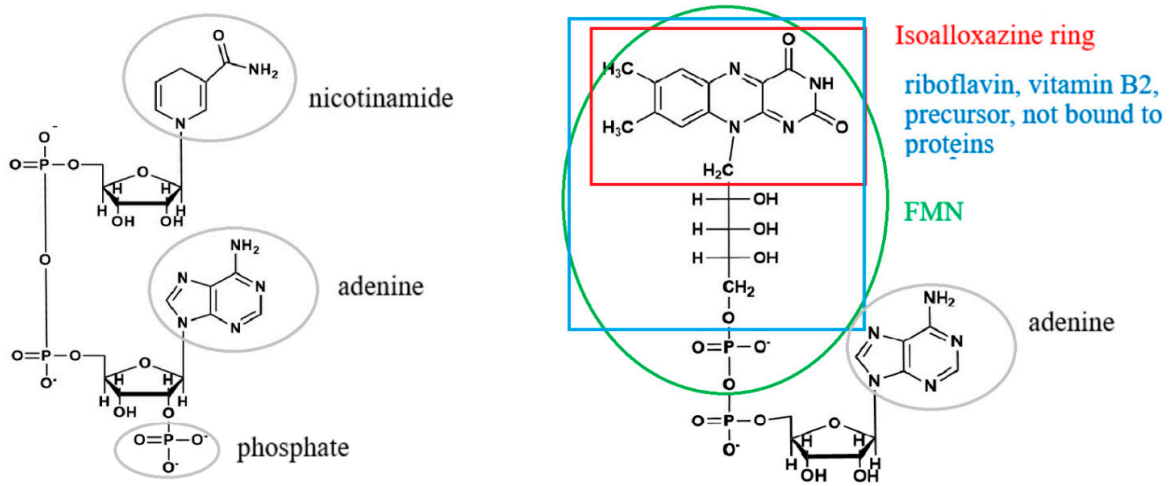

NAD(P)H: reduced nicotinamide adenine dinucleotide (phosphate), fluorescent under excitation at 360 nm

τ_{free} is about 0.4 ns (short)
τ_{bound} is about 2.5 ns (long)

FAD/FMN: flavin-adenine dinucleotide/-mononucleotide, fluorescent under excitation at 450 nm

FAD^+: τ_{free} is about 2.3 ns (long)
τ_{bound} is about 0.3 ns (short)

FMN^+ τ_{free} is about 1.5 ns (short)
τ_{bound} is about 5 ns (short)

Figure 1. Intracellular coenzymes that play key roles in energy metabolism and metabolic FLIM and their spectral and lifetime characteristics obtained from published data [10,12–15]. The figure was prepared using the software "ChemDraw (version 20.1.0.110)".

Binding of NADH to proteins of the respiratory chain during OXPHOS increases the proportion of the protein-bound enzyme, which possesses a longer fluorescence lifetime, whereas a decreased portion of the protein-bound NADH and increased free NADH during anaerobic glycolysis induces a shortening of the fluorescence lifetime (see Figure 1 and references [1,8,12]). Due to both free and bound NADH being found simultaneously, a biexponential fit of the fluorescence decay is normally performed. By inspecting the ratio of the exponential coefficients (amplitudes) of the short and long lifetime components (a_1/a_2) a change from OXPHOS to glycolytic cellular states can be observed during tumor development [16,17]. A 10% increase of the ratio was significant to observe the metabolic switch [17]. Similarly, cisplatin induced a decrease of the ratio by approx. 10% in HeLa tumor, indicating a switch from glycolysis to OXPHOS, correlated with apoptosis [18]. The ratio a_1/a_2, the so-called metabolic index based on NAD(P)H FLIM, seems to be a useful metric to diagnose cell metabolism. However, this parameter is also not fully correlated to the redox state of the cells. Following the idea of Britton Chance and his definition of the optical redox ratio, FAD should be included in the calculations. As a consequence, quantitative optical metabolic imaging was introduced by Walsh et al., which depends on both the intensity based redox ratio and the fluorescence lifetimes of NAD(P)H and FAD [19]. Moreover, Periasamy and coworkers defined the FLIRR index where the relative amount of bound NAD(P)H is correlated with the relative amount of bound FAD [9]. In that case, the exponential coefficients of both NAD(P)H and FAD were calculated from a biexponential fitting procedure. Whereas bound NAD(P)H is correlated to the amplitude of the longer lifetime component a_2, a reverse trend is followed for FAD. The fluorescence lifetime of the protein-bound FAD is shorter as compared to the free FAD due to the efficient fluorescence quenching of the isoalloxazine chromophore by adenine, induced by the folding of FAD [20,21]. Therefore, the FLIRR index is defined as NAD(P)Ha_2/FADa_1, where FADa_1 is the amplitude of the shorter lifetime component of FAD.

The bound NAD(P)H increases during OXPHOS; however, the situation for FAD is very complicated. There are reports suggesting that FAD bound to proteins is not changed or diminished during OXPHOS, which in addition to the increased protein-bound component of NAD(P)H might contribute to a higher FLIRR value [9]. In correlation, inhibiting complex II of the respiratory chain during Parkinson's disease induced an increased concentration of FAD bound to proteins [22]. However, the reverse was also found. In a work by Skala et al., [23] more glycolysis was found in high grade compared to low grade and normal tumor, which was correlated with a decrease of bound NAD(P)H. Simultaneously, the relative amount of bound FAD also decreased, which could induce a higher FLIRR index, in contrast to the expected decrease during glycolysis. However, results can differ significantly and be compared only if the same experimental conditions are maintained (excitation wavelength, emission filters, etc.). Moreover, FAD contributes to various dehydrogenase systems [24]. Even for free FAD in aqueous buffer solution, a heterogeneous fluorescence intensity decay with two major lifetime components was reported where a dominant 7 ps component that is characteristic of ultrafast fluorescence quenching and a 2.7 ns component interpreted as moderate fluorescence quenching was found [14,25,26]. Moreover, the fluorescence decay has been attributed to two molecular conformations as stacked and opened forms [27]. Also, FAD fluorescence lifetime was found to be pH dependent [26,28], which increases the complexity of interpretation inside cells.

The consideration of FAD FLIM is complicated enough; however, one important component was neglected so far—namely, contributions from FMN during FAD detection. As demonstrated in Figure 1, a subgroup in the FAD molecular structure is FMN, the mononucleotide. Whereas FAD with respect to FLIRR mainly has its function in complex II of the respiratory chain, FMN is involved in complex I. Therefore, FMN that shows opposite fluorescence lifetime characteristics with an exceptionally long lifetime for bound FMN compared to FAD must be considered when investigating metabolic FLIM. Due to this, difficulty can occur in the interpretation of FLIRR. One has to be aware that although concentration of FMN is normally below FAD, the ratio depends on the cell type (see

reference [29]) and the fluorescence quantum yield of FMN is approximately a factor of 10 times higher as compared to FAD [30]. Therefore, FMN was considered during advanced metabolic FLIM within this work. For this reason, we extended the FLIRR index approach and distinguished FLIRR1, FLIRR2 and FLIRR3, after a three-exponential fitting of the flavin signal. The definition of the ratios are as follows:

$$\text{FLIRR1} = \frac{\text{NAD(P)H}_{a_2\%}}{\text{FAD}^{+}{}_{a_1\%}}$$

$$\text{FLIRR2} = \frac{\text{NAD(P)H}_{a_2\%}}{\text{FAD}^{+}{}_{a_2\%}}$$

$$\text{FLIRR3} = \frac{\text{NAD(P)H}_{a_2\%}}{\text{FAD}^{+}{}_{a_3\%}}$$

FLIRR1 relates bound NAD(P)H to bound FAD (interpreted as shortest lifetime component), FLIRR2 bound NAD(P)H to free FAD (interpreted as mean lifetime component) and FLIRR3 bound NAD(P)H to bound FMN (interpreted as longest lifetime component). In addition, we compared the FLIRR results with the metabolic index:

$$\frac{\text{NAD(P)H}_{a_1\%}}{\text{NAD(P)H}_{a_2\%}}$$

and determined the significance during metabolic imaging of keratinocytes and squamous carcinoma cells.

2. Results and Discussion

The emission of different intracellular flavin molecules were detected within the spectral range between 542–582 nm (see Figure 2, "red" channel) after two-photon excitation at 880 nm. The overlapped emission spectra of FMN and FAD including their protein-bound und free states does not allow for spectrally separating the coenzyme signal. The measured autofluorescence decay furthermore demonstrated complex multiple exponential kinetics. In fact, we differentiated at least three fluorescent components with different lifetimes for HaCaT, as well as SCC4 cells using a three-exponential incomplete model (see Table 1):

$$\text{I(t)} = \sum_i a_i \exp(-t/\tau_i)$$

$$\text{(I)} = \sum_i a_i \exp(-t/\tau_i),$$

where τ_i and a_i denote the fluorescence lifetime of component i and its exponential coefficient, respectively. χ^2 values were maintained at below 1.1. The three components within the observed spectral range were assigned to protein-bound FAD, free FAD, and FMN. The shortest lifetime and fast decaying component τ_1 with the highest exponential coefficient a_1 were correlated to the FAD cofactor that is bound to the mitochondrial enzymes. It is likely that a different protein environment of FAD within the cancerous SCC4 and normal HaCaT cells contribute to the significant difference of the τ_1 values (p-value = 9.75×10^{-5}), presented in Table 1.

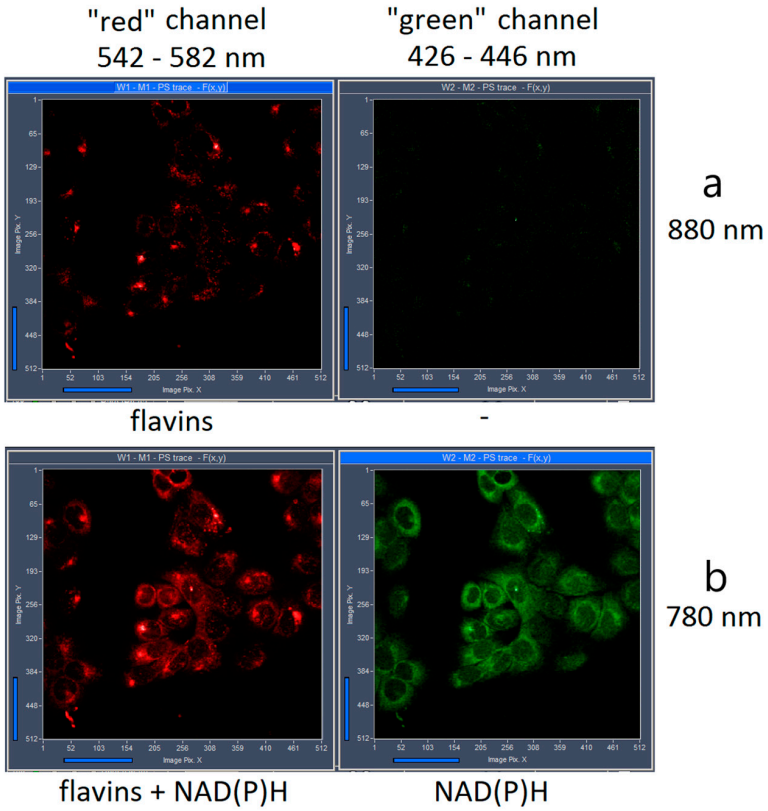

Figure 2. Intensity preview images obtained during lifetime measurements after two-photon excitation at 880 nm (**a**) and 780 nm (**b**) of HaCaT cells. Fluorescence was detected in the spectral range 426–446 nm (green channel) and 542–582 nm (red channel).

Table 1. Fluorescence lifetime values (τ_i) and their corresponding exponential coefficients (a_i) of flavins in HaCaT and SCC4 monocultures. The values were calculated by a three-exponential fit decay analysis.

	τ_{mean} (ps)	τ_1 (ps)	τ_2 (ns)	τ_3 (ns)
HaCaT	791 ± 44	297 ± 33	1.53 ± 0.09	5.40 ± 0.54
SCC4	686 ± 52	246 ± 32	1.40 ± 0.10	4.87 ± 0.46
	a_1 (%)	**a_2 (%)**	**a_3 (%)**	
HaCaT	71.62 ± 0.78	23.18 ± 1.69	10.34 ± 0.39	
SCC4	72.30 ± 0.88	21.94 ± 0.85	9.98 ± 0.79	

The statistical significance of the respective components between HaCaT and SCC4 cells was evaluated using one-way ANOVA test. The *p*-values were 9.02×10^{-7} for τ_{mean}, 9.75×10^{-5} for τ_1, 6.05×10^{-4} for τ_2 and 6.11×10^{-3} for τ_3 whereas for a_1, a_2 and a_3 the p-value was 0.026, 0.014 and 0.112 respectively.

To measure the lifetime of free FAD, we investigated the fluorescence decay of 1 mM buffer solution of FAD at 37 °C after two-photon excitation at 880 nm within the emission range 542–582 nm. The fluorescence intensity decay curve was fitted using a mono-exponential incomplete model, leading to a fluorescence lifetime of 1.90 ± 0.6 ns with χ^2 = 1.3 that closely resembles the value of 1.7 ns reported in the literature [14]. The cited work, along with our results, supports the assumption that the lifetime component τ_2, which we calculated within our cells (see Table 1), can be assigned to intracellular free FAD. In detail, the mean fluorescence lifetime τ_2 in the cells was 1.53 ± 0.09 ns for HaCaT and 1.40 ± 0.10 ns for SCC4 cells with the corresponding coefficients a_2 = 23.18 ± 1.69% and 21.94 ± 0.85% for an incomplete three-exponential free fitting procedure (see Table 1).

Moreover, FMN could also contribute to τ_2. Berg and coworkers [14] reported that the fluorescence lifetime of FMN consists of two components with 1.5 (1.3–1.7) ns and 4.7 (4.7–4.8) ns with the relative amplitudes 12% and 88%. The component at 1.5 ns was attributed to free FMN, whereas the component with the long lifetime around 4.7 ns correlates with protein bound FMN. The third component of our incomplete three exponential fit showed a mean lifetime of 5.40 ± 0.54 ns for HaCaT and 4.87 ± 0.46 ns for SCC4 cells (see Table 1). As mentioned, the long lifetime was also observed by others for intracellular FMN [14,31,32]. However, as described by Esposito et al. for FAD, a three exponential fit can also be obtained in solution that is pH dependent, which can be explained as a mixture of stacked-unstacked species [27]. The situation is therefore quite complex, and interpretations have to be made with care.

In Table 1, a significant difference of the mean flavin fluorescence lifetime for the two cell types is presented ($p = 9.02 \times 10^{-7}$). Also, the first component τ_1, as well as the second component τ_2 of the fitting model that we ascribed to protein-bound and free FAD was significantly different (p-value < 0.001). However, the amplitudes (a_i) that correspond to the contributions of the different decaying components showed less significant difference between the two cell types. It is known that fluorescence lifetime fixation during fitting of the fluorescence decay results in valid calculations [1,33], so we made an attempt to apply an incomplete three-exponential decay model using the fixed lifetime values τ_1 = 250 ps, τ_2 = 1400 ps and τ_3 = 5000 ps. These values were based on the calculations of Table 1, as well as the aforementioned published data. The results of the fitting model with fixed lifetimes are shown in Table 2. Now a_1, a_2 and a_3 were statistically significantly different for HaCaT and SCC4 cells (p-value = 5.45×10^{-5}, 5.56×10^{-5} and 4.12×10^{-5}, respectively). This result exhibits the individual contributions of the three decaying components of flavins inside different cells.

Table 2. Mean fluorescence lifetime (τ_{mean}) and the associated exponential coefficients (a_i) of intrinsic flavin autofluorescence in HaCaT and SCC4 monocultures, derived by an incomplete three-exponential fit decay analysis with fixed lifetime values: τ_1 = 250 ps, τ_2 = 1.4 ns and τ_3 = 5 ns.

	τ_{mean} (ps)	a_1 (%)	a_2 (%)	a_3 (%)
HaCaT	766 ± 47	68.7 ± 2.9	27.0 ± 2.6	4.98 ± 0.40
SCC4	706 ± 26	72.6 ± 1.6	23.5 ± 1.5	4.35 ± 0.34

The statistical significance of the respective components between HaCaT and SCC4 cell lines was evaluated using a one-way ANOVA test. The p-value was 1.05×10^{-4} for τ_{mean} and 5.45×10^{-5}, 5.56×10^{-5}, and 4.12×10^{-5} for a_1, a_2 and a_3, respectively.

In addition to FAD, we investigated FLIM of NAD(P)H in order to calculate the metabolic state of the cells. The "green" spectral channel (426–446 nm) was used to detect the fluorescence decay of protein-bound and free NAD(P)H. Two-photon laser excitation was performed at 780 nm for NAD(P)H. Also, the flavins are excited at the same wavelength, but emission of flavins was detected solely within the "red" (542–582 nm) spectral channel of our FLIM system, without any contribution in the "green" channel (see Figure 2). The mean lifetime of NAD(P)H in HaCaT and SCC4 cells was calculated using a two-exponential incomplete fitting with the fixed components τ_1 = 400 ps and τ_2 = 2.5 ns corresponding to free und protein-bound NAD(P)H, respectively [33,34]. As demonstrated in Table 3, τ_{mean} was significantly different for the two cells. In addition, the NAD(P)H metabolic index a_1/a_2 was significantly different ($p = 6.07 \times 10^{-9}$) and higher in case of the tumor cells. This correlates with increased glycolytic metabolism, described recently in the literature [16–18].

Table 3. Mean fluorescence lifetime (τ_{mean}) and associated exponential coefficients (a_i) of NAD(P)H in HaCaT and SCC4 cells. The values were calculated by a two-exponential fit decay analysis performed with the fixed lifetimes τ_1 = 400 ps and τ_2 = 2.5 ns.

	τ_{mean} (ps)	a_1 (%)	a_2 (%)	a_1/a_2
HaCaT	1160 ± 34	63.8 ± 1.6	36.2 ± 1.6	1.77 ± 0.12
SCC4	1073 ± 28	68.0 ± 1.3	32.0 ± 1.3	2.12 ± 0.13

The statistical significance of the respective components between HaCaT and SCC4 cell lines was evaluated using a one-way ANOVA test, that showed a *p*-value of 7.93×10^{-9} for τ_{mean}, 6.07×10^{-9} for a_1/a_2, 8.14×10^{-9} for a_1 and 7.58×10^{-9} for a_2.

The FLIRR index NAD(P)Ha_2/FADa_1 [9], which relates bound NAD(P)H to bound FAD was calculated for HaCaT as well as SCC4 cells. In addition to the redox ratio index defined by Periasamy and coworkers, we introduced FLIRR1, FLIRR2 and FLIRR3, as FLIRR1 = NAD(P)Ha_2/FADa_1, FLIRR2 = NAD(P)Ha_2/FADa_2 and FLIRR3 = NAD(P)Ha_2/FADa_3 (see Section 3.2). Obviously FLIRR1 corresponds to the former FLIRR index. The values are presented in Table 4 for a three exponential fitting procedure of the flavin decay with free lifetimes and a two-exponential fit of NAD(P)H with fixed lifetimes. In addition, the flavin decay was also analyzed using the fixed lifetime values: τ_1 = 250 ps, τ_2 = 1.4 ns and τ_3 = 5 ns. The results for the respective FLIRR indices are presented in Table 5. FLIRR1 was significantly different for both fitting procedures (free and fixed flavin lifetimes), whereas FLIRR2 and FLIRR3 revealed significance only for the free fit. In addition, the FLIRR1 index derived with free fitting of the flavin lifetimes ($p = 3.89 \times 10^{-9}$) was statistically more significant than the NAD(P)H metabolic index ($p = 6.07 \times 10^{-9}$), where only NAD(P)H is considered. This underlines the importance of investigating both NAD(P)H and FAD for the evaluation of metabolic differences between tumor and normal cells.

Table 4. FLIRR indices for HaCaT and SCC4 cells. FLIRR1 is the ratio between a_2(NAD(P)H) and a_1(flavins), FLIRR2 is the ratio of a_2(NAD(P)H) and a_2(flavins) and FLIRR3 is the ratio of a_2(NAD(P)H) and a_3(flavins). For the calculations, a three-exponential free lifetime fit decay analysis was performed for flavins and a two-exponential fixed lifetime fit decay for NAD(P)H with τ_1 = 400 ps and τ_2 = 2.5 ns.

	FLIRR1 (a_2/a_1)	FLIRR2 (a_2/a_2)	FLIRR3 (a_2/a_3)
HaCaT	0.51 ± 0.02	1.57 ± 0.14	3.5 ± 0.2
SCC4	0.44 ± 0.02	1.46 ± 0.08	3.2 ± 0.3

The statistical significance of the respective exponential components between HaCaT and SCC4 cell lines was evaluated using a one-way ANOVA test that showed a *p*-value of 3.89×10^{-9} for FLIRR1, 0.015 for FLIRR2 and 0.008 for FLIRR3.

Table 5. FLIRR indices of HaCaT and SCC4 cells derived by a three-exponential fit of the flavins with fixed lifetime values, τ_1 = 250 ps, τ_2 = 1.4 ns and τ_3 = 5 ns. The NAD(P)H decay was fitted biexponentially using the fixed lifetimes τ_1 = 400 ps and τ_2 = 2.5 ns.

	FLIRR1 (a_2/a_1)	FLIRR2 (a_2/a_2)	FLIRR3 (a_2/a_3)
HaCaT	0.53 ± 0.04	1.35 ± 0.13	7.3 ± 0.7
SCC4	0.44 ± 0.02	1.37 ± 0.10	7.0 ± 0.7

The statistical significance of the respective components between HaCaT and SCC4 cell lines was evaluated using a one-way ANOVA test that showed a p-value of 4.70×10^{-9} for FLIRR1, 0.685 for FLIRR2 and 0.737 for FLIRR3.

Figure 3 demonstrates the intracellular distribution of the metabolic NAD(P)H index and the different FLIRR indices following the fitting procedures described in Tables 3 and 4. Thus, for NAD(P)H, a two-exponential fitting procedure with fixed lifetimes and for FAD a

three-exponential free lifetime fit was used. For the FLIRR images, the pixel information of two different independent spectral channels must be calculated, which was done using a Matlab program (see Section 3.2). The images of the metabolic NAD(P)H index and FLIRR1 reveals clear different lifetime distribution histograms between the two cell lines, whereas no notable differences in case of FLIRR2 and FLIRR3 were found. Compared to the metabolic NAD(P)H index, the image of FLIRR1 demonstrates a clear difference for the two cell lines not only with respect to the mean numbers, but also to the distribution pattern within the cells.

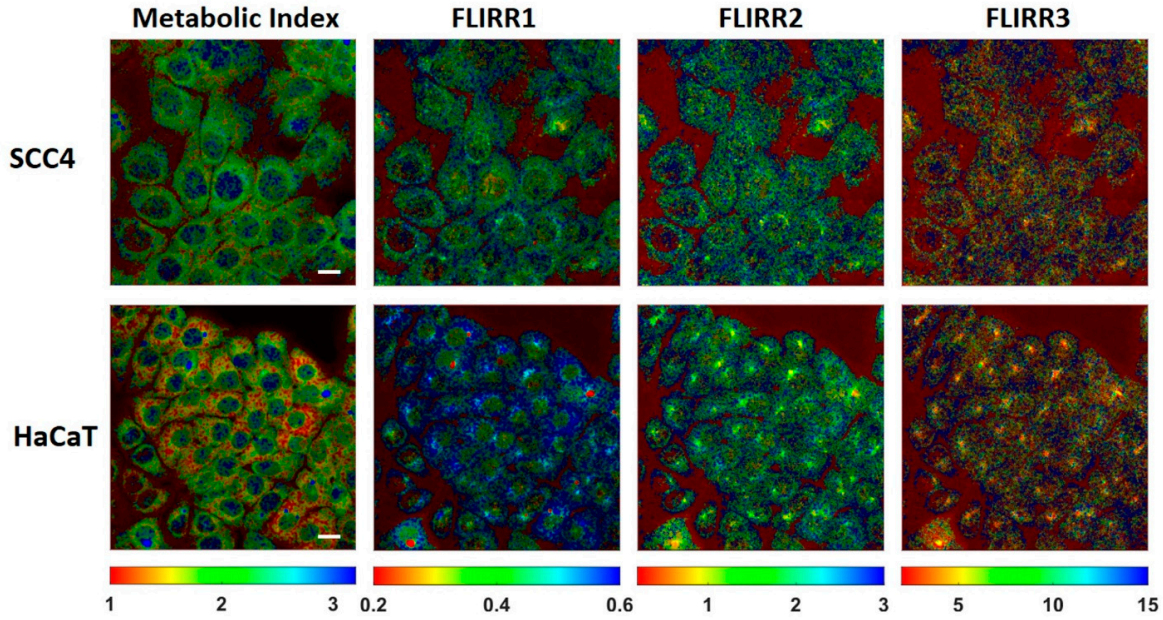

Figure 3. Images of the intracellular distribution of the metabolic NAD(P)H index and FLIRR1, FLIRR2, FLIRR3 indices within HaCaT and SCC4 cells. Scale bar 20 µm.

In conclusion, we could clearly demonstrate significant differences of both metabolic NAD(P)H index and the FLIRR1 index in HaCaT as compared to SCC4 cells. In order to demonstrate if this is valid in a cell model with more complexity, we cocultured HaCaT and SCC4 cells as described in materials and methods.

Figure 4 demonstrates FLIM images of NAD(P)H and flavins in HaCaT/SCC4 cocultures. Cells could also be distinguished by their morphological appearances and lifetime distribution. The red circle indicates a cluster of HaCaT cells where a punctuated fluorescence was observed in the flavin channel. In correlation with the results in monocultures, the mean lifetime of NAD(P)H was significantly longer in HaCaT as compared to SCC4 cells. The difference of the mean lifetime of flavins was less significant (see Table 6). From Table 6, the metabolic index was significantly decreased for the HaCaT cells ($p = 0.012$). Also, the increase of the FLIRR1 index was significant ($p = 0.007$), which correlates with the results in monocultures. Figure 5 demonstrates images of the intracellular distribution of the metabolic NAD(P)H index and the FLIRR1 index. A Matlab routine was described in materials and methods which was used to calculate the FLIRR1 image. Both imaging procedures enabled a clear discrimination between the different cell types. A punctuated appearance was found within the FLIRR1 distribution in the HaCaT cells.

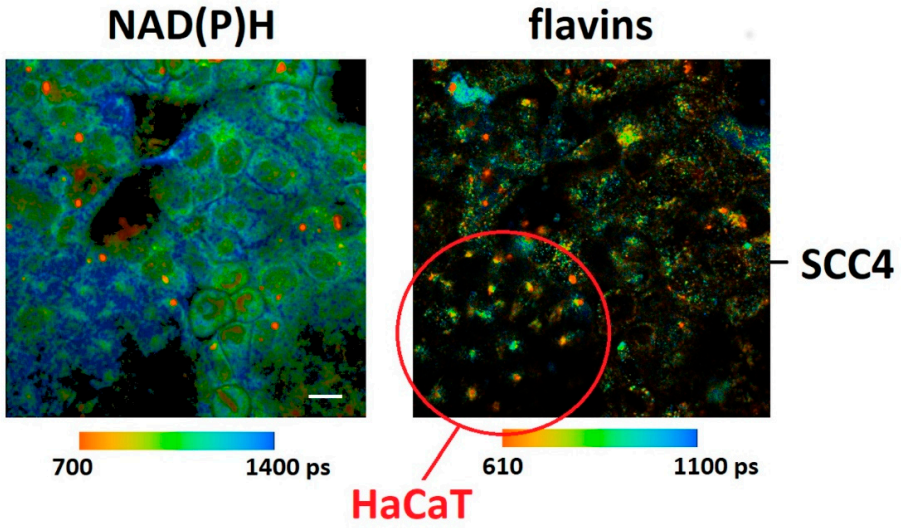

Figure 4. Fluorescence lifetime images of co-cultured HaCaT and SCC4 cells. The autofluorescence of NAD(P)H was recorded in the "green" (426–446 nm) spectral channel under 780 nm two-photon excitation whereas the autofluorescence of flavins was collected in the "red" (542–582 nm) spectral channel under 880 nm two-photon excitation. Scale bar 20 µm.

Table 6. Mean fluorescence lifetime, metabolic index and FLIRR1 for NAD(P)H and flavins within co-cultivated HaCaT and SCC4 cells. NAD(P)H fluorescence decay was fitted biexponentially with fixed lifetimes τ_1 = 400 ps and τ_2 = 2.5 ns, the flavin fluorescence decay was fitted three exponentially with free lifetimes τ_i.

	NAD(P)H τ_{mean} (ps)	Flavins τ_{mean} (ps)	Metabolic Index (NAD(P)H a_1/NAD(P)H a_2)	FLIRR1 (NAD(P)H a_2/flavins a_1)
HaCaT	1154 ± 51	704 ± 90	1.8 ± 0.2	0.49 ± 0.03
SCC4	1099 ± 47	673 ± 89	2.0 ± 0.2	0.46 ± 0.03

The statistical significance between HaCaT and SCC4 cell lines was evaluated using one-way ANOVA test. The *p*-value was 0.012 for the metabolic index and 0.007 for FLIRR1.

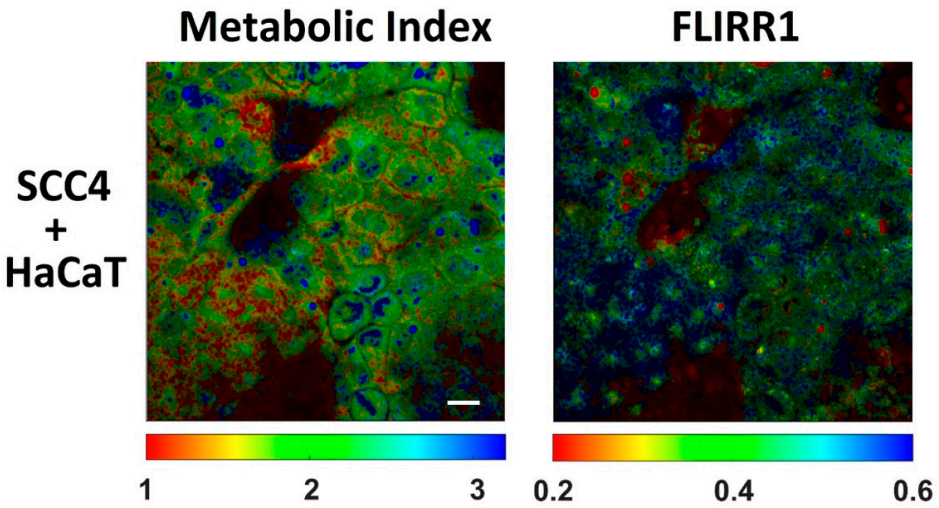

Figure 5. Intracellular distribution of the metabolic index and the redox ratio FLIRR1 within co-cultured HaCaT and SCC4 cells. Scale bar 20 µm.

3. Materials and Methods/Experimental

3.1. FLIM of NAD(P)H and Flavins

The FLIM technique for NAD(P)H and flavins was based on multiphoton laser scanning microscopy in combination with advanced multidimensional TCSPC technique. A femtosecond pulsed Mai Tai AX HPDS titanium-sapphire laser (Spectra Physics, Darmstadt, Germany) was used for two-photon excitation. The laser has a repetition rate of 80 MHz and a tuning range from 690 to 1040 nm. The maximum optical output power was about 3 W at 800 nm, and the temporal pulse width was below 100 fs. The laser pulses were modulated by controlling the optoacoustic modulator (AOM) of the laser scanning microscope (LSM 710 NLO, Carl Zeiss, Jena, Germany) by a TCSPC system generated signal.

The non-descanned detection (NDD) port of the microscope was used for the signal detection. The fluorescence signals were separated by the beam-splitter LP 490. The bandpass filters 436/20 nm and 562/40 nm (AHF Analysentechnik, Tübingen, Germany) were used to filter the emission signals. In regard to the installed emission BP filter 355–690 nm, we have defined the spectral channels as 426–446 nm ("green" channel) and 542–582 nm ("red" channel) and used them for the detection of NAD(P)H and flavin fluorescence, respectively. The HPM-100-40 hybrid detectors (Becker & Hickl GmbH, Berlin, Germany) with a detection wavelength range from 300–700 nm were used in both channels.

The autofluorescence originating from NAD(P)H and flavins was excited by two-photon excitation at 780 nm and 880 nm, respectively. Since Mai Tai AX HPDS titanium-sapphire laser does not emit two excitation wavelengths simultaneously, we performed FLIM measurements consecutively and not concurrently with two times scanning of the investigated cell area. Firstly, the flavins were excited at 880 nm, which was followed by laser irradiation at 780 nm, which excites both flavins and NAD(P)H (see Figure 2). This order of excitation has been chosen because it induces minimal impact on the cells. Also, the reverse order of excitation (first 780 nm and then 880 nm) did not change the results significantly (data not shown).

The laser power of the microscope was reduced by the internal AOM of the LSM 710 and measured to be 10 mW in the sample plane. A resolution of 512 × 512 pixels with 256 time-channels in each pixel was selected for the primary data collection. The scanning was performed at a frame time of 7.75 s that corresponds to a pixel dwell time of 6.30 µs. The total acquisition time was maintained at 1 min. The objective lens used was an EC Plan-Apochromat 40×/1.3 oil (Carl Zeiss, Germany) with a scan area of 212.1 µm × 212.1 µm and zoom 1.

3.2. FLIM Data Analysis

The fluorescence lifetime imaging data were collected in SPCM64 software and thereafter sent to SPCImage software (version 8.1, Becker & Hickl GmbH, Berlin, Germany) for processing. The FLIM data of the NAD(P)H autofluorescence within the "green" (426–446 nm) spectral channel and the flavins autofluorescence within the "red" (542–582 nm) spectral channel (see Figure 2) were analyzed by fitting the fluorescence decay curve to a multi-component exponential incomplete model with a WLS fit method. For NAD(P)H, a two-exponential incomplete model $I(t) = a_1\, e^{-t/\tau_1} + a_2\, e^{-t/\tau_2}$ was used, where I(t) is the fluorescence intensity at time t, τ_1 and τ_2 are the fluorescence lifetimes of the first and second component, corresponding to unbound and bound NAD(P)H, a_1 and a_2 are the associated relative amplitudes. For the estimation of the mean lifetime (τ_{mean}) calculated as $(a_1 \times \tau_1 + a_2 \times \tau_2)/(a_1 + a_2)$, the fixed lifetimes τ_1 = 400 ps and τ_2 = 2500 ps were chosen in accordance with literature reports [33]. For the flavin's autofluorescence, a three-exponential incomplete model $I(t) = a_1\, e^{-t/\tau_1} + a_2\, e^{-t/\tau_2} + a_3\, e^{-t/\tau_3}$ was used. τ_1 was correlated to bound FAD, τ_2 to unbound FAD and τ_3 mainly to bound FMN; a_1, a_2 and a_3 are the relative amplitudes. In all calculations, the total number of photons per trace was increased by maintaining a spatial binning factor of 2.

To establish the metabolic index and FLIRR distribution images, the relative amplitudes of the decay components and the photon counts per pixel of the respective FLIM

data was exported from the SPCImage software after image analysis of the NAD(P)H and FAD channels as two-dimensional data matrices and imported in the Matlab software (The MathWorks Inc., Natick, MA, USA; Version 2018b) for the generation of the false color images. The method to generate the metabolic index and FLIRR false color images is described in the Supplementary Figure S1.

The metabolic index and extended FLIRR indexes were calculated by means of implementing the following formulas in Matlab:

$$\text{Metabolic Index} = \frac{\text{NAD(P)H}_{a_1\%}}{\text{NAD(P)H}_{a_2\%}}$$

$$\text{FLIRR1} = \frac{\text{NAD(P)H}_{a_2\%}}{\text{FAD}^{+}{}_{a_1\%}}$$

$$\text{FLIRR2} = \frac{\text{NAD(P)H}_{a_2\%}}{\text{FAD}^{+}{}_{a_2\%}}$$

$$\text{FLIRR3} = \frac{\text{NAD(P)H}_{a_2\%}}{\text{FAD}^{+}{}_{a_3\%}}$$

A colormap was applied to the resulting matrices, each representing one index described above to create false color images. The false color images were then superimposed with the inverted intensity images (photon counts) from the 780 nm excitation NAD(P)H channel to generate a metabolic index distribution image and from 880 nm excitation flavins channel to generate all FLIRR distribution images.

3.3. Cell Culture Studies

We analyzed the FLIM data, FLIRR and the redox state within two different cell models, the human oral squamous carcinoma cell SCC4 (ATCC-Nr. CRL-1624) and the immortalized keratinocyte cell line HaCaT. SCC4 are reported to be fatty acid induced chemotherapy resistant and invasively growing [35], were cultivated in a nutrient mixture F-12 medium (DMEM/F-12, Thermo Fisher Scientific, Waltham, MA USA) supplemented with 1% GlutaMAX™ (Thermo Fisher Scientific, Waltham, MA USA), 400 mg/mL hydrocortisone (Sigma-Aldrich, St. Louis, MO, USA) and 10% fetal bovine serum (FBS) (Biochrom GmbH, Berlin, Germany) at 37 °C and 5.0% CO_2. For this kind of tumor, a glycolytic mechanism is expected which we tried to confirm by the FLIRR analysis. On the other hand, we cultivated the spontaneously transformed aneuploid immortalized keratinocyte cell line obtained from the adult healthy human skin HaCaT, which was grown in DMEM with 4,5 g/L glucose (Thermo Fisher Scientific, Waltham, MA, USA) supplemented with 1% GlutaMAX™ and 10% fetal bovine serum (FBS) at 37 °C and 5.0% CO_2. For microscopy, the cells were seeded on the glass bottom of a 24-well dish (Cellvis, Sunnyvale, CA, USA) at a cell density of 2×10^4 cells/well for SCC4 and 1×10^4 cells/well for HaCaT. The cells were grown for 48 h in the incubator at 37 °C and 5.0% CO_2. Microscopic measurements were performed at 37 °C in Tyrode's buffer (135 mM NaCl, 5 mM KCl, 1 mM $MgCl_2$, 1.8 mM $CaCl_2$, 20 mM HEPES, 5 mM glucose, pH 7.4).

In addition to the monocultures, we cocultured the HaCaT and SCC4 cells, seeding them sequentially in 24-well dishes on glass bottom at a density of 1×10^4 cells each. Before seeding, the wells were coated for 60 min at 37 °C with poly-L-lysin. For the cocultures, DMEM medium with 4.5 g/L glucose supplemented with 1% GlutaMAX™ and 10% FBS was used. The cells were grown for 48 h in the incubator at 37 °C and 5.0% CO_2. Microscopic measurements were performed at 37 °C in Tyrode's buffer.

3.4. Statistical Analysis

The statistical evaluation was performed using the software Origin(Pro), 2019b (64-bit, 9.6.5.169) (OriginLab Corporation, Northampton, MA, USA). First, a Shapiro–Wilk normality test was used to check the Gaussian distribution of the datasets. For all FLIM

data, a normal distribution was checked and confirmed. Thereafter, a one-way ANOVA test with Bonferroni mean comparison tests were used for the determination of statistical significance between the mean of datasets from two different live cell lines. The statistically significant normal distributions of two populations were predefined with a significance level of 0.05. For the data analysis, we used three different samples from three independent measurement days to obtain a total of 16 fluorescence lifetime imaging measurements for every spectral channel in each live cell type. Each fluorescence lifetime image contained approximately 40–60 live cells in case of HaCaT or 25–40 live cells in case of the larger SCC4. We estimated the fluorescence lifetime parameters such as mean lifetime (τ_m), lifetime of each fluorescing component (τ_i) and relative amount of each fluorescing component (a_i) from the entire fluorescence lifetime image. The fluorescent signal includes fluorescence from all intracellular compartments such as cytoplasm, mitochondria, etc. (see Figures 3–5). Since FLIM measurements of intrinsic autofluorescence are extremely susceptible to interference, we did not use additional counterstaining with further fluorescent dyes. Therefore, we applied FLIM measurements only to unstained cells.

4. Summary and Conclusions

Metabolic FLIM is now widely accepted to be one of the most powerful techniques to image bioenergetic status and changes in cells and tissue. However, the correct interpretation of the results could be difficult. Whereas an attribution of the lifetimes as an indicator for cell metabolism is mainly accepted, it is debated if this is valid for the redox state of cells. With respect to NAD(P)H FLIM this is true only for special conditions, if the NADH/NAD^+ pool is stable and careful interpretation of the redox state is needed when comparing the fluorescence lifetime of different cell systems [3–6]. Therefore, new algorithms are developed to circumvent these problems and to image cell metabolism and redox state from fluorescence lifetimes in complex cellular systems.

Innovative ideas have been evaluated using the lifetime components of FAD together with NAD(P)H (see for example reference [2]). Recently, the fluorescence lifetime induced redox ratio (FLIRR) where FLIM results of NAD(P)H and FAD are correlated were successfully introduced [9]. It was demonstrated that in the FLIRR index, the relative amount of bound NAD(P)H divided by the relative amount of bound FAD increases during OXPHOS and correlates with a higher oxidative state. However, contradictory results were also reported, claiming detailed interpretations. FLIM of FAD could be especially complicated. In contrast to NAD(P)H, the fluorescence lifetime of the protein-bound FAD is shorter compared to the free FAD [20,21]. For free FAD in aqueous buffer solution, a heterogeneous fluorescence intensity decay with two major lifetime components was reported—a dominant ultrafast 7 ps component and a 2.7 ns component interpreted as moderate fluorescence quenching [14,25,26]. Moreover, the fluorescence decay has been attributed to two molecular conformations as stacked and opened forms and FAD fluorescence lifetime was found to be pH dependent that increases complexity of interpretation inside cells [26,28]. Depending on the fitting procedure and experimental conditions, different lifetime components and values were found for FAD in various cell types. Whereas in prostate cancer cells two-exponential fitting led to two components with 120 ps and 3.38 ns [9], the lifetime τ_1 for protein-bound FAD and τ_2 for free FAD in Kasumi-1 cells was reported to be around 400 ps and 2.4 ns, respectively [23]. In isolated cardiomyocytes, a three-exponential fitting model let to 200 ps, 870 ps and 2.81 ns, respectively, with associated amplitudes at 71.8, 17.2, and 11.0 [11]. In general, the lifetime of protein-bound FAD was reported to be within 80–700 ps for living cells [9,11,26]. Within our measurements, high values of the pre-exponential factor a_1 which shows the relative contribution of the first component of the fitting model, supports the correlation with bound FAD, as FAD mostly exists as a part of flavoproteins in living systems [36,37].

From the discussion above, FAD FLIM is found to be a complex and correct interpretation of metabolic parameters can be challenging. Moreover, one component was neglected so far; namely, contributions from FMN during FAD detection. Our aim was therefore

to investigate the simultaneous evaluation of the fluorescence lifetime of NAD(P)H, FAD and FMN for advanced metabolic FLIM. Where FAD with respect to FLIRR mainly has its function in complex II of the respiratory chain, FMN is involved in complex I. FMN shows reverse fluorescence lifetime characteristics as compared to FAD, with an exceptionally long lifetime for protein bound FMN (see Figure 1) which must be considered in the metabolic FLIM investigation. Although the concentration of FMN is normally below FAD, the ratio depends on the cell type [29] and the fluorescence quantum yield of FMN is approx. 10 times higher as compared to FAD [30]. Interestingly, the estimation of the fluorescence brightness seen in the FAD channel is not dominated by protein bound FAD. In contrast, the fluorescence intensities (q-values) were highest for FMN, with a significant difference between the two cells (data not shown). Due to this, we extended the FLIRR index approach and evaluated FLIRR1, FLIRR2 and FLIRR3 after three-exponential fitting of the flavin signal. FLIRR1 relates bound NAD(P)H to bound FAD, FLIRR2 bound NAD(P)H to free FAD and FLIRR3 bound NAD(P)H to FMN. The significance of the result was compared to the metabolic NAD(P)H index that relates free NAD(P)H to bound NAD(P)H. We could clearly demonstrate a significant difference between HaCaT keratinocytes and SCC4 cells for the metabolic NAD(P)H and FLIRR1 index in monocultures, as well as cocultures. FLIRR1 was significantly different for both fitting procedures (free and fixed flavin lifetimes), whereas FLIRR2 and FLIRR3 revealed significance only for the free fitting calculations. Moreover, the FLIRR1 index was statistically higher than the NAD(P)H metabolic index in monocultures, as well as cocultures. We conclude that FLIRR1 is the most significant in cocultures, although the NAD(P)H fluorescence lifetime is significantly different, but not the flavin lifetime. This underlines the importance of relating the exponential coefficients of both NAD(P)H and FAD for the evaluation of metabolic differences between tumor and normal cells. In addition, the images of FLIRR1 reveals a clear difference between the two cell lines, as evident from the calculated values (histogram), as well as the intracellular distribution pattern.

In summary, FLIRR1 was evaluated to demonstrate the most significant difference in metabolic imaging between HaCaT keratinocytes and SCC4 cells. This indicates that protein bound NAD(P)H and protein bound FAD mainly impacts the metabolic differences in both cell types. Although free FAD and FMN are also significantly different in the two cells (see Tables 1 and 2), their relative contribution to the metabolic signal is small. However, this does not indicate that the fluorescence brightness seen in the FAD channel is dominated by the protein bound FAD. In contrast, as outlined above, the largest contribution originates from FMN that exhibits the highest fluorescence quantum yield.

Supplementary Materials: The following are available online at https://www.mdpi.com/article/10.3390/ijms22115952/s1. Supplementary Figure S1. Flow diagram of workflow to establish the metabolic index and FLIRR 1, FLIRR 3 and FLIRR 3 false color images.

Author Contributions: All authors contributed to the conceptualization, writing, and editing of this manuscript. All authors have read and agreed to the published version of the manuscript.

Funding: This research received funding from the Ministry of Research and Development (see Acknowledgements).

Institutional Review Board Statement: Not applicable.

Informed Consent Statement: Not applicable.

Data Availability Statement: The data presented in this study are available on request from the corresponding author. The data are not publicly available due to privacy.

Acknowledgments: This work is currently supported by the Ministry of Research and Development, FKZ order: 13N14508 ("OMOXI"). The authors thank the Ulm University Center for Translational Imaging MoMAN for its support.

Conflicts of Interest: The authors declare no conflict of interest.

Abbreviations

AOM	optoacoustic modulator
FAD	flavin adenine dinucleotide
FLIM	fluorescence lifetime imaging
FLIRR	fluorescence lifetime induced redox ratio
FMN	flavin mononucleotide
NAD(P)H	**reduced** nicotinamide adenine dinucleotide (phosphate)
OXPHOS	oxidative phosphorylation
TCSPC	time-correlated single photon counting

References

1. Becker, W. *Advanced Time-Correlated Single Photon Counting Applications*; Springer Series in Chemical Physics; Springer International Publishing: Berlin, Germany, 2015; ISBN 978-3-319-14928-8.
2. Datta, R.; Heaster, T.M.; Sharick, J.T.; Gillette, A.A.; Skala, M.C. Fluorescence Lifetime Imaging Microscopy: Fundamentals and Advances in Instrumentation, Analysis, and Applications. *J. Biomed. Opt.* **2020**, *25*, 1. [CrossRef]
3. Yuan, X.; Liu, Y.; Bijonowski, B.M.; Tsai, A.-C.; Fu, Q.; Logan, T.M.; Ma, T.; Li, Y. NAD+/NADH Redox Alterations Reconfigure Metabolism and Rejuvenate Senescent Human Mesenchymal Stem Cells in Vitro. *Commun. Biol.* **2020**, *3*, 774. [CrossRef] [PubMed]
4. Quinn, K.P.; Sridharan, G.V.; Hayden, R.S.; Kaplan, D.L.; Lee, K.; Georgakoudi, I. Quantitative Metabolic Imaging Using Endogenous Fluorescence to Detect Stem Cell Differentiation. *Sci. Rep.* **2013**, *3*, 3432. [CrossRef] [PubMed]
5. Heikal, A.A. Intracellular Coenzymes as Natural Biomarkers for Metabolic Activities and Mitochondrial Anomalies. *Biomark. Med.* **2010**, *4*, 241–263. [CrossRef]
6. Schaefer, P.M.; Hilpert, D.; Niederschweiberer, M.; Neuhauser, L.; Kalinina, S.; Calzia, E.; Rueck, A.; von Einem, B.; Arnim, C.A.F. von Mitochondrial Matrix PH as a Decisive Factor in Neurometabolic Imaging. *Neurophotonics* **2017**, *4*, 045004. [CrossRef]
7. Yu, Q.; Heikal, A.A. Two-Photon Autofluorescence Dynamics Imaging Reveals Sensitivity of Intracellular NADH Concentration and Conformation to Cell Physiology at the Single-Cell Level. *J. Photochem. Photobiol. B* **2009**, *95*, 46–57. [CrossRef]
8. Liu, Z.; Pouli, D.; Alonzo, C.A.; Varone, A.; Karaliota, S.; Quinn, K.P.; Münger, K.; Karalis, K.P.; Georgakoudi, I. Mapping Metabolic Changes by Noninvasive, Multiparametric, High-Resolution Imaging Using Endogenous Contrast. *Sci. Adv.* **2018**, *4*, eaap9302. [CrossRef]
9. Alam, S.R.; Wallrabe, H.; Svindrych, Z.; Chaudhary, A.K.; Christopher, K.G.; Chandra, D.; Periasamy, A. Investigation of Mitochondrial Metabolic Response to Doxorubicin in Prostate Cancer Cells: An NADH, FAD and Tryptophan FLIM Assay. *Sci. Rep.* **2017**, *7*, 10451. [CrossRef] [PubMed]
10. Blacker, T.S.; Mann, Z.F.; Gale, J.E.; Ziegler, M.; Bain, A.J.; Szabadkai, G.; Duchen, M.R. Separating NADH and NADPH Fluorescence in Live Cells and Tissues Using FLIM. *Nat. Commun.* **2014**, *5*, 3936. [CrossRef]
11. Chorvat, D.; Chorvatova, A. Spectrally Resolved Time-Correlated Single Photon Counting: A Novel Approach for Characterization of Endogenous Fluorescence in Isolated Cardiac Myocytes. *Eur. Biophys. J.* **2006**, *36*, 73–83. [CrossRef]
12. Lakowicz, J.R.; Szmacinski, H.; Nowaczyk, K.; Johnson, M.L. Fluorescence Lifetime Imaging of Free and Protein-Bound NADH. *Proc. Natl. Acad. Sci.* **1992**, *89*, 1271–1275. [CrossRef]
13. Penjweini, R.; Roarke, B.; Alspaugh, G.; Gevorgyan, A.; Andreoni, A.; Pasut, A.; Sackett, D.L.; Knutson, J.R. Single Cell-Based Fluorescence Lifetime Imaging of Intracellular Oxygenation and Metabolism. *Redox Biol.* **2020**, *34*, 101549. [CrossRef]
14. van den Berg, P.A.W.; Feenstra, K.A.; Mark, A.E.; Berendsen, H.J.C.; Visser, A.J.W.G. Dynamic Conformations of Flavin Adenine Dinucleotide: Simulated Molecular Dynamics of the Flavin Cofactor Related to the Time-Resolved Fluorescence Characteristics. *J. Phys. Chem. B* **2002**, *106*, 8858–8869. [CrossRef]
15. Visser, A. Time-Resolved Fluorescence Studies on Flavins. In *Fluorescent Biomolecules*; Jameson, D.M., Reinhart, G.D., Eds.; Springer US: Boston, MA, USA, 1989; pp. 319–341. ISBN 978-1-4684-5621-9.
16. Bird, D.K.; Yan, L.; Vrotsos, K.M.; Eliceiri, K.W.; Vaughan, E.M.; Keely, P.J.; White, J.G.; Ramanujam, N. Metabolic Mapping of MCF10A Human Breast Cells via Multiphoton Fluorescence Lifetime Imaging of the Coenzyme NADH. *Cancer Res.* **2005**, *65*, 8766–8773. [CrossRef] [PubMed]
17. Pastore, M.N.; Studier, H.; Bonder, C.S.; Roberts, M.S. Non-Invasive Metabolic Imaging of Melanoma Progression. *Exp. Dermatol.* **2017**, *26*, 607–614. [CrossRef] [PubMed]
18. Shirmanova, M.V.; Druzhkova, I.N.; Lukina, M.M.; Dudenkova, V.V.; Ignatova, N.I.; Snopova, L.B.; Shcheslavskiy, V.I.; Belousov, V.V.; Zagaynova, E.V. Chemotherapy with Cisplatin: Insights into Intracellular PH and Metabolic Landscape of Cancer Cells in Vitro and in Vivo. *Sci. Rep.* **2017**, *7*, 8911. [CrossRef] [PubMed]
19. Walsh, A.J.; Skala, M.C. Optical Metabolic Imaging Quantifies Heterogeneous Cell Populations. *Biomed. Opt. Express* **2015**, *6*, 559–573. [CrossRef]
20. Chosrowjan, H.; Taniguchi, S.; Mataga, N.; Nakanishi, T.; Haruyama, Y.; Sato, S.; Kitamura, M.; Tanaka, F. Effects of the Disappearance of One Charge on Ultrafast Fluorescence Dynamics of the FMN Binding Protein. *J. Phys. Chem. B* **2010**, *114*, 6175–6182. [CrossRef] [PubMed]

21. Mataga, N.; Chosrowjan, H.; Shibata, Y.; Tanaka, F.; Nishina, Y.; Shiga, K. Dynamics and Mechanisms of Ultrafast Fluorescence Quenching Reactions of Flavin Chromophores in Protein Nanospace. *J. Phys. Chem. B* **2000**, *104*, 10667–10677. [CrossRef]
22. Chakraborty, S.; Nian, F.-S.; Tsai, J.-W.; Karmenyan, A.; Chiou, A. Quantification of the Metabolic State in Cell-Model of Parkinson's Disease by Fluorescence Lifetime Imaging Microscopy. *Sci. Rep.* **2016**, *6*, 19145. [CrossRef]
23. Skala, M.C.; Riching, K.M.; Gendron-Fitzpatrick, A.; Eickhoff, J.; Eliceiri, K.W.; White, J.G.; Ramanujam, N. In Vivo Multiphoton Microscopy of NADH and FAD Redox States, Fluorescence Lifetimes, and Cellular Morphology in Precancerous Epithelia. *Proc. Natl. Acad. Sci.* **2007**, *104*, 19494–19499. [CrossRef] [PubMed]
24. Kunz, W.S.; Kunz, W. Contribution of Different Enzymes to Flavoprotein Fluorescence of Isolated Rat Liver Mitochondria. *Biochim. Biophys. Acta BBA Gen. Subj.* **1985**, *841*, 237–246. [CrossRef]
25. Nakabayashi, T.; Islam, M.S.; Ohta, N. Fluorescence Decay Dynamics of Flavin Adenine Dinucleotide in a Mixture of Alcohol and Water in the Femtosecond and Nanosecond Time Range. *J. Phys. Chem. B* **2010**, *114*, 15254–15260. [CrossRef] [PubMed]
26. Islam, M.S.; Honma, M.; Nakabayashi, T.; Kinjo, M.; Ohta, N. PH Dependence of the Fluorescence Lifetime of FAD in Solution and in Cells. *Int. J. Mol. Sci.* **2013**, *14*, 1952–1963. [CrossRef]
27. Esposito, R.; Delfino, I.; Portaccio, M.; Iannuzzi, C.; Lepore, M. An Insight into PH-Induced Changes in FAD Conformational Structure by Means of Time-Resolved Fluorescence and Circular Dichroism. *Eur. Biophys. J.* **2019**, *48*, 395–403. [CrossRef]
28. Sato, K.; Nishina, Y.; Shiga, K.; Tanaka, F. Hydrogen-Bonding Dynamics of Free Flavins in Benzene and FAD in Electron-Transferring Flavoprotein upon Excitation. *J. Photochem. Photobiol. B* **2003**, *70*, 67–73. [CrossRef]
29. Hühner, J.; Ingles-Prieto, Á.; Neusüß, C.; Lämmerhofer, M.; Janovjak, H. Quantification of Riboflavin, Flavin Mononucleotide, and Flavin Adenine Dinucleotide in Mammalian Model Cells by CE with LED-Induced Fluorescence Detection: CE and CEC. *Electrophoresis* **2015**, *36*, 518–525. [CrossRef]
30. Islam, S.D.M.; Susdorf, T.; Penzkofer, A.; Hegemann, P. Fluorescence Quenching of Flavin Adenine Dinucleotide in Aqueous Solution by PH Dependent Isomerisation and Photo-Induced Electron Transfer. *Chem. Phys.* **2003**, *295*, 137–149. [CrossRef]
31. Visser, A.J.W.G. Kinetics of Stacking Interactions in Flavin Adenine Dinucleotide from Time-Resolved Flavin Fluorescence. *Photochem. Photobiol.* **1984**, *40*, 703–706. [CrossRef]
32. Wahl, P.; Auchet, J.C. Time Resolved Fluorescence of Flavin Adenine Dinucleotide. *FEBS Lett.* **1974**, *44*, 67–70. [CrossRef]
33. Kalinina, S.; Breymayer, J.; Schäfer, P.; Calzia, E.; Shcheslavskiy, V.; Becker, W.; Rück, A. Correlative NAD(P)H-FLIM and Oxygen Sensing-PLIM for Metabolic Mapping. *J. Biophotonics* **2016**, *9*, 800–811. [CrossRef] [PubMed]
34. Kalinina, S.; Breymayer, J.; Reeß, K.; Lilge, L.; Mandel, A.; Rück, A. Correlation of Intracellular Oxygen and Cell Metabolism by Simultaneous PLIM of Phosphorescent TLD1433 and FLIM of NAD(P)H. *J. Biophotonics* **2018**, *11*, e201800085. [CrossRef] [PubMed]
35. Agostini, M.; Silva, S.D.; Zecchin, K.G.; Coletta, R.D.; Jorge, J.; Loda, M.; Graner, E. Fatty Acid Synthase Is Required for the Proliferation of Human Oral Squamous Carcinoma Cells. *Oral Oncol.* **2004**, *40*, 728–735. [CrossRef] [PubMed]
36. Ghisla, S.; Massey, V. Mechanisms of flavoprotein-catalyzed reactions. In *EJB Reviews 1989*; Christen, P., Hofmann, E., Eds.; EJB Reviews; Springer: Berlin/Heidelberg, Germany, 1989; pp. 29–45. ISBN 978-3-642-75189-9.
37. Mattevi, A. To Be or Not to Be an Oxidase: Challenging the Oxygen Reactivity of Flavoenzymes. *Trends Biochem. Sci.* **2006**, *31*, 276–283. [CrossRef]

Supplementary Materials

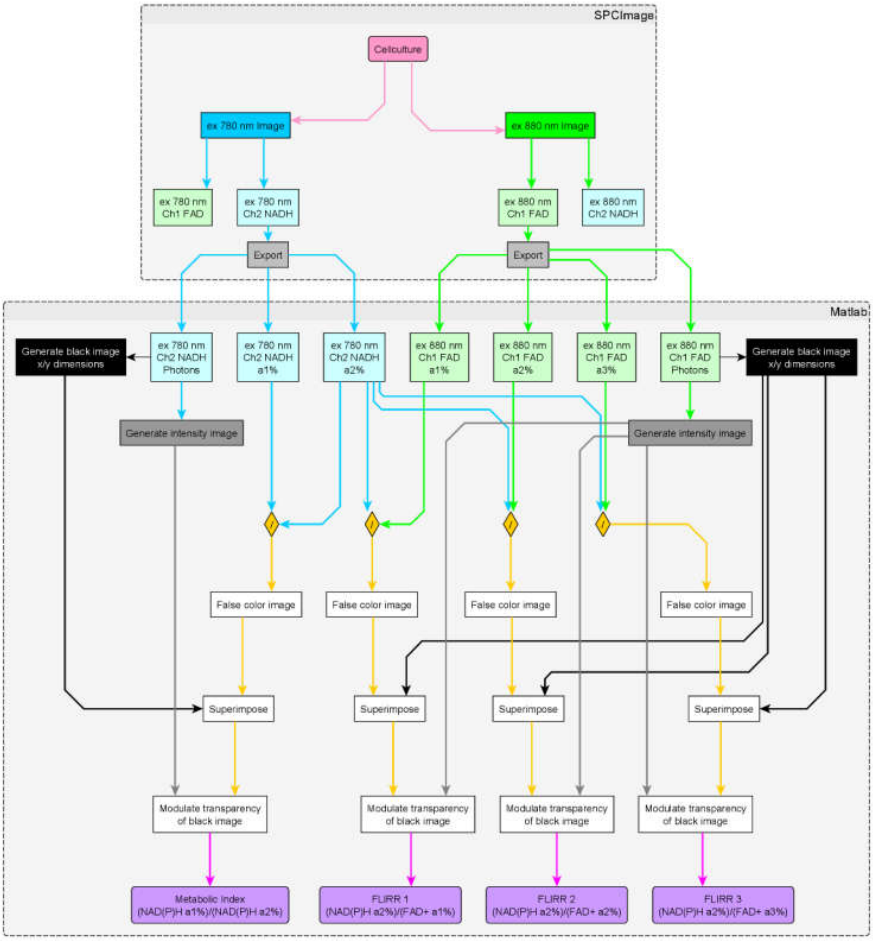

Supplementary Figure S1. Flow diagram of workflow to establish the metabolic index and FLIRR 1, FLIRR 3 and FLIRR 3 false color images. After completion of image analysis in SPCImage as described in section 3.2. "FLIM data analysis" the relative amplitudes of the fitfuncions to the NAD(P)H and FAD channels and the intensity image which represents the photon counts per pixel are exportet using the SPCImage export dialog. The exported data matrixes are importet into Matlab and the Metabolic Index and FLIRR 1 to 3 indizes calculated, according to the formulas described in section 3.2. A color map is applied to the resulting matrixes to create false color images which are then superimposed by the inverted intensity image to create the final images.

5.2 Quenched coumarin derivatives as fluorescence lifetime phantoms for NADH and FAD

C. Freymüller, S. Kalinina, A. Rück, R. Sroka und A. Rühm, "Quenched coumarin derivatives as fluorescence lifetime phantoms for NADH and FAD", *Journal of Biophotonics*, 8. Apr. 2021. DOI: 10.1002/jbio.202100024, JIF_{2021}: 3.390.

Kurzfassung: Die endogenen Fluorophore NADH und FAD sind aufgrund ihrer begrenzten Haltbarkeit und variablen, von Konzentration, pH-Wert, Oxidationszustand und Proteinbindung abhängigen, Fluoreszenzeigenschaften nicht als Referenzsystem für FLIM geeignet.
Über eine umfassende Literaturrecherche wurden Coumarin 1 und Cumarin 6 als geeignete Fluorophore zur Simulation der Fluoreszenzeigenschaften von NADH und FAD identifiziert. Die Auswahlkriterien waren die Anregbarkeit bei den für NADH und FAD zur metabolischen Bildgebung verwendeten Wellenlängen 780 nm und 880 nm und die Ähnlichkeit der Emissionsspektren zu NADH und FAD sowie monoexponentielles Abklingverhalten. Weitere Kriterien waren eine gleiche oder längere Fluoreszenzlebensdauer als gebundenens NADH (ca. 2500 ps) und freies FAD (ca. 2000 ps), sowie die Quenchbarkeit der Fluoreszenzlebensdauer. Diese Kriterien wurden von Coumarin 1 als Surrogat für NADH und Coumarin 6 als Surrogat für FAD mit 4-Hydroxy-TEMPO als Quencher erfüllt. Das für die Bestimmung der Quench-Eigenschaften von Coumarin 1 und Coumarin 6 verwendete Multiphotonen-FLIM -Mikroskop wurde mithilfe von in der Literatur bekannten Fluorophoren mit monoexponentiellem Abklingverhalten charakterisiert. Zusätzlich wurden die Fluoreszenzlebensdauern von freiem NADH und FAD in Lösung bestimmt und diese mit publizierten Werten verglichen. Es wurden die ungequenchten Fluoreszenzlebensdauern τ_0 von Coumarin 1, $\tau_0 = (2927{,}8 \pm 16{,}9)\,ps$, und Coumarin 6, $\tau_0 = (2478{,}8 \pm 36{,}1)\,ps$, bestimmt. Die Ergebnisse sind mit Literaturwerten vergleichbar (Coumarin 1 3100 ps [130]; Coumarin 6 $(2390 \pm 80)\,ps$ [131]). Zur Bestimmung der Fluoreszenzdynamik der Quenchproszesse von Coumarin 1 und 6 wurde die Abhängigkeit der Fluoreszenzlebensdauer von der Konzentrationen des Quenchers 4-Hydroxy-TEMPO (variiert von 0 $mol\,L^{-1}$ bis 0,415 $mol\,L^{-1}$) bei gleichbleibender Fluorophorkonzentration ermittelt. Die Fluorophorlösungen zeigten bei allen untersuchten Quencherkonzentrationen monoexponentielles Abklingverhalten. In Abhängigkeit der Quencherkonzentration wurde an die Fluoreszenzlebensdauer eine modifizierte Stern-Volmer-Gleichung angefittet, da das Quenchverhalten beider Fluorophore bei Quencherkonzentrationen größer 0,1 $\mathrm{mol\,L^{-1}}$ durch die unmodifizierte Stern-Volmer Gleichung [132, 133] nicht zufriedenstellend beschrieben wurde. Aus den erhaltenen Fitfunktionen wurden die notwendigen Quencherkonzentrationen zum Erreichen der Fluoreszenzlebensdauern von freiem und proteingebundenem NADH und FAD ermittelt. Als Ziel für die freien und proteingebundenen Fluoureszenzlebensdauern von NADH und FAD werden $\tau_{1_{frei}} \approx 400\,ps$ [27, 28] und $\tau_{2_{gebunden}} \approx 2500\,ps$ [134] für NADH und $\tau_{1_{gebunden}} \approx 100ps$ ($106ps$ [6], $< 100ps$ [81], $130ps$ [31]) beziehungsweise $\tau_{2_{frei}} \approx 2000ps$ ($2300\,ps$[4], $\tau_3 = 2090\,ps$ in Lösung [16], $2300\,ps - 2900\,ps$ [81]) für FAD verwendet.

Die Fluoreszenzlebensdauern der Coumarin 1 Lösungen als Surrogate für die freie und proteingebundene Form von NADH wurden bestimmt und mit den Zielvorgaben von 400 ps und 2500 ps verglichen. Die Messungen wurden zur Kontrolle mit erneut angemischten Lösungen wiederholt und die Langzeitstabilität der Fluorophorlösungen, einzeln und in

Kombination mit dem Quencher, nach 41 Tagen gekühlter Lagerung überprüft. Weiterhin erfolgte eine Diskussion der Rolle der Auswahloptionen für Parameter beim Fitprozess von TCSPC-Daten wie z.B. die mathematische Fitmethode, Binning und Threshold.

Die Lebensdauern der Surrogatlösungen für die freie und proteingebundene Form von FAD konnte aus organisatorischen Gründen am FLIM-Mikroskop der AG Rück nicht untersucht werden. Die erforderlichen Messungen wurden bei der AG Hellerer am Multiphoton Imaging Labor der Hochschule München für angewandte Wissenschaften durchgeführt [19]. Die Messungen zeigten, dass die kurze Fluoreszenzlebensdauer $100\,ps$ von freiem FAD mit der berechneten Quencherkonzentration nicht erreicht werden kann. Hier kann durch die Erhöhung der Quencherkonzentration versucht werden eine Annäherung zu erreichen oder es wird ein alternatives Fluorophor verwendet. Rose Bengal in wässeriger Lösung könnte hier, aufgrund der Fluoreszenzlebensdauer im Bereich von $78\,ps$ bis $140\,ps$ [135, 136, 137] eine Alternative darstellen [127].

Es konnte gezeigt werden, dass Lösungen aus gequenchtem Coumarin 1 und Coumarin 6 aufgrund ihrer einfachen Herstellung, relativ anspruchslosen Lagerungsbedingungen und ihrer Langzeitstabilität als Phantome für freies und proteingebundenes NADH und FAD geeignet sind.

Der Anteil von Christian Freymüllers an dem oben beschriebenen Manuskript war die Identifikation von Flurophoren, die sich als Phantome für NADH und FAD eignen. Hierzu erfolgte eine umfassende Recherche und Bewertung hinsichtlich Biokopatibilität, spektralen (Fluoreszenzanregung und Emissionsspektrum) und Fluoreszenzlebensdauereigenschaften einschließlich Quenchbarkeit im Rahmen eines Delphi-Verfahrens. Weiterhin oblag Herrn Freymüller die Planung und Durchführung aller Messungen an den hergestellten Fluorophorlösungen (spektral und Fluoreszenzlebensdauer) sowie deren Bewertung und die graphische Darstellung. Im Weiteren, führte Herr Freymüller die Auswertung der Fluoreszenzlebensdauerdaten (in Verbindung mit fachlicher Diskussion mit Sviatlana Kalinina), die Erstellung der Programme zur Berechnung der Stern-Vollmer-Koeffizienten und Konzentrationsverhältnisse der NADH und FAD Phantom-Lösungen durch. Die Erstellung des Manuskriptes erfolgte in Zusammenarbeit mit den Koautoren.

Received: 15 January 2021 | Revised: 22 February 2021 | Accepted: 12 March 2021

DOI: 10.1002/jbio.202100024

FULL ARTICLE

JOURNAL OF BIOPHOTONICS

Quenched coumarin derivatives as fluorescence lifetime phantoms for NADH and FAD

Christian Freymüller[1,2*] | **Sviatlana Kalinina**[3] | **Angelika Rück**[3] | **Ronald Sroka**[1,2] | **Adrian Rühm**[1,2]

[1]Laser-Forschungslabor, LIFE Center, University Hospital, LMU Munich, Planegg, Germany

[2]Department of Urology, University Hospital, LMU Munich, Munich, Germany

[3]Core Facility Confocal and Multiphoton Microscopy N24, University of Ulm, Ulm, Germany

***Correspondence**
Christian Freymüller, Laser-Forschungslabor, LIFE Center, University Hospital, LMU Munich, Fraunhoferstr. 20, 82152 Planegg, Germany.
Email: christian.freymueller@med.uni-muenchen.de

Funding information
German Ministry of Education and Research (BMBF), Grant/Award Number: 13N14507

Abstract

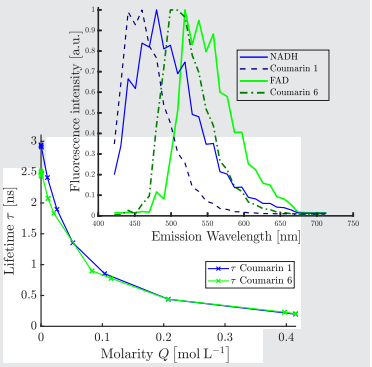

Two-photon fluorescence lifetime imaging is a versatile laboratory technique in the field of biophotonics and its importance is also growing in the field of in vivo diagnostics for medical purposes. After years of experience in dermatology, endoscopic implementations of the technique are now posing new technical challenges. To develop, test, and compare instrumental solutions for this purpose suitable reference samples have been devised and tested. These reference samples can serve as reliable NADH- and FAD-mimicking optical phantoms for 2-photon fluorescence lifetime imaging, as they can be prepared relatively easily with reproducible and stable characteristics for this quite relevant diagnostic technique. The reference samples (mixtures of coumarin 1 and coumarin 6 in ethanol with suitable amounts of 4-hydroxy-TEMPO) have been tuned to exhibit spectral and temporal fluorescence characteristics very similar to those of NADH and FAD, the two molecules most frequently utilized to characterize cell metabolism.

KEYWORDS

coumarin 1, coumarin 6, flavin adenine dinucleotide, fluorescence lifetime imaging microscopy, multiphoton microscopy, nicotinamide adenine dinucleotide, tissue phantom

1 | INTRODUCTION

Fluorescence lifetime imaging microscopy (FLIM) has developed into a versatile method and an integral constituent in biosciences and medicine. Especially imaging of NADH and FAD by means of two-photon FLIM grants new insight into cells and organisms since it allows for imaging the metabolic state of living cells, for example, in cell cultures or clinical applications, for example in dermatology [1]. To further exploit this valuable information for medical diagnostics (eg, in the form of FLIM endoscopy), new instrumentation (eg, by integration of FLIM capability into devices similar to multiphoton

This manuscript is part of the inaugural thesis of Christian Freymüller to be submitted to the Medical Faculty of LMU Munich.

systems described in References [2, 3]) and investigation protocols need to be devised. For the development, testing or comparison of medical diagnostic systems, it is usually necessary to evaluate a system by a defined calibration protocol/procedure. This is usually done by means of artificial optical phantoms or standards with clearly defined properties, instead of tissue samples or in vivo tissue whose optical properties vary from sample to sample, site to site, or patient to patient, thus rendering reproducible measurements impossible. Artificial optical phantoms with reproducible and tunable properties are necessary in order to ensure reproducibility, stability and comparability [4] of results obtained under different conditions or with different instrumentation (for example different research microscopes, systems comprising different detector types or components from different manufacturers, different software, or different classes of optical devices, for example, standard microscope objectives vs endoscopes.

Indeed, NADH and FAD for themselves prove to be unsuitable as standards for comparing different measurement systems because of their limited shelf life in solution and the dependence of their fluorescence characteristics on external conditions, such as pH value [5] and oxidative state (NADH fluorescence intensity decreases, FAD fluorescence intensity increases with oxidation, for example, within hours in solutions exposed to air). Furthermore, with regard to their protein-bound and unbound forms, pH value and concentration, the number of exponential functions and fluorescence lifetime values regarded as required to properly fit their fluorescence decay curves varies in literature in contrast to other substances proposed as standards, like Rose Bengal, 2,5-Diphenyloxazole (PPO), 1,4-Bis(5-phenyl-2-oxazolyl) benzene (POPOP), or anthracene. Such variations and uncertainties are not desired for a standard or reference sample that should deliver stable measurement results under different conditions.

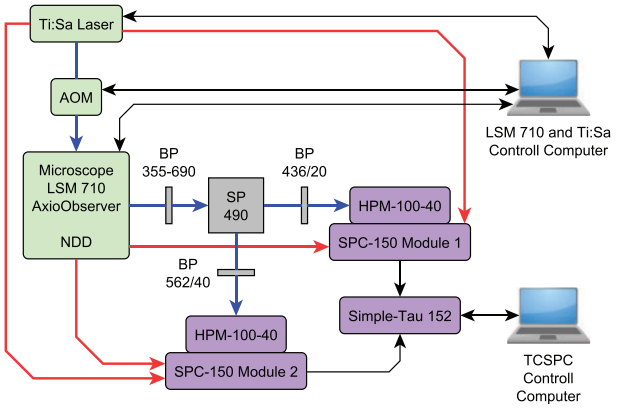

FIGURE 1 Schematics of fluorescence lifetime imaging microscopy (FLIM) measurement system; blue lines: optical paths; red lines: electrical synchronization connections; black lines: electrical control connections

2 | MATERIAL AND METHODS

2.1 | Experimental setup for two-photon FLIM

The employed instrumental setup [6], equipped with different optical filters, is shown in Figure 1. It consists of a multiphoton laser scanning microscope (LSM 710 NLO, Carl Zeiss Microscopy GmbH, Jena, Germany) combined with a time-correlated single-photon counting (TCSPC) system based on two HPM-100-40 detectors (Becker & Hickl GmbH, Berlin, Germany), attached to a non-descanned (NDD) sideport of the LSM 710, and a Simple-TAU 152 TCSPC system, controlled by a separate computer running SPCM Ver. 9.61 32 Bit (Becker & Hickl GmbH, Berlin, Germany). For two-photon excitation, a pulsed femtosecond titanium-sapphire laser (Ti:Sa) (MaiTai AX HPDS, Spectra Physics, Darmstadt, Germany) was used, providing <100 fs pulse width and a wavelength tuning range of 690 to 1040 nm. The laser power entering the LSM 710 is adjusted by an acousto-optic modulator (AOM), controlled by the microscope software ZEN (Carl Zeiss Microscopy GmbH, Jena, Germany). It is expressed as a percentage (0%-100%), defined by the ratio of the light power leaving and entering the AOM, respectively. The absolute light power in the focal plane was measured using a powermeter (S130C with PM100D, Thorlabs Inc., Newton).

The generated fluorescence signal is cleaned up at the NDD port by a 355 to 690 nm bandpass filter, further separated by a 490 nm beam splitter, and directed to the SPC modules. For FAD and NADH detection, two SPC modules are used in combination with a 562/40 nm bandpass filter and a 436/20 nm bandpass filter (both AHF Analysentechnik, Tübingen, Germany) as described in Rück et al. [7], respectively. The instrumental setup used for the development of an NADH/FAD phantom was also used for experiments on cell cultures and chosen for compatibility and comparability.

Fluorophore solutions were filled into microscopy-suited channels (μ-Slide VI 0.4, Cat.No. 80606, ibidi GmbH, Gräfelfing, Germany) with a capacity of 40 μL per channel, closed by plugs (Luer Plug, Cat.No: 10822, ibidi, Gräfelfing, Germany) to minimize evaporation during measurements. All experiments were carried out at room temperature (22°C). Fluorescence lifetime measurements were performed at (200 ± 5) μm depth in the vertical center of the channels using an x20 objective

(Plan-Apochromat x20 NA 0.8 objective, Carl Zeiss Microscopy GmbH, Jena, Germany). The lateral position was reproducibly adjusted at least 1 mm from the side faces and at least 5 mm from the ends of the channels. The image size was 128 pixels × 128 pixels, corresponding to a 70.85 μm × 70.85 μm imaging area, and the pixel dwell time was 6.3 μs for all FLIM measurements. A constant imaging depth was accomplished by performing a confocal z-scan of every individual microslide channel in reflection mode with a 633 nm laser to find the lower and upper bounds of the individual channels (by using the Fresnel reflections caused by the different refractive indices of the fluorophore solutions and the slide material). The center of each channel was determined and saved using the positions mode of the microscope control software for subsequent use during the FLIM or spectral emission measurements. Emission spectra were recorded in the same planes as FLIM-data using the LSM 710's 31 channel spectral imaging unit with wavelength intervals of 9.7 nm and a spectral range of 417 to 718 nm. FLIM data evaluation and fitting was done with the software SPCImage 8.0 NG and 8.1 NG (Becker & Hickl, Berlin, Germany) using the incomplete-decay model function and weighted-least-square fitting for SPCImage's fluorescence lifetime fitting process. The mean value μ of the fluorescence lifetime distribution histogram generated by SPCImage was regarded as the fluorescence lifetime value τ for the respective measurement.

2.2 | Validation of FLIM-system

The FLIM system's correct function was validated by comparing the measured fluorescence lifetimes of six different fluorophore solutions with literature values. The fluorophores, excitation wavelengths, detection filters, concentrations, solvents, and the number of measurements per fluorophore are listed in Table 1.

The fluorophore solutions were filled into microscopy-suited channels as described above. The laser excitation power was chosen individually for each fluorophore, according to the specific fluorescence intensity, in order to protect the TCSPC detectors from overload/destruction. Data analysis was done using SPCImage individually for PPO and Rose Bengal, for all other fluorophores one dataset was fitted using SPCImage and the same settings (bin, threshold, instrumental response function [IRF]) reused by batch-processing for all other datasets of the same fluorophore.

2.3 | Fluorophores and quencher

The fluorophores coumarin 1 (D87759, 99%, Sigma Aldrich, Darmstadt, Germany) and coumarin 6 (546 283, >99%, Sigma Aldrich, Darmstadt, Germany) were chosen to prepare NADH- and FAD-mimicking optical phantoms, because of the spectral similarities to NADH and FAD expected from literature sources [8–11]. To adjust the fluorescence lifetimes of the coumarin phantom solutions to those of NADH and FAD in different molecular states and environments, 4-hydroxy-TEMPO was used as a quencher. The used fluorophores, solvents, quencher, excitation wavelengths, and emission filters, are listed in Table 2. The concentration and number of measurements for the coumarin solutions varied with the experiment carried out and are described in the corresponding section of the main text.

The expected similarity of the spectral characteristics was verified by measurements on coumarin solutions in

TABLE 1 Used standard fluorophore solutions

Fluorophore	Distributor	Article no.	mol L^{-1}	Solvent	λ_{ex} (nm)	Filter	n
Coumarin 6	Sigma Aldrich	546 283	$2 \cdot 10^{-4}$	Ethanol	780	562/40	3
Coumarin 6	Sigma Aldrich	546 283	$2 \cdot 10^{-4}$	Ethanol	880	562/40	3
PPO	Sigma Aldrich	D210404	10^{-3}	Ethanol	780	436/20	2
POPOP	Sigma Aldrich	P3754	Saturated	Ethanol	780	436/20	7
Rose Bengal	Sigma Aldrich	330 000	10^{-3}	Methanol	780	562/40	5
Rose Bengal	Sigma Aldrich	330 000	$0.5 \cdot 10^{-3}$	Water	780	562/40	2
Solvent							
Ethanol (Uvasol)	Merck	1.0098					
Methanol (Uvasol)	Merck	1.06002					
Water (LiChrosolv)	Merck	1.15333					

Note: mol L^{-1}: concentration; λ_{ex}: excitation wavelengths; Filter: detection filters (center wavelength/full width in nm); n: number of fluorescence lifetime measurements per fluorophore.

TABLE 2 Fluorophores, solvents and quencher

Fluorophore	Distributor	Article no.	mol L^{-1}	Solvent	λ_{ex} (nm)	Filter	n	
Coumarin 1	Sigma Aldrich	D87759	*	Ethanol	780, *	436/20	*	◆
Coumarin 6	Sigma Aldrich	546 283	*	Ethanol	780, 880, *	436/20, 562/40	*	◆
NADH	Sigma Aldrich	N8129	5×10^{-3}	TRIS buffer	780, *	436/20	16	◆
FAD	Enzo Life Sciences, Inc.	ALX-480-084-M050	5×10^{-3}	TRIS buffer	780, 880	562/40	3	⋆
FAD	Sigma Aldrich	F6625	*	TRIS buffer	*	-		■
Solvent								
Ethanol (Uvasol)	Merck	1.0098	-	-	-	-	-	◆
TRIS 1 M pH 7.5	Jena Biosciences	BU-125S	1	-	-	-	-	⋆
TRIS 1 M pH 7.5	Invitrogen	15 567–027	1	-	-	-	-	■
Quencher								
4-hydroxy-TEMPO	Sigma Aldrich	176 141	*	-	-	-	-	⋆

Note: mol L^{-1}: concentration; λ_{ex}: excitation wavelengths; Filter: detection filters (center wavelength/full width [in nm]); *n*: number of fluorescence lifetime measurements per fluorophore; *: different values, depending on experiment (see main text); -: not applicable; ■: used in single-photon (absorption and single-photon fluorescence) experiments; ⋆: used in multiphoton (fluorescence intensity and/or lifetime) experiments; ◆: used in multiphoton (fluorescence intensity and/or lifetime) and single-photon (absorption and single-photon fluorescence) experiments.

ethanol (spectroscopy grade) in comparison to freshly prepared solutions of NADH and FAD in TRIS buffer. For this purpose, single-photon absorption spectra were measured with a UV/VIS spectrometer (Lambda 40 P, Perkin Elmer, Rodgau, Germany), single-photon (1P) excitation and emission spectra were measured with a fluorescence spectrometer (Fluoromax II, Horiba, Tokyo, Japan), and two-photon (2P) emission spectra were measured with a multiphoton microscope (Zeiss LSM710 NLO, Carl Zeiss Microscopy GmbH, Jena, Germany).

The measured spectra are shown in Figure 2 for NADH and coumarin 1 and in Figure 3 for FAD and coumarin 6. The wavelengths used for 1P and 2P excitation and the detection filter regimes are indicated in the graphs.

2.4 | Determination of the dependence of coumarin fluorescence lifetimes on fluorophore concentration

For coumarin 6, the fluorescence lifetime is reported to be independent of fluorophore concentration in the range of 10^{-2} to 10^{-6} mol L^{-1} [12]. It was checked whether this behavior can also be confirmed for coumarin 1, for 10^{-2}, 10^{-3}, 10^{-4} and 10^{-5} mol L^{-1} solutions in ethanol at excitation wavelength 780 nm. In the case of coumarin 6, only selected measurements were performed to confirm the information already available from literature [12].

2.5 | Determination of the dependence of coumarin fluorescence lifetimes on quencher concentration

The dependencies of the fluorescence lifetimes of coumarin 1 and coumarin 6 in ethanol on the concentration of the quencher 4-hydroxy-TEMPO were determined by two-photon fluorescence lifetime imaging. Suitable fluorophore concentrations, excitation wavelengths and laser power settings were chosen in each case. The choices made are discussed in the respective sections.

From coumarin 1, a 2×10^{-2} mol L^{-1} solution in ethanol was prepared and further diluted to 2×10^{-4} mol L^{-1}. The 4-hydroxy-TEMPO was prepared into a 0.83 mol L^{-1} solution and seven diluted solutions of different molarities. Nine solutions, named C1.0 to C1.8, with a constant coumarin 1 molarity of 10^{-4} mol L^{-1} and increasing 4-hydroxy-TEMPO molarities between 0 and 0.415 mol L^{-1} were obtained by mixing equal volumes of 2×10^{-2} mol L^{-1} coumarin 1 solution with either pure solvent (C1.0) or one of the eight prepared 4-hydroxy-TEMPO solutions (C1.1-C1.8). The resulting concentrations of the solutions C1.0 to C1.8 are listed in Table 3.

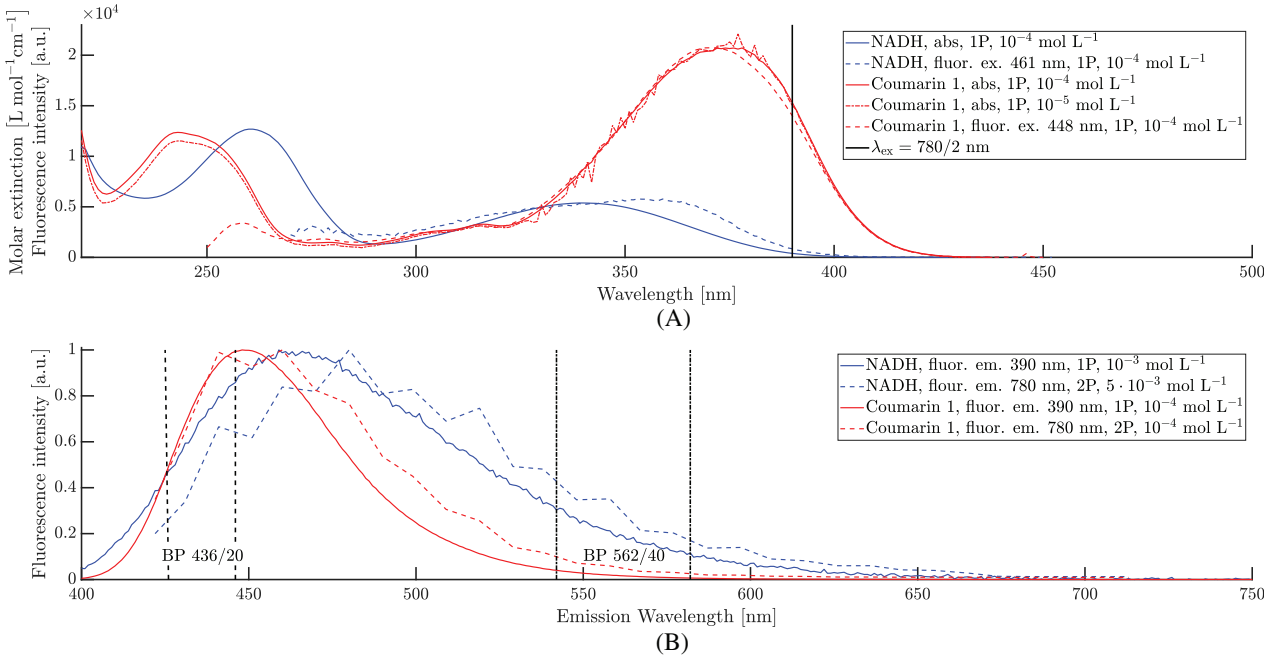

FIGURE 2 Absorption and fluorescence data for NADH and coumarin 1, for explanation of the curves refer to legend; 1P: single-photon data, 2P: two-photon data; A, abs: absorption spectrum; fluor. ex.: fluorescence excitation spectrum; λ_{ex}: half two-photon excitation wavelength; fluorescence excitation spectra scaled to fit absorption spectra; B, fluor. em.: fluorescence emission spectrum; black dashed lines: 436/10 nm BP, black dash-dot lines: 562/40 nm BP; data normalized to maximum

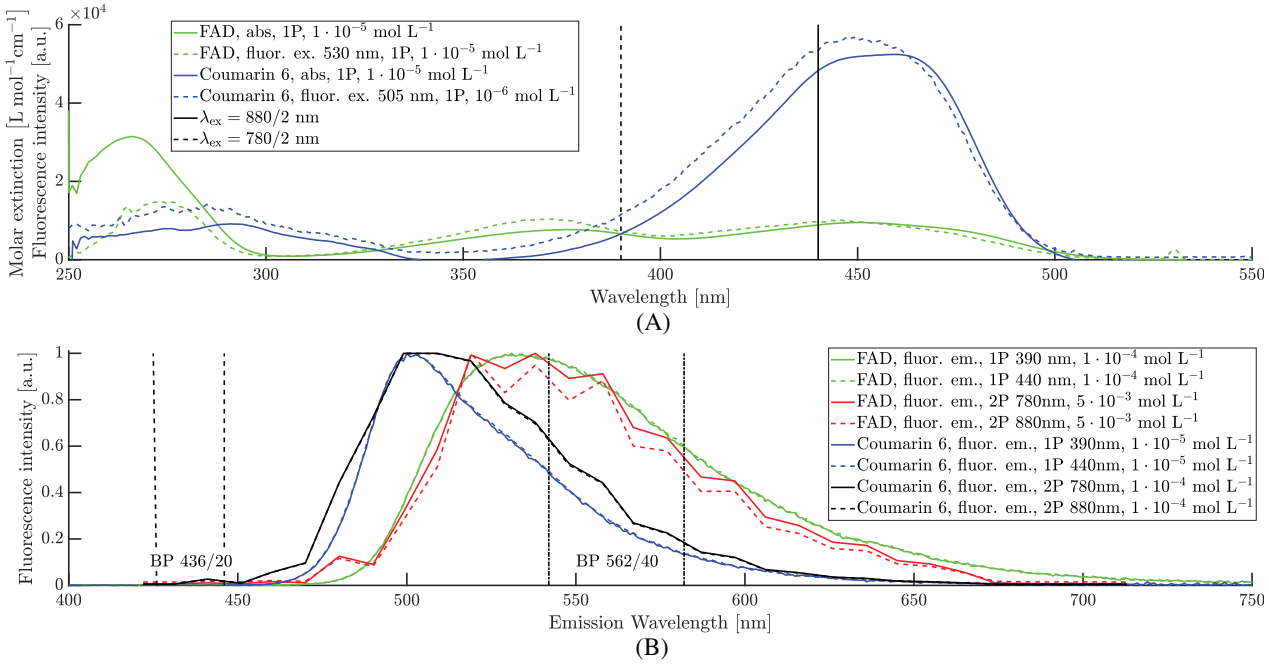

FIGURE 3 Absorption and fluorescence data for FAD and coumarin 6, for explanation of the curves refer to legend; 1P: single-photon data, 2P: two-photon data; A, abs: absorption spectrum; fluor. ex.: fluorescence excitation spectrum; λ_{ex}: half two-photon excitation wavelength; fluorescence excitation spectra scaled to fit absorption spectra; B, fluor. em.: fluorescence emission spectrum; black dashed lines: 436/20 nm BP, black dash-dot lines: 562/40 nm BP; data normalized to maximum

All nine solutions C1.0 to C1.8 were prepared independently three times (further referred to as batch 1, 2 and 3) from scratch on separate days. The fluorescence lifetime of each solution was measured one to three times, in each case with two different relative laser power settings (2% and 3%, referring to 1.1 mW and 2 mW, as measured in the focal plane) at $\lambda_{ex} = 780$ nm.

For coumarin 6, fluorescence lifetime measurements with two-photon excitation at 780 and 880 nm were performed on solutions with coumarin 6 and 4-hydroxy-TEMPO concentrations as shown in Table 4. The relative laser power used for both excitation wavelengths was between 1% and 2% (referring to 0.1 to 0.5 mW in the focal plane for $\lambda_{ex} = 880$ nm and 0.3 to 1.1 mW for $\lambda_{ex} = 780$ nm). Every measurement was performed once, except in the absence of quencher, where three measurements at 780 nm and two measurements at 880 nm were performed.

Fluorescence lifetime data were recorded for 30 s in each case. The resulting data were analyzed using SPCImage 8.0 NG for coumarin 1 and SPCImage 8.1 NG for coumarin 6 with the fit method weighted least square (WLS). From each of the three coumarin 1 batches one of the obtained fluorescence lifetime datasets was analyzed using SPCImage by adjusting bin factor and threshold. The IRF was automatically calculated by SPCImage at the brightest pixel of the time-integrated image. All other fluorescence lifetime datasets of the same coumarin 1 batch were then analyzed using SPCImage's batch processing function, using the same bin factor, threshold and IRF for all datasets of that batch. Datasets of coumarin 6 where analyzed in a similar way, yet with the IRF calculated at the brightest pixel of each individual time-integrated image. A monoexponential decay model turned out to be sufficient in each case.

For the analysis of coumarin 1 fluorescence lifetime images using SPCImage, a binning factor of 1 was used and the decay model option was set to incomplete, to account for residual fluorescence from the previous excitation pulse [13]. The mean value μ and the two values $\mu \pm \sigma$ derived from the lifetime distribution histogram was exported for every dataset. Six fluorescence lifetime results were obtained for each of the solutions C1.0 to C1.8 (three repetitions for each of the two relative laser power settings 2% and 3%) and were imported into Matlab (The MathWorks Inc., Natick, Massachusetts, United States; Version 2020a) for statistical analysis, further fitting operations, and visualization. For each of the nine samples C1.0 to C1.8 with different quencher concentrations Q, the median τ_{B1-3} and the SD σ_{B1-3} derived from the three batches were calculated from the six fluorescence lifetime values. The fluorescence lifetime τ_0 of unquenched coumarin 1 was defined as the mean value of the six fluorescence lifetime values obtained on solution C1.0 in Table 3. Basic solutions as well as the solutions C1.0 to C1.8 were prepared in tubes (Safe-Lock Tubes 2 mL, Eppendorf AG, Hamburg, Germany) and after the initial experiment the remaining volume was kept refrigerated between 2 and 4 °C for later analysis, after being sealed with Parafilm M (Bemis Company, Inc, Oshkosh, United States).

The fluorescence lifetime τ_0 for unquenched coumarin 6 was defined as the mean fluorescence lifetime value of the five fluorescence lifetime values obtained in the absence of quencher and compared to the coumarin 6 fluorescence lifetime values obtained from the systems validation described above. The procedure for the analysis of coumarin 6 fluorescence lifetime images of the samples C6.0 to C6.7 was basically the same as described for coumarin 1, except for the usage of a bin factor of 4 in images with high quencher concentrations. Results were again averaged over different relative laser power settings (in this case ranging between 1% and 2% for both two-photon excitation wavelengths).

To check if the non-transparent quencher (stock solution has dark amber color for the human visual system) has a detectable influence on the fluorescence spectrum, the following procedure was performed for each of the coumarin 1 samples C1.0 to C1.8 and coumarin 6 samples C6.0, C6.3, and C6.7. A fluorescence spectrum was recorded in the same focal plane as the acquired FLIM data, using the LSM 710's spectral imaging unit, an excitation wavelength of 780 nm for coumarin 1 and additionally 880 nm for coumarin 6. It was verified that the spectrum did not contain relevant contributions attributable to the quencher.

Additionally it was checked if the quenched and non-quenched coumarin 1 and coumarin 6 solutions show a monoexponential fluorescence decay behavior. Firstly, by switching to a double-exponential fitting model with a second decay component, observing the residuals, the

TABLE 3 Coumarin 1/4-hydroxy-TEMPO combinations

Identifier	C1.0	C1.1	C1.2	C1.3	C1.4
mol L^{-1} 4-hydroxy-TEMPO	0	2.6×10^{-5}	5.2×10^{-4}	1.0×10^{-2}	2.6×10^{-2}
Identifier	**C1.5**		**C1.6**	**C1.7**	**C1.8**
mol L^{-1} 4-hydroxy-TEMPO	5.2×10^{-2}		0.1	0.21	0.415

Note: Coumarin 1 concentration: 10^{-4} mol L^{-1} for all combinations.

TABLE 4 Coumarin 6/4-hydroxy-TEMPO combinations

Identifier	C6.0	C6.1	C6.2	C6.3
mol L^{-1} 4-hydroxy-TEMPO	0	$1.14 \cdot 10^{-2}$	2.08×10^{-2}	8.30×10^{-2}
mol L^{-1} Coumarin 6	10^{-4} and 7.5×10^{-5}	7.5×10^{-5}	7.5×10^{-5}	10^{-4}
Identifier	**C6.4**	**C6.5**	**C6.6**	**C6.7**
mol L^{-1} 4-hydroxy-TEMPO	0.114	0.208	0.396	0.415
mol L^{-1} Coumarin 6	7.5×10^{-5}	7.5×10^{-5}	7.5×10^{-5}	10^{-4}

goodness of fit χ^2, and the relative contribution of the second component to the fit model [13]. Second, by using the phasor plot of SPCImage and confirming that the phasors are concentrated in one narrow spot on or very close to the semicircle of the phasor plot [13, 14].

2.6 | Fitting functions for coumarin 1 and coumarin 6 fluorescence quenching

The dependencies of the obtained fluorescence lifetime values τ_{B1-3} on quencher concentration were analyzed by fitting different model functions to the observed datapoints, using Matlab's Curve Fitting Toolbox (version 3.5.10, The Mathworks Inc).

The Stern-Volmer equation for dynamic quenching [15–17],

$$\frac{F_0}{F} = \frac{\tau_0}{\tau} = 1 + K_{SV}[Q] \tag{1}$$

Further referred to as SV1, describes the reduction of the fluorescence intensity F and the fluorescence lifetime τ in the presence of a quencher with concentration Q[mol L^{-1}], where τ_0 and F_0 are the corresponding values without quencher and K_{SV} the Stern-Volmer quenching constant. This equation can alternatively be written as a hyperbolic function,

$$\tau = \frac{\tau_0}{1 + K_{SV,H1}[Q]} \tag{2}$$

Further referred to as H1, as far as the fluorescence lifetime τ is concerned. The intensity term $\frac{F_0}{F}$ was disregarded here, since fluorescence intensities were not examined or evaluated quantitatively.

By adding a quadratic term in the denominator on the right-hand side of Equation (2), a refined version of the hyperbolic function H1 can be constructed,

$$\tau = \frac{\tau_0}{1 + K_{SV,H2}[Q] + K_{SV2,H2}[Q]^2} \tag{3}$$

Further referred to as H2.

In case of combined static and dynamic quenching, the quenching of the fluorescence intensity can be described by the following extended version, Equation (4), of the aforementioned Stern-Volmer equation SV1 for dynamic quenching [15]:

$$\frac{F_0}{F} = (1 + K_D[Q])(1 + K_S[Q]) \tag{4}$$

An analogously formulated phenomenological equation for the fluorescence lifetime,

$$\frac{\tau_0}{\tau} = (1 + K_D[Q])(1 + K_S[Q]) \tag{5}$$

Further referred to as SV2, has also been tested to fit the obtained dependence of fluorescence lifetimes on the quencher concentration.

2.7 | Adjustment of phantom fluorescence lifetime to in-vivo NADH and FAD

From the model fitting of the observed $\tau_{B1-3}(Q)$ datasets for coumarin 1 based on Equation (3), the 4-hydroxy-TEMPO concentrations $Q_{0.4}$ and $Q_{2.5}$ were determined that correspond to the fluorescence lifetimes of free and bound NADH, $\tau_1 \approx 0.4$ ns [18, 19] and $\tau_2 \approx 2.5$ [16], respectively. Subsequently, two solutions of 10^{-4} mol L^{-1} coumarin 1 and the two concentrations $Q_{0.4}$ and $Q_{2.5}$ of 4-hydroxy-TEMPO were prepared as described above, and the fluorescence lifetimes were measured at 2% and 3% relative laser power at 780 nm excitation wavelength three times each, using the same conditions as for the determination of τ_{B1-3}. The two solutions were prepared three times from scratch, and measurements were repeated, leading to 18 fluorescence lifetime values per solution. Mean, median, and SD were determined using Matlab, and the values were compared to the two target fluorescence lifetime values.

To mimic the fluorescence lifetimes of bound and free FAD, $\tau_1 \approx 0.1$ ns (106 ps [20], 130 ps [21]) and $\tau_2 \approx 2$ ns (see Table 6), target lifetimes of $\tau_1 = 0.1$ ns and $\tau_2 = 2$ ns were chosen for the coumarin 6 solution. From the model

fitting of the observed $\tau(Q)$ datasets for coumarin 6 based on Equation (3), the 4-hydroxy-TEMPO concentration $Q_{2.0}$ was determined that corresponds to the fluorescence lifetime of free FAD, $\tau_2 \approx 2.0$ ns. For the fluorescence lifetime $\tau_1 = 0.1$ ns of bound FAD, the required quencher concentration was not within the examined range. Nevertheless, by extrapolation based on fit function H2, the hypothetically required quencher concentration $Q_{0.1}$ could be calculated to mimic $\tau_1 = 0.1$ ns of bound FAD. Since it is unknown if a fluorescence lifetime of ≈0.1 ns can be reached by quenching coumarin 6, an alternative substance is proposed for this purpose.

2.8 | Test of coumarin 1 long-time stability

Since long-time stability is highly desirable for optical phantoms, the fluorescence lifetime $\tau_{B2,Rep}$ (repetition measurement) of the nine preserved coumarin 1 solutions C1.0 to C1.8 of batch 2 were measured again after 41 days. Additionally, the preserved basic solutions for coumarin 1 batch 2 (2×10^{-4} mol L^{-1} coumarin 1 solution and the 4-hydroxy-TEMPO solution with molarity 0.83 mol L^{-1} plus seven diluted versions thereof) were still available. By mixing them again at equal volumes, the initial preparation was recreated, yielding fluorescence lifetimes $\tau_{B2,New}$ (measurement after new preparation). All solutions were measured once at 780 nm and for 2% and 3% relative laser power. Fitting with SPCImage was done using the same values for threshold and binning factor as for the initial measurements.

3 | RESULTS

3.1 | Validation of FLIM system

In Table 5, results of fluorescence lifetime measurements on fluorescence lifetime standards proposed in literature are compared with the corresponding literature values. The multiphoton FLIM system used for the present work seems to provide fluorescence lifetimes in good agreement with the ones expected from literature. All fluorophores listed in Table 5 showed monoexponential decay behavior, as expected from literature.

3.2 | NADH and FAD fluorescence lifetimes

The measured fluorescence lifetimes of unbound NADH and FAD solutions in 1 mol L^{-1} TRIS pH 7.5, prepared as specified in Table 2, are shown in Table 6. The obtained fluorescence lifetimes for NADH are in reasonable agreement with literature. For FAD the obtained fluorescence lifetime corresponds to one of the published lifetimes of ≈2000 ps. Reported fluorescence lifetimes of FAD, which could exist protein-bound and unbound, vary in the range 7 to ≈4000 ps [5, 28, 29], depending on stacking and conformation. A fluorescence lifetime of ≈2000 ps for FAD is usually associated with free FAD [5, 15, 21, 30], therefore the same molecule state was assumed here.

Fitting was done monoexponentially also for NADH since no indication of bi- or tri-exponential decay behavior was discernable in the data, and the obtained fluorescence lifetime ≈400 ps was interpreted as indication that the fluorophore was present in its free (unbound) form [19, 30, 31]. FAD was fitted monoexponentially since the presence of a second or third component could not be verified with absolute certainty.

3.3 | Dependency of coumarin 1 and coumarin 6 fluorescence lifetimes on fluorophore concentration

Independence of the fluorescence lifetime on coumarin 1 concentration in ethanol could be confirmed for concentrations 10^{-3}, 10^{-4}, 10^{-5} mol L^{-1}, and a mean value of (2913 ± 52) ps was obtained from a total of 11 measurements. For a coumarin 1 concentration of 10^{-2} mol L^{-1}, which in contrast to coumarin 6 at this concentration [12] dissolved completely, the fluorescence lifetime was ≈2700 ps. The independence of the fluorescence lifetime of coumarin 6 on concentration reported in literature [12] could be confirmed for all tested fluorophore concentrations.

3.4 | Dependency of coumarin 1 and coumarin 6 fluorescence lifetimes on quencher concentration

By means of the quencher 4-hydroxy-TEMPO, the fluorescence lifetime of coumarin 1 could be varied in a range between $\tau_0 = (2927.8 \pm 16.9)$ ps in the absence of quencher and $\tau = (196.8 \pm 12.4)$ ps at a quencher concentration of 0.415 mol L^{-1}. Likewise, the fluorescence lifetime of coumarin 6 could be varied between $\tau_0 = (2478.8 \pm 36.1)$ ps and $\tau = 200$ ps. In all cases, the monoexponential decay behavior was maintained. The determined value τ_0 for coumarin 6 in these quenching experiments lies within the SD of the coumarin 6 measurements performed for the validation of the FLIM system (Table 5).

TABLE 5 Results of fluorescence lifetime measurements of selected standard fluorophores and comparison with literature

Fluorophore	*n*	τ (ps)	$\tau-\sigma$ (ps)	$\tau+\sigma$ (ps)	Lit. τ (ps)
PPO	2	1617.51	1595.43	1639.9	1600 [15]
		1612.99	1582.1	1643.5	
		Mean τ (ps)	**STD τ (ps)**		
Coumarin 6	6	2488.93	41.92		2390 [12]
POPOP	7	1273.49	16.75		1380 [15], 1430 [22], 1400 [23]
Rose Bengal (Methanol)	5	555.22	4.83		519 [15], 516 [24], 540 [25]
Rose Bengal (Water)	4	87.1	6.6		140 [26], 120 [25], 78 [27]

TABLE 6 Results of fluorescence lifetime measurements on NADH and FAD solutions and comparison with literature

Fluorophore	*n*	Mean τ (ps)	STD τ (ps)	Lit. τ (ps)
NADH	16	416.9	26.3	≈400 [18, 19], 470 [31], 500 ps [22]
FAD	3	1945.4	34.7	≈2000 [20], τ_3 = 2090 (solution) [5], 2460 [22], 2300 ± 700 [21], τ_2 = 2820 (solution) [28], 2470 [32]

Note: n: number of fluorescence lifetime measurements per fluorophore.

In Figure 4 the fit functions H1 and H2 defined in Equations (2) and (3), respectively, are shown together with the measured fluorescence lifetimes of coumarin 1 (τ_{B1-3}, the average over sample batches 1-3) and coumarin 6.

Fitting with fit function H1 yields $K_{SV,H1}$ = 22.73 (20.89,24.57) L mol^{-1} with R^2 = 0.998 for coumarin 1 and $K_{SV,H1}$ = 20.00 (18.62,21.37) L mol^{-1} with R^2 = 0.998 for coumarin 6. Here the 95% confidence intervals are added in brackets.

Despite the high R^2 value in both cases, the fits in Figure 4 show good agreement with the measured data only for lower quencher concentrations up to ≈0.1 mol L^{-1}, while increasing deviations of the H1 fit curves from the datapoints are observed for higher quencher concentrations, both in the case of coumarin 1 and coumarin 6. Since it was strongly desired that the fit model is valid also for short fluorescence lifetimes of 0.1 ns to 0.4 ns, which turned out to require higher quencher concentrations >0.1 mol L^{-1}, this problem cannot be neglected. It was therefore addressed by modification of the fitting model, leading to the fit function H2 defined in Eq. (3). The respective curve fits yielded the model parameters $K_{SV,H2}$ = 20.36 L mol^{-1} and $K_{SV2,H2}$ = 32.43 L^2 mol^{-2} and R^2 = 0.999. In contrast to H1, the H2 fit curves are in good agreement with the coumarin 1 and coumarin 6 fluorescence lifetime datapoints within the entire examined range of quencher concentrations, including quencher concentrations >0.1 mol L^{-1} (see Figure 4).

Figure 5 shows the Stern-Volmer plots, $\tau_0\,\tau^{-1}$ vs quencher concentration Q, for the measured fluorescence lifetimes of coumarin 1 and coumarin 6, in each case together with the fit functions SV1 and SV2 defined in Equations (1) and (5), respectively. The fit of the linear Stern-Volmer relationship in Equation (1) for solely dynamic quenching yields K_{SV} = 31.65 (29.01,34.29) L mol^{-1} and R^2 = 0.986 for coumarin 1, as well as K_{SV} = 25.26 (24.29,26.24) L mol^{-1} and R^2 = 0.992 for coumarin 6. In both cases, the fit quality can be considered insufficient, since a linear fit does not adequately describe

the measured fluorescence lifetime datasets (see SV1 curves in Figure 5). The fits to the quadratic function SV2 defined in Equation (5) yield KS = 19.18 (18.6,19.76) L mol^{-1}, KD = 1.60 (1.479,1.706) L mol^{-1} and $R^2 = 1.0$ for coumarin 1, and KS = 16.61 (13.74,19.48) L mol^{-1}, KD = 1.189 (0.6257,1.752) L mol^{-1} and $R^2 = 0.998$ for coumarin 6. In both cases, the measured datapoints are adequately described by the fit function SV2 in the entire range of examined quencher concentrations, as in the case of Figure 4 and the fit function H2 defined in Equation (3).

Two-photon fluorescence emission spectra of coumarin 1 and coumarin 6 with concentrations listed in Tables 3 and 4, respectively, showed a decrease in fluorescence intensity with increasing quencher concentration as to be expected from the Stern-Volmer relationship in Equation (1). For both substances no shift in fluorescence wavelength with quencher concentration and, in the case of coumarin 6, excitation wavelength could be observed.

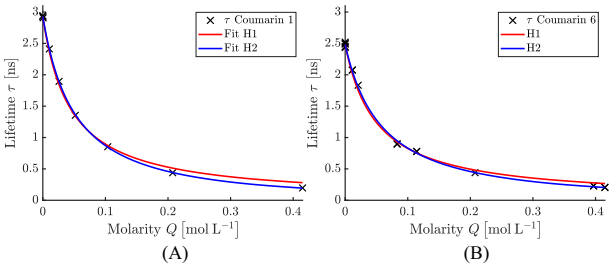

FIGURE 4 Measured fluorescence lifetimes together with fit curves according to functions H1 and H2 defined in Equations (2) and (3) respectively, of A, coumarin 1 (with $\tau = \tau_{B1-3}$, the average over sample batches 1-3) and B, coumarin 6

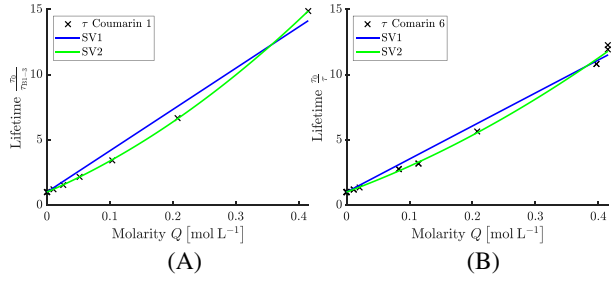

FIGURE 5 Stern–Volmer plots $\frac{\tau_0}{\tau}$ vs Q, in each case together with fit functions SV1 and SV2 defined in Equations (1) and (5), respectively, for A, coumarin 1 (with $\tau = \tau_{B1-3}$, the average over sample batches 1-3) and B, coumarin 6

3.5 | NADH and FAD fluorescence lifetime synthesis

For the synthesis of phantom solutions with fluorescence lifetimes corresponding to those of free and bound NADH, $\tau_1 \approx 0.4$ ns and $\tau_2 \approx 2.5$ ns, respectively, the required 4-hydroxy-TEMPO concentrations were determined as $Q_{0.4} = 0.234$ mol L^{-1} and $Q_{2.5} = 8.55 \times 10^{-3}$ mol L^{-1}, based on the fit function H2 defined in Equation (3).

From the 18 measurements per target fluorescence lifetime, the mean, median and SD were calculated using Matlab as shown in Table 7. In the case of both NADH variants, the obtained fluorescence lifetime is shorter than the target value, but still within the range of the SD.

For the synthesis of phantom solutions with fluorescence lifetimes corresponding to those of bound and free FAD, $\tau_1 \approx 0.1$ ns and $\tau_2 \approx 2.0$ ns, respectively, the required 4-hydroxy-TEMPO concentrations were determined as $Q_{2.0} = 1.3 \times 10^{-3}$ mol L^{-1} and, outside of the examined Q range, $Q_{0.1} = 0.713$ mol L^{-1}, again based on the fit function H2.

3.6 | Test of long-time stability of coumarin 1 solutions

The fluorescence lifetime values τ_{B1-3} obtained from the initial measurements on sample batches 1 to 3 where compared with the results of measurements performed 41 days later. The values $\tau_{B2,Rep}$ were obtained in repeated measurements on the archived samples of batch 2 and the values $\tau_{B2,New}$ were obtained on samples newly mixed from the archived basic solutions of batch 2.

The fluorescence lifetimes $\tau_{B2,Rep}$ and $\tau_{B2,New}$ obtained after 41 days are consistent with those obtained in the initial measurements. The maximum deviation from the initial results τ_{B1-3} was found to be $\Delta\tau = 36.8$ ps. This indicates that a solution prepared and stored in

TABLE 7 4-hydroxy-TEMPO quencher concentrations for the synthesis of coumarin 1 based phantoms with fluorescence lifetimes corresponding to those of free and bound NADH

Target fluorophore	Target τ (ns)	Q (mol L^{-1})	τ Mean (ns)	τ Median (ns)	τ STD (ns)
NADH free	0.4	0.234	0.389	0.389	0.017
NADH bound	2.5	8.55×10^{-3}	2.476	2.477	0.058

Note: Q: 4-hydroxy-TEMPO molarity.

the described way is at least stable within the time frame of 1 month. This would be consistent with the reported finding that coumarin 6 in ethanol is stable as a fluorescence lifetime standard for months [14].

4 | DISCUSSION

4.1 | General data processing

For the analysis of FLIM data, one can and has to choose between a vast number of adjustable fit options beforehand. The SPCImage software provides three different fitting methods (one of which may alternatively be implemented on GPU or CPU), 11 different binning factors (0 and 10), usually three different types of fitting function (single, double, triple exponential), and two settings for the decay model (complete and incomplete), which already makes up for at least $3 \times 11 \times 3 \times 2 = 198$ different configurations of the fitting process. Furthermore, the intensity threshold level for pixels to be considered in the fit can be freely adjusted, one can select between different methods for defining the IRF, and the pixel (ie, one of 128×128 pixels) based on which the IRF shall be defined can be freely chosen or will vary depending on the recorded FLIM data. Many of the choices available in SPCImage will result in a successful fit. For each and any of them it can be discussed extensively, whether the choice made is appropriate and the fit result might or might not be valid. Since such discussion will not be expedient, the FLIM images were analyzed by calculating the IRF at the brightest pixel and with the threshold set to auto.

The impact of different settings on the mean fluorescence lifetime of the same dataset was examined for a few samples, by changing the pixel for the IRF calculation, the bin factor and the threshold. The impact of different fitting algorithms has also been discussed literature [33].

Based on these thoughts and investigations, we strongly recommend to always include information about instrumentation and fitting procedures/parameters in publications to aid the generation and dissemination of valuable and reproducible fluorescence lifetime data.

4.2 | Suitability of coumarins with 4-hydroxy-TEMPO in ethanol as phantoms for NADH and FAD

Two-photon excitation at 780 nm is suitable for NADH and coumarin 1. The two-photon absorption cross section, expressed in units of Göppert-Mayer ($1\ \mathrm{GM} = 10^{-50}\ \mathrm{cm}^{-4}\ \mathrm{s\ photon}^{-1}\ \mathrm{molecule}^{-1}$), is relatively small in case of NADH, with reported values for 780 nm of ≈0.003 GM [34] and ≈0.02 GM [35]. In comparison, for coumarin 1 in a concentration of 10^{-5} mol L^{-1} in ethanol excited with a Ti:Sa laser, much higher two-photon absorption cross sections of 75.6 GM at 774.5 nm and 28.5 GM at 797.0 nm have been reported [10]. Correspondingly, rather low coumarin 1 concentrations had to be chosen to obtain fluorescence intensities similar to those of NADH typically observed in biological samples.

Above that, the following can be stated: The emission spectrum of coumarin 1 is narrower than that of NADH, as can be seen in Figure 2, but several important features are retained. The shapes of the emission spectra in the NADH bandpass filter range (436/20 nm) are similar, although the one of courmarin 1 is somewhat broader, and the long-wavelength tails of both emission spectra extend into the FAD bandpass filter range (562/40 nm), although at a considerably lower relative level in the case of coumarin 1. The fluorescence lifetime of the coumarin 1 phantom can be matched to that of NADH (ranging from 0.4 to 2.5 ns for free and bound NADH) by the quencher 4-hydroxy-TEMPO.

With this, it can be concluded that coumarin 1 fulfills all essential conditions to serve as a two-photon FLIM phantom for NADH: Its fluorescence can be excitated at 780 nm and detected with a 436/20 nm bandpass filter, with fluorescence lifetimes matchable to those of NADH. The fluorescence of both fluorophores leaks into the employed FAD bandpass filter range.

For coumarin 6 the following can be stated: Two-photon excitation at 780 and 880 nm is possible for both FAD and coumarin 6. For coumarin 6, no information about two-photon absorption cross sections could be found in literature.

The emission spectrum of coumarin 6 largely resembles that of FAD, with similar widths and only a slight shift toward shorter wavelength in the case of coumarin 1, as can be seen in Figure 3. Both fluorophores show emission in the FAD bandpass filter range (562/40 nm), but not in the NADH bandpass filter range (436/20 nm). The fluorescence lifetime of coumarin 6 can be varied in the range of 0.2 to 2.5 ns, therefore the FAD phantom can at least be matched to the fluorescence lifetime of unbound FAD of ≈2.0 ns. The quencher concentration necessary to reach the fluorescence lifetime of bound FAD of ≈0.1 ns has to be tested. Alternatively, Rose Bengal (330 000, 95%, Sigma Aldrich) dissolved in water could be used to reach the short fluorescence lifetime of bound FAD. The fluorescence spectrum of coumarin 6 overlaps well with the range of the used bandpass for FAD detection and two-photon fluorescence excitation was well feasible with excitation wavelengths 780 and 880 nm. The obtained fluorescence lifetime is ≈0.1 ns, which is consistent with literature values (0.12 ns [25]).

Thus, it can be concluded that coumarin 6 also fulfills all essential conditions to serve as a two-photon FLIM phantom for FAD: Its fluorescence can be excited at 780 and 880 nm and detected with a 562/40 nm bandpass filter, with fluorescence lifetimes matchable to those of unbound FAD and, at least approximately, also those of bound FAD. Furthermore, the fluorescence of both fluorophores does not leak into the employed NADH bandpass filter range.

Therefore both coumarin phantoms match the basic requirement for a phantom to have similar properties as the target fluorophores, but not necessarily identical ones [4]. Any other phantom features are, at this stage of phantom development, of negligible importance, but one has to be aware of their existence.

4.3 | Phantom limitations and development options

A major limitation of the proposed pair of liquid coumarin phantoms is that they can only be prepared to exhibit one single fluorescence lifetime. For example, a mixture of coexisting bound and free NADH (or FAD) cannot be mimicked with the proposed coumarin 1 (or coumarin 6) solutions with added 4-hydroxy-TEMPO, because it is not possible to have two different concentrations of the same quencher in one homogeneous solution with free convection. One alternative approach would be to use two different spectrally suitable fluorophores, provided that: (a) the two fluorophores are differently (but, coincidentally, exactly to the desired extent) affected by the same quencher or (b) a second spectrally suitable fluorophore/quencher system can be established in the same solution, such that the two fluorophore/quencher systems can be tuned more or less independently from each other. The fluorescence lifetime characteristics of mixtures of different fluorophores have been reported in literature, for example, for lucifer yellow/coumarin 6 and rhodamine B/coumarin 6 [12], but in both cases quenching was not investigated. For both mixtures, slight shifts in the fluorescence lifetimes of the components have been reported [12]. First experiments were carried out with a mixture of fluorescein in a 0.05 mol L^{-1} sulfuric acid solution of pH 3.5 and quinine sulfate quenched by sodium chloride (NaCl). The quenching of quinine sulfate worked, but the fluorescence lifetime of the fluorescein solution was found to increase by the addition of quinine sulfate and/or NaCl.

Finding the ideal combination between two fluorophores and two quenchers will require further research, to identify two fluorophores for which the same solvent can be used and two different quenchers are available who do not detrimentally affect each other or the other fluorophore/quencher system. In principle a simultaneous preparation of four different fluorescence lifetimes in the same solution would be desirable, to mimic coexisting bound and free variants of both NADH and FAD.

4.4 | Related intrinsic fluorophores

Inside living tissue there are further intrinsic fluorophores that coexist with NADH and FAD [36]. One fluorophore out of the flavin group is of particular interest: flavin mononucleotide (FMN). It has a similar fluorescence spectrum as FAD [37, 38] and will therefore, if present, unavoidably be detected by a bandpass filter tuned for FAD detection, so that a separation from FAD via emission wavelength is virtually impossible. Also, FMN is known by the authors to be similarly excitable as FAD. However, largely different two-photon excitation cross sections at 800 nm have been reported in literature: 2.1 GM for FAD and 1.6 GM for FMN in one source [37], as well as ≈0.034 GM for FAD [34] and ≈0.17 GM for FMN [39] in two other sources (data in both cases extracted using a graph digitizer [40]).

The potential contribution of FMN to measurements in cell cultures and in vivo is usually not taken into account so far. Apparently, a distinction from FAD is almost impossible based on spectral characteristics of the two molecules, but might be possible based on fluorescence lifetimes [41]. As a potential phantom for FMN, lucifer yellow could be suitable, with a fluorescence lifetime in water of $\tau \approx 5.2$ and $\tau \approx 10$ ns in ethanol [12]. If a suitable quencher can be identified, lucifer yellow could potentially act as phantom for FMN.

5 | CONCLUSION

In conclusion a reproducible and stable standard phantom for two-photon FLIM can be established according to the mentioned recipes, mimicking FAD and NADH in their bound and unbound states. By means of these phantoms, measurements of different two-photon FLIM systems can be made more comparable since the inherent unstable characteristics of NADH and FAD are circumvented. Further investigations would be necessary to create a structured standard with sufficiently small features, which could then be useful to improve the localization of two-photon FLIM signals in samples.

ACKNOWLEDGMENTS

We express our thanks to the Core Facility Confocal and Multiphoton Microscopy at University Ulm and Kirsten Rees for help, assistance and advice, as well as Becker &

Hickl GmbH, Berlin, for advice regarding the FLIM system. This investigation was financially supported by the German Ministry of Education and Research (BMBF), project OMOXI, Grant 13N14507.

CONFLICT OF INTEREST

The authors declare no conflicts of interest.

DATA AVAILABILITY STATEMENT

Research data are not shared.

ORCID

Christian Freymüller https://orcid.org/0000-0002-3014-297X

REFERENCES

[1] K. König, *J. Biophotonics* **2008**, *1*(1), 13.
[2] L. M. G. Huizen, T. Radonic, F. Mourik, D. Seinstra, C. Dickhoff, J. M. A. Daniels, I. Bahce, J. T. Annema, M. L. Groot, *Transl. Biophotonics* **2020**, *2*(4), e202000009.
[3] A. B. E. Attia, R. Bi, K. Dev, D. Yao, M. Olivo, *Transl. Biophotonics* **2020**, *2*(4), e202000010.
[4] B. W. Pogue, M. S. Patterson, *J. Biomed. Opt.* **2006**, *11*(4), 041102.
[5] M. Islam, M. Honma, T. Nakabayashi, M. Kinjo, N. Ohta, *Int. J. Mol. Sci.* **2013**, *14*(1), 1952.
[6] S. Kalinina, J. Breymayer, P. Schäfer, E. Calzia, V. Shcheslavskiy, W. Becker, A. Rück, *J. Biophotonics* **2016**, *9*(8), 800.
[7] A. Rück, C. Hauser, S. Mosch, *J. Biomed. Opt.* **2014**, *19*(9), 096005.
[8] U. Brackmann, *Lamdachrome Laser-Dyes*, 3rd ed. Lambda Physik AG, Göttingen, Germany **2000**. http://www.chem.ucla.edu/~craigim/pdfmanuals/catalogs/Lamdachrome-laser-dyes.pdf
[9] M. Taniguchi, J. S. Lindsey, *Photochem. Photobiol.* **2018**, *94*(2), 290.
[10] A. Fischer, C. Cremer, E. H. K. Stelzer, *Appl. Opt.* **1995**, *34*(12), 1989.
[11] Spectra at UA - University of Arizona, https://www.spectra.arizona.edu/ Accessed March, 2020
[12] A. S. Kristoffersen, S. R. Erga, B. Hamre, Ø. Frette, *J. Fluoresc.* **2014**, *24*(4), 1015.
[13] W. Becker, *The bh TCSPC Handbook*, 8th ed. Becker&Hickl, Berlin, Germany **2019**.
[14] Y. Sun, R. N. Day, A. Periasamy, *Nat. Protoc.* **2011**, *6*(9), 1324.
[15] J. R. Lakowicz, *Principles of Fluorescence Spectroscopy*, 3rd ed., Springer, New York **2006**.
[16] S. Kalinina, J. Breymayer, K. Reeß, L. Lilge, A. Mandel, A. Rück, *J. Biophotonics* **2018**, *11*(10), e201800085.
[17] M. H. Gehlen, *J. Photochem. Photobiol. C Photchem. Rev.* **2020**, *42*, 100338.
[18] S. Kalinina, D. Bisinger, J. Breymayer, A. Rück, in *Multiphoton Microscopy in the Biomedical Sciences XV* (Eds: A. Periasamy, P. T. C. So, K. König), International Society for Optics and Photonics, SPIE, Wellington **2015**, p. 39.
[19] J. R. Lakowicz, H. Szmacinski, K. Nowaczyk, M. L. Johnson, *Proc. Natl. Acad. Sci. USA* **1992**, *89*(4), 1271.
[20] M. C. Skala, K. M. Riching, A. Gendron-Fitzpatrick, J. Eickhoff, K. W. Eliceiri, J. G. White, N. Ramanujam, *Proc. Natl. Acad. Sci. USA* **2007**, *104*(49), 19494.
[21] N. Nakashima, K. Yoshihara, F. Tanaka, K. Yagi, *J. Biol. Chem.* **1980**, *255*(11), 5261.
[22] T. Hinsdale, C. Olsovsky, J. J. Rico-Jimenez, K. C. Maitland, J. A. Jo, B. H. Malik, *Biomed. Opt. Express* **2017**, *8*(3), 1455.
[23] P. Thomas, P. Pande, F. Clubb, J. Adame, J. A. Jo, *Photochem. Photobiol.* **2010**, *86*(3), 727.
[24] R. Luchowski, M. Szabelski, P. Sarkar, E. Apicella, K. Midde, S. Raut, J. Borejdo, Z. Gryczynski, I. Gryczynski, *Appl. Spectrosc.* **2010**, *64*(8), 918.
[25] Y. Sun, A. Periasamy, in *Advanced Fluorescence Microscopy*. Methods in Molecular Biology, Vol. 1251 (Ed: P. J. Verveer), Springer New York, New York, NY **2015**, p. 83.
[26] S.-C. Liao, Y. Sun, C. Ulas, *FLIM Analysis Using the Phasor Plots*, Vol. 61822, ISS, Inc, Champaign, IL **2014**.
[27] H. Stiel, K. Teuchner, A. Paul, D. Leupold, I. E. Kochevar, *J. Photochem. Photobiol., B* **1996**, *33*(3), 245.
[28] A. J. W. G. Visser, *Photochem. Photobiol.* **1984**, *40*(6), 703.
[29] R. Esposito, I. Delfino, M. Portaccio, C. Iannuzzi, M. Lepore, *Eur. Biophys. J.* **2019**, *48*(4), 395.
[30] R. Datta, T. M. Heaster, J. T. Sharick, A. A. Gillette, M. C. Skala, *J. Biomed. Opt.* **2020**, *25*(07), 1.
[31] M. A. Yaseen, J. Sutin, W. Wu, F. Buyin, H. Uhlirova, A. Devor, D. A. Boas, S. Sakadžić, *Biomed. Opt. Express* **2017**, *8*(5), 2368.
[32] D. Chorvat, A. Chorvatova, *Eur. Biophys. J.* **2006**, *36*(1), 73.
[33] K. Santra, J. Zhan, X. Song, E. A. Smith, N. Vaswani, J. W. Petrich, *J. Phys. Chem. B* **2016**, *120*(9), 2484.
[34] S. Huang, A. A. Heikal, W. W. Webb, *Biophys. J.* **2002**, *82*(5), 2811.
[35] Z. Lab, E. Nancy, C. Peter. Meining School of Biomedical Engineering, Cornell University, Ithaca, USA, Two-photon action cross sections, Online, 2020, https://zipfellab.bme.cornell.edu/cross_sections.html Accessed March, 2020
[36] W. R. Zipfel, R. M. Williams, R. Christie, A. Y. Nikitin, B. T. Hyman, W. W. Webb, *Proc. Natl. Acad. Sci. USA* **2003**, *100*(12), 7075.
[37] J. P. Villabona-Monsalve, O. Varnavski, B. A. Palfey, T. Goodson, *J. Am. Chem. Soc.* **2018**, *140*(44), 14562.
[38] A. Mukherjee, J. Walker, K. B. Weyant, C. M. Schroeder, *PLoS One* **2013**, *8*(5), e64753.
[39] C. Xu, W. Zipfel, J. B. Shear, R. M. Williams, W. W. Webb, *Proc. Natl. Acad. Sci. USA* **1996**, *93*(20), 10763.
[40] A. Rohatgi, Webplotdigitizer: Version 4.3, **2020**. https://automeris.io/WebPlotDigitizer/index.htm Accessed November 30, 2020
[41] A. C. Rück, P. Schäfer, B. von Einem, S. Kalinina, in *Multiphoton Microscopy in the Biomedical Sciences XX* (Eds: A. Periasamy, P. T. So, K. König), International Society for Optics and Photonics, Wellington **2020**, p. 6.

How to cite this article: Freymüller C, Kalinina S, Rück A, Sroka R, Rühm A. Quenched coumarin derivatives as fluorescence lifetime phantoms for NADH and FAD. *J. Biophotonics*. 2021;e202100024. https://doi.org/10.1002/jbio.202100024

5.3 Development of a microstructured tissue phantom with adaptable optical properties for use with microscopes and fluorescence lifetime imaging systems

C. Freymüller, S. Ströbl, M. Aumiller, M. Eisel, R. Sroka und A. Rühm, "Development of a microstructured tissue phantom with adaptable optical properties for use with microscopes and fluorescence lifetime imaging systems", *Lasers in Surgery and Medicine*, 1–17, 2022, Publisher: John Wiley & Sons, Ltd. DOI: 10.1002/lsm.23556, JIF_{2021}: 4.025.

Kurzfassung: Das Manuskript beschreibt das Design, die Entwicklung und die Charakterisierung eines künstlichen Gewebephantoms für mikroskopische und mikroendoskopische, bildgebende Systeme. Ziel der Entwicklung ist ein künstliches Gewebephantom mit dessen Hilfe die mögliche Bildgebungstiefe (Position der Fokalebene unter der Phantombeziehungsweise im klinischen Einsatz Gewebeoberfläche) und die erreichbare x, y, und z-Auflösung ermittelt werden kann. Das Phantom soll ebenfalls mit unterschiedlichen Systemen, wie Forschungsmikroskopen und Endoskopen, verwendet werden können, um einen Vergleich von unterschiedlichen Systemen am selben Phantom zu ermöglichen.
Hierzu wurde eine regelmäßige, treppenförmige, Struktur entworfen und in Standard Mikroskopieobjektträger ($76\,mm \times 26 \times 1mm$; n=10) mittels Laser-Mikrostrukturierung eingeschrieben. Die Treppenstruktur erlaubt die Bestimmung der Position der Fokalebene eines Mikroskops oder Endoskops relativ zur Oberfläche des Phantoms ohne die Notwendigkeit eines z-Triebes.
Die entstandenen Glasstrukturen wurden mit einem Messmikroskop hinsichtlich ihrer maximalen Tiefe, Stufenhöhe, Oberflächeneingenschaften und Stufenlänge charakterisiert. Die Strukturen wurden mit an die Anregungs- und Fluoreszenz-Eingenschaften von NADH und FAD angepassten, Mitochondrien simulierenden, Polystyrene Microspheres von $1\,\mu m$ Durchmesser beschichtet. Um die wellenlängenabhängigen Streueigenschaften von Gewebe des oberen Atemwegstraktes zu simulieren, wurde der reduzierte Streukoeffizient μ_s' der humanen Kieferhöhlenschleimhaut für die Wellenlängen $780\,nm$ und $880\,nm$ aus Literaturquellen ermittelt. Die Simulation von Gewebe wurde über eine gewebesimulierende Deckschicht aus einem Hydrogel (Poloxamer/Wasser Lösung) und einer Suspension von nicht fluoreszierenden Polystyrene Microspheres als Streuzentren realisiert. Die Zusammensetzung der Streuschicht wurde mit einem Matlab Optimierungscode, welcher eine publizierte Implementierung eines Codes zur Berechnung von Mie-Streuung nutzt, für beide Wellenlängen ermittelt. Die resultierenden Hydrogel/Polystyrene Microspheres Suspensionen wurden mit einem existierenden Aufbau zur Vermessung von optischen Eingenschaften charakterisiert und die Messergebnisse mit den Designparametern verglichen. Die strukturierten Objektträger wurden mit den NADH und FAD simulierenden fluoreszierenden Polystyrene Microspheres beschichtet, die Vertiefung (tiefste Stelle ca. $250\,\mu m$) mit der Streususpension gefüllt und die Konstruktion mit einem Deckglas versiegelt.
Die Charakterisierung der Phantome erfolgte mit einem Mulitiphotonen-FLIM-Mikroskop bezüglich der Unterscheidbarkeit der Strukturen und erreichbarer Eindringtiefe. Weiterhin wurde das Alterungsverhalten (Verklumpungen der nicht fluoreszierenden Microspheres in der Streuschicht, Ablösen der Beschichtung mit fluoreszierenden Microspheres) der Streuschicht und der Beschichtung mit dem Multiphotonen-FLIM-Mikroskop und einem

Konfokalmikroskop untersucht. Mit dem im Rahmen des Projektes OMOXI von den Projektpartnern entwickelten Endoskop und dem modifizierten FLIM-Messsystem MPTflex, wurden Aufnahmen der Phantomkonstruktionen erstellt. Die entwickelten Phantome können zum Beispiel zur Funktionskontrolle und zum Vergleich verschiedener Messsysteme hinsichtlich der mit der jeweils verfügbaren oder physiologisch verträglichen Anregungslaserleistung erreichbaren Bildgebungstiefe und Ermittlung von Verzeichnungen oder Fehlern im optischen System eingesetzt werden. Durch einen Gegenüberstellung der mit dem MPTflex und dem adaptierten Endoskop entstandenen Bilder mit den Aufnahmen der zuvor genannten Mikroskope wurde beispielhaft der Vergleich unterschiedlicher Systeme demonstriert.

Der Anteil von Christian Freymüller an der Arbeit beinhaltet die Anforderungsanalyse und das Design der strukturierten Glasoberflächen sowie die Charakterisierung (die Herstellung erfolgte in Zusammenarbeit mit Stephan Ströbl), die Literaturrecherche, Entwicklung, Berechnung und Herstellung der fluoreszierenden Polystyrene Microsphere-Beschichtung und der Streususpension (die Vermessung der Streususpension erfolgte in Zusammenarbeit mit Maximilan Aumiller und Maximilian Eisel).
Weiterhin oblag Herrn Freymüller das Experimentdesign zur Charakterisierung der zusammengesetzten Phantome, die Vermessungen sowohl mit dem Mulitiphotonen-FLIM-Mikroskop als auch dem Konfokalmikroskop (Endoskopaufnahmen durch Adrian Rühm, Steuerung der Elektronik remote durch Christian Freymüller), sowie die Auswertung und Interpretation der Mikroskopaufnahmen. Das Manuskript wurde gemeinschaftlich mit den Koautoren erstellt.

Accepted: 24 April 2022

DOI: 10.1002/lsm.23556

BASIC SCIENCE

Development of a microstructured tissue phantom with adaptable optical properties for use with microscopes and fluorescence lifetime imaging systems

Christian Freymüller M.Sc.[1,2] | **Stephan Ströbl Dr. rer. biol. hum.**[1,2,3] | **Maximilian Aumiller M.Sc.**[1,2] | **Maximilian Eisel Dr. rer. biol. hum.**[1,2] | **Ronald Sroka Prof. Dr. rer. biol. hum.**[1,2] | **Adrian Rühm Dr. rer. nat.**[1,2]

[1]Laser-Forschungslabor, LIFE Center, Department of Urology, University Hospital, LMU Munich, Munich, Germany

[2]Department of Urology, University Hospital, LMU Munich, Munich, Germany

[3]Research Center for Microtechnology, FH Vorarlberg, Dornbirn, Vorarlberg, Austria

Correspondence

Christian Freymüller, Laser-Forschungslabor, LIFE Center, Department of Urology, University Hospital, LMU Munich, Munich, Germany.
Email: Christian.Freymueller@med.uni-muenchen.de

Funding information

Bundesministerium für Bildung und Forschung, Grant/Award Number: 13N14507; Österreichische Forschungsförderungsgesellschaft, Grant/Award Number: 855657; Deutsche Forschungsgemeinschaft, Grant/Award Number: (RTG) GRK2274 Project number 299102935

Abstract

Objectives: For the development and validation of diagnostic procedures based on microscopic methods, knowledge about the imaging depth and achievable resolution in tissue is crucial. This poses the challenge to develop a microscopic artificial phantom focused on the microscopic instead of the macroscopic optical tissue characteristics.

Methods: As existing artificial tissue phantoms designed for image forming systems are primarily targeted at wide field applications, they are unsuited for reaching the formulated objective. Therefore, a microscopy- and microendoscopy-suited artificial tissue phantom was developed and characterized. It is based on a microstructured glass surface coated with fluorescent beads at known depths covered by a scattering agent with modifiable optical properties. The phantom was examined with different kinds of microscopy systems in order to characterize its quality and stability and to demonstrate its usefulness for instrument comparison, for example, regarding structural as well as fluorescence lifetime analysis.

Results: The analysis of the manufactured microstructured glass surfaces showed high regularity in their physical dimensions in accordance with the specifications. Measurements of the optical parameters of the scattering medium were consistent with simulations. The fluorescent beads coating proved to be stable for a respectable period of time (about a week). The developed artificial tissue phantom was successfully used to detect differences in image quality between a research microscope and an endoscopy based system. Plausible causes for the observed differences could be derived based on the well known microstructure of the phantom.

Conclusions: The artificial tissue phantom is well suited for the intended use with microscopic and microendoscopic systems. Due to its configurable design, it can be adapted to a wide range of applications. It is especially targeted at the characterization and calibration of clinical imaging systems that often lack extensive positioning capabilities such as an intrinsic *z*-stage.

KEYWORDS

artificial tissue phantom, endomicroscopy, endoscopy, fluorescence lifetime imaging, microscopy, two-photon fluorescence microscopy

Part of the inaugural thesis is to be submitted to the medical faculty of LMU Munich.

INTRODUCTION

Artificial tissue phantoms play an essential role in the development and validation of medical equipment.[1] Usually, artificial phantoms are designed to mimic only the macroscopic behaviour, i.e., spatially averaged properties of the biological tissue to be represented, for example, for a comparison of medical treatment methods.[2] This is useful if the system under development or investigation does not use image forming optics. For microscopy and microendoscopy, developing an equivalent artificial phantom is more demanding because of the requirement to implement and control small structures comparable to those of the biological tissue, and because of the related accuracy. For tissue diagnosis based on general microscopic methods, it is often necessary to know up to which depth meaningful images can be expected, that is, images in which structural features known to be present within the sample can still be visually distinguished. Such information is easy to obtain at a modern research microscope, since these microscopes are equipped with a motorized stage for precise movements in x, y and z-direction. Rather simple, that is, macroscopically homogeneous artificial tissue phantoms can be used in this case, such as an agar phantom with embedded scattering centres and fluorescent spheres,[3,4] gold nano-rods,[5] or a liquid phantom.[6]

In this case, the imaging depth, that is, the depth of the focal plane below the phantom surface, can simply be varied using the z-drive of the microscopy stage. In the case of endoscopic systems, both widefield or scanning type, the situation can be more difficult since they usually lack a positioning stage or provide only restricted positioning capabilities. In such cases[7–11] and particularly in the case of fixed focus systems, the accessible depth range, the depth calibration, and the imaging quality in that range have to be assessed in a different way. Constructs designed for the evaluation of fluorescence cameras[12,13] target these problems on a macroscopic scale, but they are not suited for scanning, especially depth-scanning microscopy, and microendoscopy systems. Tissue phantoms based on fluorophore- or blood-filled glass capillaries[14,15] have been examined. These contain structures in the range of about ≈80 µm. Rather complex skin-mimicking phantoms[16] contain artificial vessel structures in the range of 1 mm diameter. Publications about microstructured tissue phantoms containing finer structures are scarce. Phantoms published in literature are mostly based on stereolithography[17] or two-photon polymerization,[18] but still require a z-stage for depth determination or do not reach structure sizes as small as cellular dimensions.

This study presents an approach for the construction of microscopy- and microendoscopy-suited artificial tissue phantom with modifiable optical properties and fluorescent structures located at well-defined depths within a modifiable medium. This phantom is specifically designed to meet the technical need to characterize clinical optical systems, which very often lack a z-stage. The phantom is based on a microstructured glass surface coated with fluorescent beads and covered with a scattering medium, consisting of non-fluorescent polystyrene beads in a hydrogel (Poloxamer). The artificial tissue phantom was developed for the characterization of a microendoscopic multiphoton fluorescence lifetime microscopy (FLIM) systems for metabolic imaging, therefore it was adjusted to the spectral fluorescence excitation and emission characteristics of nicotinamide adenine dinucleotide (NADH) and flavin adenine dinucleotide (FAD). Fluorescent beads of 1µm diameter were chosen to mimic the size of mitochondria. Optical properties of the scattering medium were adjusted to human epithelial tissue in the upper respiratory tract. Despite this original design the artificial phantom can be adapted to a wide range of applications. Since fluorescent spheres are available for a multitude of spectral excitation and emission characteristics, and the scattering characteristics can be adapted as well, different kinds of biological tissue can be simulated.

Many imaging systems for clinical applications lack the extensive positioning capabilities known from modern research microscopes. To characterize these systems, there is need for a phantom with intrinsic lateral and axial position determination capability. The presented artificial tissue phantom is a step toward this direction. The aim of the development was to design a staircase-like phantom especially for mimicking features encountered when trying to optically diagnose the metabolic states of cells within the epithelial layers in the upper respiratory tract. This application may serve as an example for a variety of further applications.

MATERIAL AND METHODS

In the following sections "Glass structure" to "Scattering medium" the general design and the manufacturing methods of the artificial tissue phantom and applied characterization methods are described. In section "Simulated optical properties" the selection of phantom parameters is described. In section "Imaging" the image recording and analysis methods are described.

Glass structure

Standard microscopy slides (Superfrost PLUS, Art. no. J1800AMNZ, Gerhard Menzel GmbH) were used as substrate for the artificial phantoms. Into these slides, 65 steps of 5 µm step height, 200 µm tread length and 5 mm width were inscribed using a microstructuring laser system (microSTRUCTvario, 3D-Micromac AG) equipped with an ultrashort pulsed laser (Spirit HE 1040-30 SHG, SpectraPhysics) with emission wavelength 520 nm for material processing.

The script for creating the desired step structure was custom written and the machining pattern, number of passes as well as laser power were initially adjusted in order to produce surfaces as even as possible. Figure 1 shows a transmission image of a structured glass slide recorded with a flatbed scanner (CanoScan 8800F, Canon Inc.) and a magnified image recorded with a wide field microscope (DMIRBE, Leica Microsystems GmbH), equipped with a colour camera (DBK 38UX267, The Imaging Source), further referred to as wide-field microscope (WF-microscope). The size of these structures, centred on the slide in x- and y -direction, is specified in the figure. A simplified, not to scale, scheme of the described structure, with the fluorescent spheres coating and scattering medium indicated as described in sections "Fluorescent sphere coating" and "Scattering medium," is shown in Figure 2.

A total of 10 structured slides were manufactured and individually characterized using a three-dimensional (3D) laser scanning microscope (VK-X260K, Keyence Corporation). Evaluation and visualization of the measurements was carried out with VK-X Series Software MultiFileAnalyzer (Version 1.3.1.34, Keyence Corporation), Gwyddion[19,20] version 2.59 and Matlab (The Mathworks Inc.; Version 2018b).

The step heights and tread lengths of 10 manufactured step structures (referred to as St1–St10 in the following) were analysed based on the acquired 3D image stacks as follows. A depth profile $z_i(x_i)$, averaged over 50 adjacent y-planes, was extracted for each analysed structured slide along the x-axis using VK-X Series Software MultiFileAnalyzer (see Figure 3). Each profile was numerically differentiated using Matlab, which resulted in a series of peaks indicating the locations of the steps, that is, of the transitions between adjacent treads. The corresponding peak positions $\hat{x}_i$ were determined using Matlab's `findpeaks` function and the corresponding tread lengths L_i, Equation (1), calculated, taking into account the scanning resolution $\xi = 0.697\,\mu m$ of the microscope. The midpoint positions of the treads were defined in the centre between two adjacent step positions as $\bar{x}_i$, Equation (2). The depth positions $\bar{z}_i$ of the treads were determined by averaging the profile $z_i(x_i)$ over $\pm 50\, x_i$ positions around the x_i position closest to the midpoint position $\bar{x}_i$ (corresponding to an average over 101 datapoints or 69.7 µm). The step heights of the steps were then defined by the corresponding depth difference between the two adjacent treads as H_i, Equation (3), taking into account the z-resolution of the analysed image stack. The tread lengths and step heights of the examined structures were represented graphically and the mean and standard deviation calculated.

$$L_i = \left(\hat{x}_{i+1} - \hat{x}_i\right) \times \xi \tag{1}$$

$$\bar{x}_i = \left\lfloor \frac{\hat{x}_i + \hat{x}_{i+1}}{2} \right\rfloor \tag{2}$$

$$H_i = \bar{z}_i - \bar{z}_{i-1} \tag{3}$$

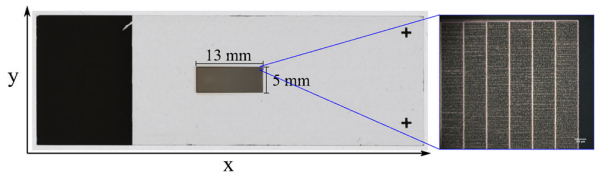

FIGURE 1 Sample image of an uncoated, unsealed, glass structure; standard microscopy slide, 76 × 26 mm, magnification of region within the small blue rectangle is shown in the right image: WF-microscope with objective PL Fluotar ×10/0.30 PH 1 phase contrast, scale bar is 100 µm.

Fluorescent sphere coating

The slides, like the one exemplary shown in Figure 1, were cleaned before each imaging using a lab washer (Miele Professional PG 8593) and coated with blue and yellow/green fluorescent beads of 1 µm diameter (FluoSpheres F8814 and FluoSpheres F8823, respectively, both Thermo Fisher Scientific). The beads were chosen to mimic the fluorescent properties of NADH and FAD since the phantom was designed for testing equipment for metabolic imaging. Figure 4 shows a comparison of the beads two-photon fluorescence spectra with that of NADH (N8129, Sigma-Alrich GmbH) and FAD (ALX-480-084-M050, Enzo Life Sciences GmbH) solutions in 7.5 pH TRIS buffer (BU-125S, TRIS 1 M pH 7.5, Jena Bioscience GmbH). The two-photon spectra were recorded with a multiphoton FLIM microscope described previously.[21]

To fix the fluorescent beads on the steps, they are dispersed (1 µl of each fluorescent beads suspension) in

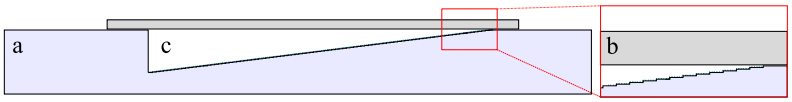

FIGURE 2 Simplified scheme of structure; (a) glass microscopy slide, (b) coverslip, and (c) pluronic solution (with or without scattering agent); image magnification (red): detailed view; the coating with fluorescent beads is indicated by blue and green dots on the horizontal planes of the step structure.

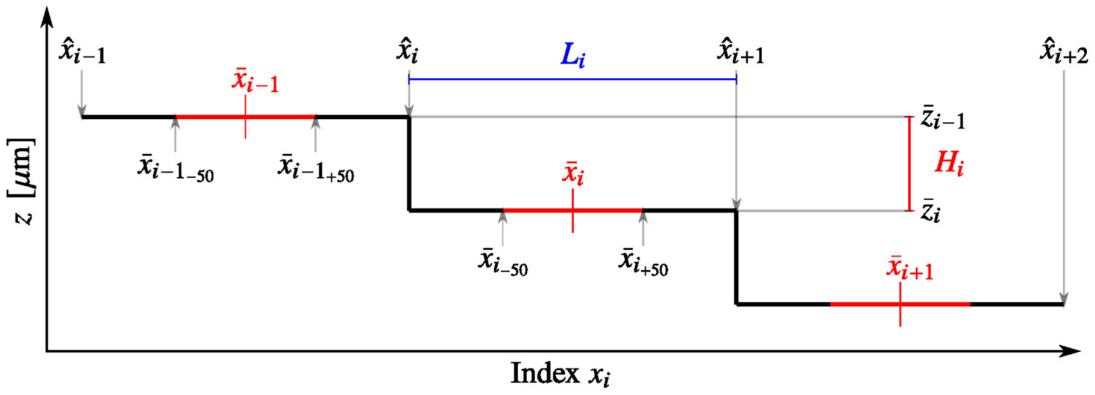

FIGURE 3 Scheme for calculating step length and step height of a step structure (not to scale).

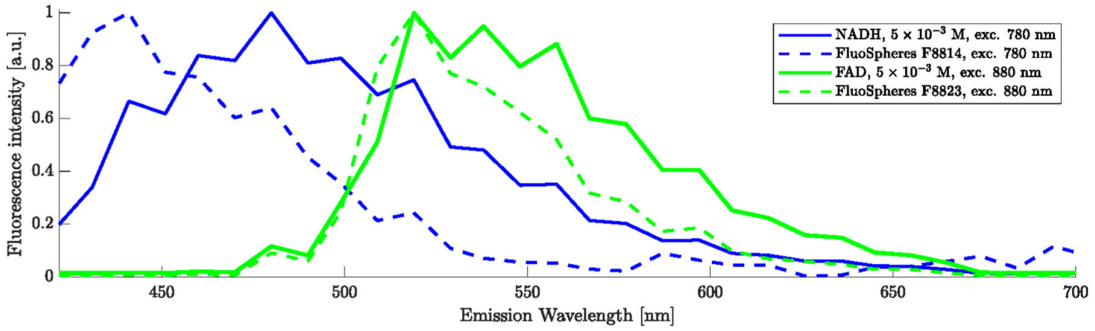

FIGURE 4 Comparison of the normalized two-photon fluorescence spectra of NADH, FAD, and blue and yellow/green fluorescent beads.

500 µl 0.9%w/w polyvinyl alcohol (PVA) solution (Art. no. 563900 Poly(vinyl alcohol), Sigma-Aldrich GmbH). Approximately 10 µl of the mixture is filled into the structures using a pipette, distributed to cover the whole structure and a small rim on the surface of the glass slide. The filled structure was then dried on a hot plate (RCT basic, IKA Labortechnik) at ≈60°C and subsequently wrapped in aluminium foil for light protection until further use. The position of the fluorescent sphere coating is indicated by tiny blue and yellow dots in the scheme in Figure 2.

The adherence of the fluorescent bead coating was checked during imaging with a multiphoton microscope and in one case additionally, after 14 days storage, using a confocal microscope (TCS SP8 WLL AOBS with objective HC PL APO CS2 ×10/0.40 DRY objective, both Leica Microsystems GmbH), further referred to as CF-microscope.

Scattering medium

To mimic light scattering in tissue, a scattering agent consisting of an aqueous 13%w/w Pluronic solution (Art. no. P2443, Sigma-Aldrich GmbH) and non-fluorescent polystyrene beads of 1 µm diameter (Polybead Microspheres 1.00 µm, Cat. no. 07310-15, Polysciences Europe GmbH) was prepared and refrigerated until use. The scattering suspension was checked for homogeneity by visual inspection using the WF-microscope with objective HCX PL Fluotar ×20/0.50 PH 2 (Leica Microsystems GmbH). Then ≈10 µl were filled in the indentation of the structure, which was then closed by a cover glass (VWR Cover Glass no. 1.5, Cat. no. 631-0136, VWR International GmbH) and sealed around the edges of the coverslip using a mounting medium (Eukitt 03989, Sigma-Aldrich GmbH). The position of the scattering medium in the glass structure is indicated as white area in the scheme in Figure 2.

For imaging with the FLIM platform (see chapter "Imaging" for description) the cover glass was substituted with cling film. This was necessary because the working distance of the custom made endoscope was between 25 and 100 µm, therefore a standard cover glass could not be used. Preliminary experiments with a multiphoton FLIM microscope (described in Freymüller et al.[21]) showed no significant reduction in image quality or introduction of detectable aberrations when a cling film was brought into the imaging path.

The concentrations of non-fluorescent polystyrene beads were adjusted, based on calculations of Mie

scattering taking the refractive index of the surrounding medium and the non-fluorescent beads into account, so as to mimic the scattering properties of a selected biological tissue (in this case oral mucosa). The Pluronic solution was modelled with a wavelength dependent refractive index identical to water[22,23], for the non-fluorescent beads the wavelength dependent refractive index of polystyrene[24,25] was used. The reduced scattering coefficient μ_s' for a given mixing ratio of Polybead suspension and water/Pluronic solution was calculated based on Mie theory.[26] A customized Matlab algorithm based on literature[27,28] was implemented for the Mie calculations and for the iterative determination of the mixing ratio required to obtain a given value of the reduced scattering coefficient μ_s'.

The resulting optical parameters were evaluated using an existing integrating sphere measurement setup described previously.[29] The setup, originally equipped with a white light source (DLight 201332 20, Karl Storz SE & Co. KG), was extended by integration of a 780 and 880 nm laser diode (LDM780/3LJ and LM-104-E002, respectively, both Roithner Lasertechnik GmbH). Polarization effects were not taken into account as they were supposed to be negligible due to multiple scattering events within the scattering medium.[30]

The degradation of one artificial tissue phantom over the time course of 7 days was assessed by imaging with the transmitted light detector (TLD) of the CF-microscope at three different points in time: immediately (i.e., within 2 h) after preparation and after keeping it 3 and 7 days at room temperature ($\approx 20°C$), wrapped in aluminium foil for light-protection. Degradation was defined qualitatively as any visible change in the phantom over time in comparison to the state immediately after preparation, as revealed under a microscope. This especially refers to aggregation/clotting or sedimentation of spheres in the scattering medium, detachment of the fluorescent spheres, or an eventual growth of bacteria or mold.

Simulated optical properties

In this section, the optical phantom parameters realized with the methods described in sections “Fluorescent sphere coating” and “Scattering medium” are specified. The aim pursued with the proposed artificial phantoms is to provide a well-defined, repeatable construct for acquiring optical resolution data dependent on the depth of the observed structure in the phantom. An important field of application is metabolic imaging by means of multiphoton FLIM. Therefore, the study was focused on two-photon excitation using wavelength between 700 and 900 nm, specifically 780 and 880 nm, and an emission wavelength range of 400–600 nm, as this corresponds well to the fluorescence characteristics of NADH and FAD, the most important fluorophores for the investigation of cell metabolism. An ideal artificial tissue phantom would have two-photon excitation spectra and corresponding emission spectra exactly matching those of real biological cells or tissue, even in mixtures representing situations with coexisting cells in different states. This is practically impossible to achieve, even more in mixtures where different absorption and scattering agents may affect or interfere with each other. Since an artificial phantom has to be similar, but not identical[1] to what is simulated, the focus was primarily on the excitation wavelengths. Here the choice of excitation wavelength was motivated by existing two-photon FLIM microscopy systems to be examined and compared. In all cases, NADH, FAD and their artificial phantom analogues can be excited at 780 nm, and only FAD and its artificial phantom analogue can be excited at 880 nm. Also, the emission spectra of NADH and FAD are sufficiently similar to those of their chosen artificial phantom analogues.[21]

Literature on optical properties of human oral tissue in the relevant wavelength range proved to be sparse. Data was found for the human maxillary sinus as a graph[31] and for different oral and colon tissues at 855 and 1064 nm Values of μ_s' at the relevant wavelengths 780 and 880 nm were therefore derived from Bashkatov et al.[31] with a digitizer tool[33] and used for calculating the composition of the scattering suspension.

To prepare scattering suspensions with optical parameters corresponding to human maxillary sinus according to Table 1 ($\mu_{s\ 780nm}' = 1.002\ mm^{-1}$ and $\mu_{s\ 880nm}' = 0.802\ mm^{-1}$), non-fluorescent spheres suspension and Pluronic solution were mixed in the ratios determined with the customized Matlab algorithm for Mie calculations based on literature[27,28], as described in section “Scattering medium". To check the repeatability of the optical properties of the prepared scattering medium and their consistency with the respective target values, the scattering suspension for 780 nm was prepared three times and measured three times each, the suspension for 880 nm was prepared one time and measured three times using the existing integrating sphere setup[29] with modifications as described in section “Scattering medium".

Imaging

The prepared structures were imaged using a multiphoton FLIM microscope (TCS SP8 DIVE FALCON multiphoton fluorescence lifetime microscope on an upright DM8 stand and a HC IRAPO L 25x/1.00 W motCORR objective, both Leica Microsystems GmbH), further referred to as multiphoton microscope MP-microscope. The microscope was equipped with a

Tissue	λ (nm)	μ_a (cm^{-1})	μ_s (cm^{-1})	μ_s' (cm^{-1})	g
Oral mucosa: Normal Tissue[32,p283]	855	–	27 ± 11	2.7	0.9
Oral mucosa: Dysplastic Tissue[32,p283]	855	–	39 ± 6	3.9	0.9
Oral mucosa: Sqaumous cell carcinoma[32,p283]	855	–	60 ± 9	6	0.9
Colon: Muscle[32,p261]	1064	3.3	238	16.66	0.93
Colon: Submucous[32,p261]	1064	2.3	117	10.53	0.91
Colon: Mucous[32,p261]	1064	2.7	39	3.51	0.91
Colon: Integral[32,p261]	1064	0.4	261	15.66	0.94
Human maxillary sinus[31]	780	0.17	–	10.02	0.9
Human maxillary sinus[31]	880	0.14	–	8.02	0.9

TABLE 1 Literature values[31,32] for human mucosa tissues; values for human maxillary sinus[31] extracted using a digitizer tool[33]

motorized stage (Motorised Moveable Base Plate [MMBP], Scientifica Limited) and a titanium sapphire laser (Insight Dual 067, Spectra Physics). The fluorescent spheres were excited at 780 nm and their fluorescence was detected in the spectral regions 426–466 nm (further referred to as blue channel) and 542–582 nm (further referred to as green channel) by internal hybrid detectors (Leica HyD, pinhole open for multiphoton imaging). Additional imaging was done using the confocal part of the MP-microscope in reflection mode (imaging excitation laser at 500 nm, detection by internal photomultiplier, pinhole at 1 AU) to image the boundaries of the structure in x-direction for preliminary positioning and slope correction of the slide (the corresponding positions are indicated by two green squares in Figure 5).

To characterize the step structures, z-stacks were performed at selected x-positions between the two reference points, indicated exemplarily as small blue squares along the blue connecting line in Figure 5. At each selected position, a z-stack of either 20 or 40 µm height and 1 µm spacing along z was acquired with one of the settings listed in Table 2, resulting in identical lateral and axial resolution for every imaging stack. The image quality is not expected to change with increasing depth.[34] Nevertheless, an analysis was done to confirm that the designed artificial tissue phantom behaves according to expectations and no undesired effects are introduced. To check for a possible change in image quality with increasing imaging depth, from six different depths, five spheres per depths value and spectral detection channel were randomly chosen and their horizontal intensity profile extracted using LAS X (Leica Microsystems GmbH). These profiles were fitted with a Gaussian profile using Matlab. The mean and standard deviation (SD) of the obtained full width at half maximum (FWHM) were determined for each spectral detection channel. A Kruskall–Wallis test with $p > 0.05$ regarded as significant was done using Matlab to check whether the differences of the obtained FWHM values are significant.

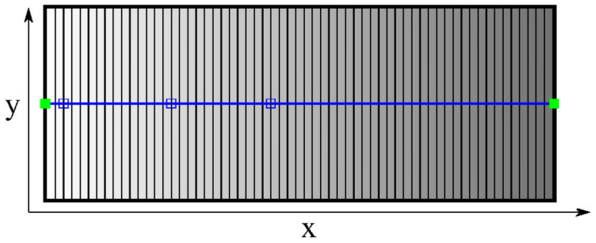

FIGURE 5 Scheme of imaging positions; green squares: imaging positions for slope correction; blue line: imaging direction along x-axes with exemplary indication of imaging stack positions.

Multiphoton images from within a scattering medium can generally be obtained from depths corresponding to two to three times the mean scattering free path l_s.[3,34] For the chosen scattering parameter of $\mu_{s\ 780nm}' = 1.002\ mm^{-1}$ this would be up to $3 \times l_s \approx 300$ µm. It is therefore expected that multiphoton images can be acquired over the whole depth range of the step structures that exhibit a maximum depth of 65 × 5 µm = 325 µm.

A preliminary test with the FLIM part of the MP-microscope was conducted to check if sufficient numbers of photons for a successful fluorescence lifetime fit (fluorescence lifetime imaging of the fluorescent spheres results in clearly recognizable exponential decay curves and a successful fitting process) could be gathered within the entire depth range of the prepared structures. The fluorescence lifetime analysis and fitting was done using a mono-exponential decay function and binning 1 in the FLIM module of LAS X.

The MP-microscope system served as reference for the exemplary performance check. Images for assessing the aging of the prepared artificial phantom were acquired using the CF-microscope. Image preparation and analysis was done using Fiji,[35] LAS X, and Matlab.

To demonstrate the artificial tissue phantom is suitable for comparing different imaging systems,

TABLE 2 List of used imaging parameters MP-microscope

Setting	Zoom factor	*xy*-pixel	FOV (μm)	*xy* resolution (μm)	*z* spacing (μm)
1	1	2048	442.86	0.21634	1.0
2	2	1024	221.43	0.21645	1.0

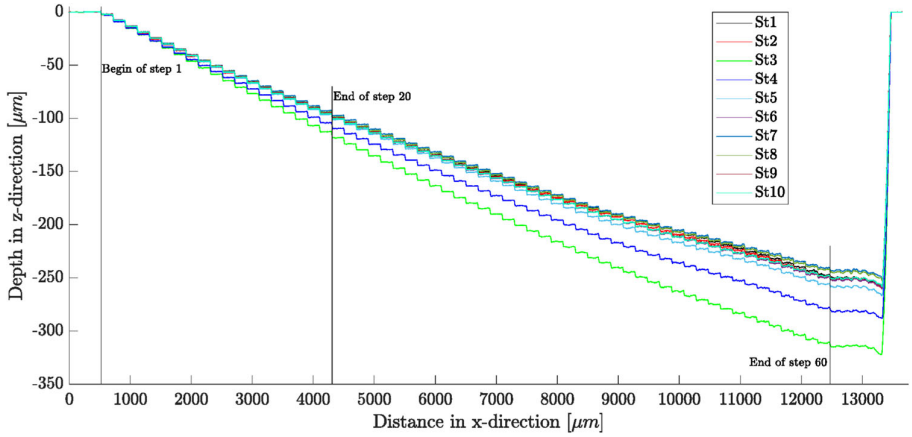

FIGURE 6 Depth profile of structured slides St1–St10.

including systems without *z*-stage, images were acquired using a modified FLIM platform for dermatology (MPTflex, JenLab GmbH). It contained two femtosecond fiber lasers emitting at 780 and 880 nm (TOPTICA Photonics AG) and a hybrid detector (Becker&Hickl GmbH) and was equipped with a custom-made endoscope for the exploration of clinical applications, further referred to as FLIM-platform. In contrast to the microscopes, the FLIM-platform provided no tuneable spectral detection, but fluorescence signals were always collected within the broad wavelength range 409–660 nm by the FLIM detector. Thus, no further discrimination of fluorescence contributions was possible, apart from choosing one of two available excitation wavelengths. The recorded data were stored in Becker&Hickl *.sdt* files. To obtain time-integrated images, these files were imported into Fiji[35] and converted into an intensity image by integrating the photon numbers over all time channels for each pixel.

MP-microscope, CF-microscope, and FLIM-platform images of an artificial phantom were recorded to conduct a visual comparison of the resulting images.

RESULTS

Glass structure analysis

In Figure 6 the depth profile of the 10 analysed structured slides are shown. Between 61 and 63 steps per structure could be clearly distinguished by the implemented algorithm.

However, in the evaluation of the tread length and step height only the first 60 steps per structured slide were included, hence with the end of the 60th step there is no further descent but a hill-like structure with regular indentations, as can be seen in Figure 6.

With the exception of St3 and St4 the analysed structures overlap very well up to until step 20 ($x \approx 4000$ µm) and begin to deviate from there on. For St3 and St4 the edges of each step are still in the same positions in *x*-direction as for the other eight structures, but they start to deviate from those early, due to larger step heights.

The length of the treads of the individual structures are shown in Figure 7 as a function of the step index for the individual structures. They proved to be uniform with only slight deviations to the design of 200 µm length, the only exception being step number 41, which is ≈184 µm in length. Since this reduction in length occurs in all structures at the same position and to the same extent, it is likely to be caused by the manufacturing process, namely the programmed laser ablation pattern.

Mean values and standard deviations of the tread length L_i (59 per structure, as step 41 was excluded) are listed in Table 3.

The step heights are shown in Figure 8 as a function of the step number for the individual structures St1–St10. For all structures, the step height of the first step is ≈1 to ≈3 µm, that of the second step is ≈6 µm and the step height decreases to ≈4 µm when reaching step 60. As seen in Figure 8, St3 and St4 deviate from the other structures by having a slightly higher step height in general, which explains the greater overall depth observed for these two

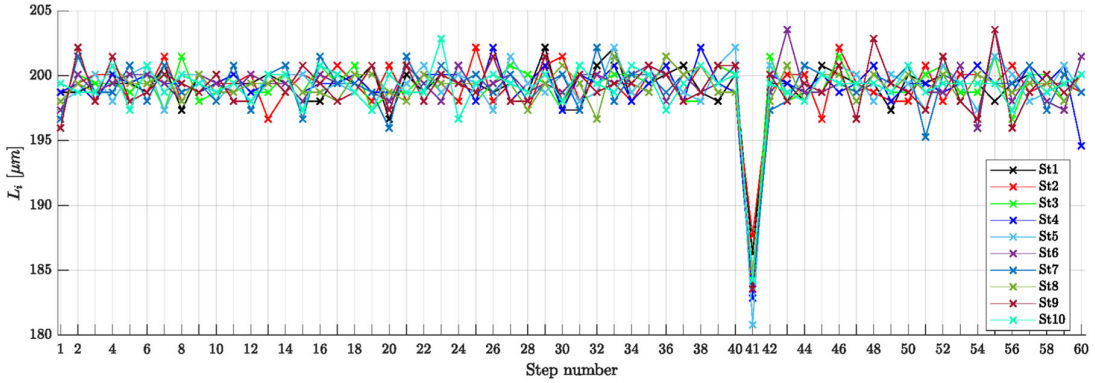

FIGURE 7 Tread length L_i of 60 steps from profiles St1–St10; the systematically shorter step 41 can clearly be distinguished.

TABLE 3 List of used imaging parameters MP-microscope

Structure	St1	St2	St3	St4	St5	St6	St7	St8	St9	St10	total
Mean (µm)	199.33	199.37	199.37	199.39	199.42	199.39	199.34	199.32	199.30	199.33	199.36
SD (µm)	1.1	1.22	1.18	1.17	1.21	1.27	1.44	1.00	1.59	1.11	1.23

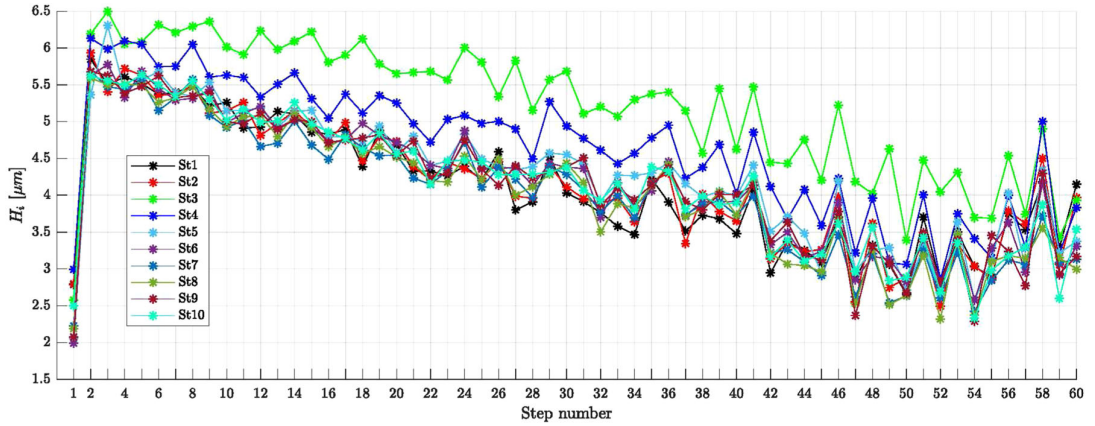

FIGURE 8 Step height H_i of individual steps for structures St1–St10; St3 and St4 deviate from the others due to overall higher step height.

structures in Figure 6. The steps of the other structured slides, except St3 and St4, follow each other with small variations.

Fluorescent spheres coating

The durability of the fluorescent spheres coating was checked during imaging with the MP-microscope in the imaged sample regions. One slide was kept in refrigeration after initial imaging with the multiphoton microscope, checking was done with the CF-microscope at random positions (excitation at 405 nm, detection ranges blue spheres 420–470 nm, yellow/green spheres 510–600 nm). Except for single fluorescent spheres, no detachment of the coating could be detected in the examined areas, neither immediately after preparation or 14 days after preparation. Figure 9 shows a confocal image stack of the first two steps of structure St2 at 14 days after preparation. The steps are clearly distinguishable, and no detachment of the coating is visible.

Optical properties of scattering media

To prepare scattering suspensions with optical properties corresponding to human maxillary sinus according to calculations based on Table 1, 1 ml non-fluorescent spheres suspension was mixed with 5.33 ml water/Pluronic solution to obtain $\mu_s' = 1.002\ \mathrm{mm}^{-1}$ at 780 nm

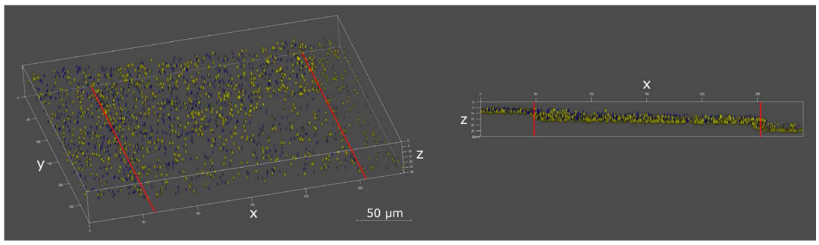

FIGURE 9 Structured slide St2, confocal image stack of fluorescent sphere coating 14 days after preparation (CF-microscope, $\lambda_{ex} = 405\,nm$, blue: blue fluorescent spheres, yellow: yellow/green fluorescent spheres), transitions between steps highlighted in red.

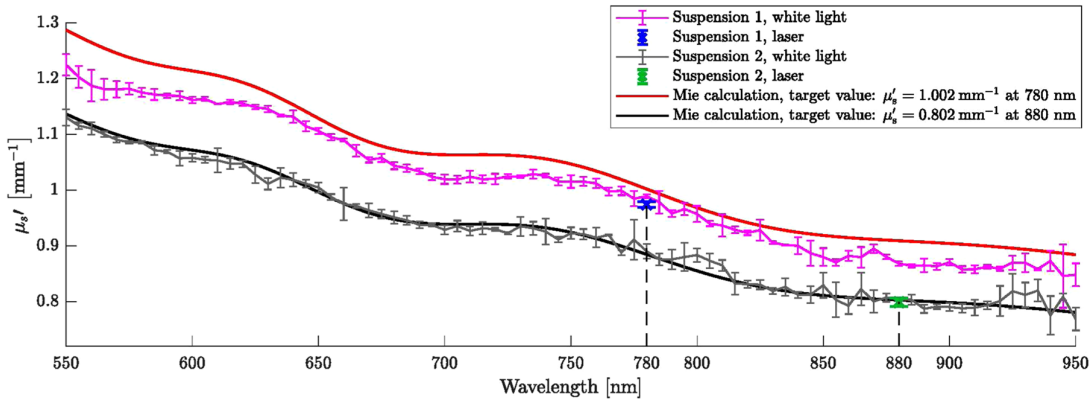

FIGURE 10 Mie calculation results for the reduced scattering coefficient of Suspensions 1 and 2 in comparison with integrating sphere measurements performed with a white light source and two laser diodes emitting light of 780 and 880 nm wavelength.

and with 6.17 ml water/Pluronic solution to obtain $\mu_s' = 0.802\ mm^{-1}$ at 880 nm, referred to as Suspension 1 and Suspension 2 in Figure 10. The optical properties of the resulting scattering suspensions were determined as described in section "Scattering medium" using an integrating sphere setup as described in section "Simulated optical properties". In the case of the 780 nm suspension, only seven of the nine measurements conducted with the 780 nm laser diode were usable. A comparison of the measured μ_s' values and Mie calculations is shown in Figure 10 (mean and SD of three measurements per suspension). Overall, the measured values and corresponding Mie calculations are in reasonable agreement, although the deviations are clearly larger in the case of the suspension designed for 780 nm.

In Table 4 the μ_s' values for the two wavelengths are shown for different selections of the experimental results.

In Figure 11, transmission images of a phantom are shown that were obtained with the TLD of the CF-microscope within 2 hours after preparation and after 3 and 7 days of storage at room temperature, respectively. The images show that the non-fluorescent scattering spheres (black dots) tend to clot together over time and accumulate.

From the conducted experiments the timeframe for usability of the phantom is about one day from the time of applying the scattering medium. After this time period, the glass structure has to be cleaned and recoated, and new scattering medium has to be applied as described.

TABLE 4 Mean values of μ_s' measured at 780 and 880 nm

Target Light source	$\mu_{s\ 780nm}' = 1.002\ mm^{-1}$		$\mu_{s\ 880nm}' = 0.802\ mm^{-1}$	
	μ_s' (mm^{-1}) measured	*n*	μ_s' (mm^{-1}) measured	*n*
WL	0.966 ± 0.021	9	0.8041 ± 0.0014	3
L	0.955 ± 0.020	7	0.7988 ± 0.0077	3
WL + L	0.961 ± 0.021	16	0.8015 ± 0.0057	6

Abbreviations: L, laserdiodes (780 and 880 nm, respectively); *n*, number of measurements; WL, white light source.

Imaging

A 3D rendering of a multiphoton imaging stack recorded with the MP-microscope around steps 9–10 (referring to a depth of 46 and 51 µm, respectively) within structured slide St5 is shown exemplarily in Figure 12. For the six steps listed in Table 5 together with the corresponding depths within the scattering medium, the brightest 2D image was extracted from the corresponding stack.

The first steps showed an increased density of fluorescent spheres compared to deeper ones. The laser power required to obtain an image from deeper areas was significantly increased.[36] However, a visual comparison

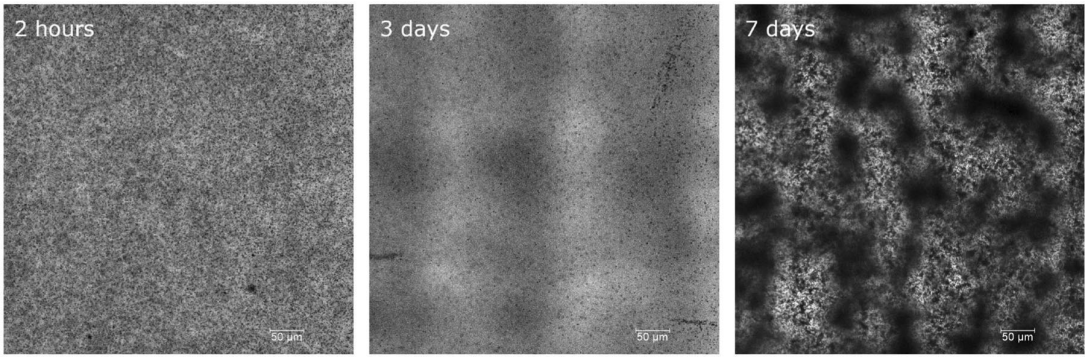

FIGURE 11 Detailed view of artificial phantom recorded at different times after preparation (2 hours, 3 days, and 7 days), at 2 hours the non-fluorescent spheres (black dots) are homogeneously distributed, at 3 days beginning of clotting is visible, at 7 days the non-fluorescent spheres are clotted to cloud like structures; CF-microscope, objective HC PL APO CS2 ×10/0.40 DRY, FOV 516.67 µm; *x*/*y* resolution 0.5 µm/pixel; scale bar is 50 µm.

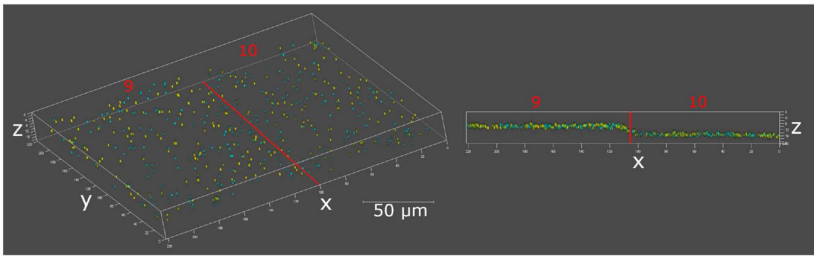

FIGURE 12 Structured slide St5 with scattering medium, steps 9 and 10 referring to depth of 46 and 51 µm, respectively; steps 9 and 10 marked and transition between steps highlighted by a red line in left image; MP-microscope, λ_{ex} = 780 nm, cyan: blue fluorescent beads, yellow: yellow/green fluorescent beads.

TABLE 5 Mean and standard deviation of FWHM of five fluorescent spheres per depth and channel and relative laser-power for excitation at 780 nm for images of six steps at increasing depth (MP-microscope).

Step **Depth (µm)**	**1** **2**	**10** **52**	**19** **96**	**29** **142**	**39** **184**	**59** **252**
FWHM blue channel (mean ± SD) µm	0.773 ± 0.097	0.79 ± 0.11	0.83 ± 0.16	0.83 ± 0.11	0.88 ± 0.10	0.77 ± 0.14
FWHM green channel (mean ± SD) µm	0.817 ± 0.020	0.771 ± 0.019	0.785 ± 0.031	0.753 ± 0.044	0.789 ± 0.023	0.788 ± 0.076
Relative laser power (% AOM)	0.5	0.8	1.7	3.6	5.4	21

shows, as expected from literature,[34] no detectable degradation of image quality with increasing depth. To confirm this, from each depth listed in Table 5, five spheres per depth value and spectral detection channel as described in chapter "Imaging" were randomly chosen and their horizontal intensity profile extracted and fitted with a Gaussian profile to retrieve the FWHM. The mean and SD of the obtained FWHM values for each spectral detection channel are collected in Table 5. The performed Kruskal–Wallis test on the FWHM values obtained for every depth and channel (blue channel: $p = 0.7684$, green channel: $p = 0.1269$) showed no difference between the six imaging depths, which confirms the visual impression of basically constant image quality regardless of depth and is therefore consistent with the expected behaviour.[4] The SD is found to be systematically larger for the blue channel. This is probably caused by the blue fluorescent beads being less excitable at the chosen wavelength, which was deliberately desired as described in the chapter "Fluorescent sphere coating".

A preliminary FLIM test with the MP-microscope, excitation wavelength of 780 nm, was carried out on one structured slide with scattering medium. It was possible to obtain FLIM images from the whole depth range of the structure and to obtain a useful fluorescence lifetime fit in both the blue and the green detection channel. Fluorescence lifetime fitting was done monoexponentially with binning 1.

The depth positions and obtained fluorescence lifetime values of the fluorescent beads are shown in Table 6 and graphically in Figure 13. The fluorescence lifetimes are different for the two kinds of fluorescent spheres, which is not unexpected since they contain different fluorophores. The measured fluorescence lifetimes are shorter between 2.1 and 23.2 µm depth compared to the lifetime values obtained from depth 0 µm (without scatterer overlaying the fluorescent spheres) for both spectral detection channels. The measured fluorescence lifetimes increase at a depth of 49.8 µm and decrease from there on until the deepest measured point (238.8 µm). For both spectral detection channels, the observed change of fluorescent lifetime with depth is greater than the SD of the data. Additionally, the change in fluorescence lifetime is almost equal for both channels in a way that the difference between the two fluorescent lifetimes does not change with increasing depth but stays relatively constant at $(0.800 \pm 0.048)\,ns$.

Due to the different nature of the imaging systems included in the comparison between the MP-microscope, CF-microscope and the FLIM-platform, it was not possible to capture images of the glass structures with the same imaging parameters, specifically magnification, number of pixels and detection filters, as mentioned in the description of the FLIM-platform.

The exemplary comparison of three pairs of images representing two depths (Z1 and Z2) within an artificial phantom with scattering medium coated with fluorescent spheres (1 µm diameter) recorded with three imaging devices (MP-microscope, CF-microscope, FLIM-platform) is shown in Figure 14. These are the time-integrated images recorded with the FLIM-platform, confocal images recorded with the same spatial resolution (CF-microscope, excitation 405 nm, detection range 510–600 nm) as the FLIM-platform and images recorded with the MP-microscope (with the spatial resolution according to setting 2 in Table 2). A precise comparison of the imaging quality between the FLIM-platform (and also the CF-microscope) and the MP-microscope is not possible based on these images, because the scan point densities were different and in case of the FLIM-platform (and also the CF-microscope) not high enough to fulfil the sampling theorem[37] with respect to the available optical resolution and the size of the fluorescent spheres. The on-purpose equally undersampled images obtained with the CF-microscope (see Figure 14) show similar structures as those recorded with the FLIM-platform, so at least a comparison at this level is possible. This comparison reveals a few differences. In the FLIM-platform image recorded at Z1 position, it looks like the focal plane is cylinder-shaped with the cylinder axis pointing along y, whereas the image recorded at Z2 position seems to have a slight slope along the y-direction, and from the middle of the image upward, similarly represented fluorescent spheres seem to be arranged along a roughly semicircular bent grid. In the images recorded with the CF-microscope the two z-positions are clearly distinguishable by the fact that fluorescent spheres, resting on two adjacent treads, are in the focus and thus visible only on the left (Z1 position) or on the right (Z2 position) of the step edge, respectively, highlighted by a red line at the transition between the steps in the figure.

TABLE 6 of the fluorescent beads in the blue and the green detection channel in scattering medium with measured $\mu_{s\,780nm}^{'} = 0.96\ mm^{-1}$, MP-microscope, excitation wavelength 780 nm.

Fluorescence lifetime (ns)					
Depth (µm)	0	2.1	23.2	49.8	97.8
Blue channel	2.736 ± 0.062	2.639 ± 0.038	2.627 ± 0.045	2.759 ± 0.032	2.659 ± 0.037
Green channel	3.584 ± 0.102	3.417 ± 0.055	3.422 ± 0.033	3.588 ± 0.039	3.444 ± 0.048
Depth (µm)	140.3	178.7	210.2	238.8	
Blue channel	2.545 ± 0.024	2.407 ± 0.035	2.411 ± 0.031	2.322 ± 0.040	
Green channel	3.385 ± 0.032	3.265 ± 0.041	3.168 ± 0.047	3.034 ± 0.049	

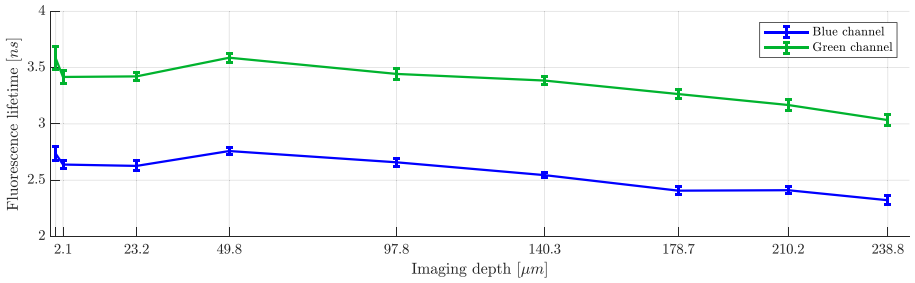

FIGURE 13 Fluorescence lifetime obtained from blue and green detection channels versus depths; individual values see Table 6; fluorescent lifetimes of the blue and green channel over increasing imaging depths.

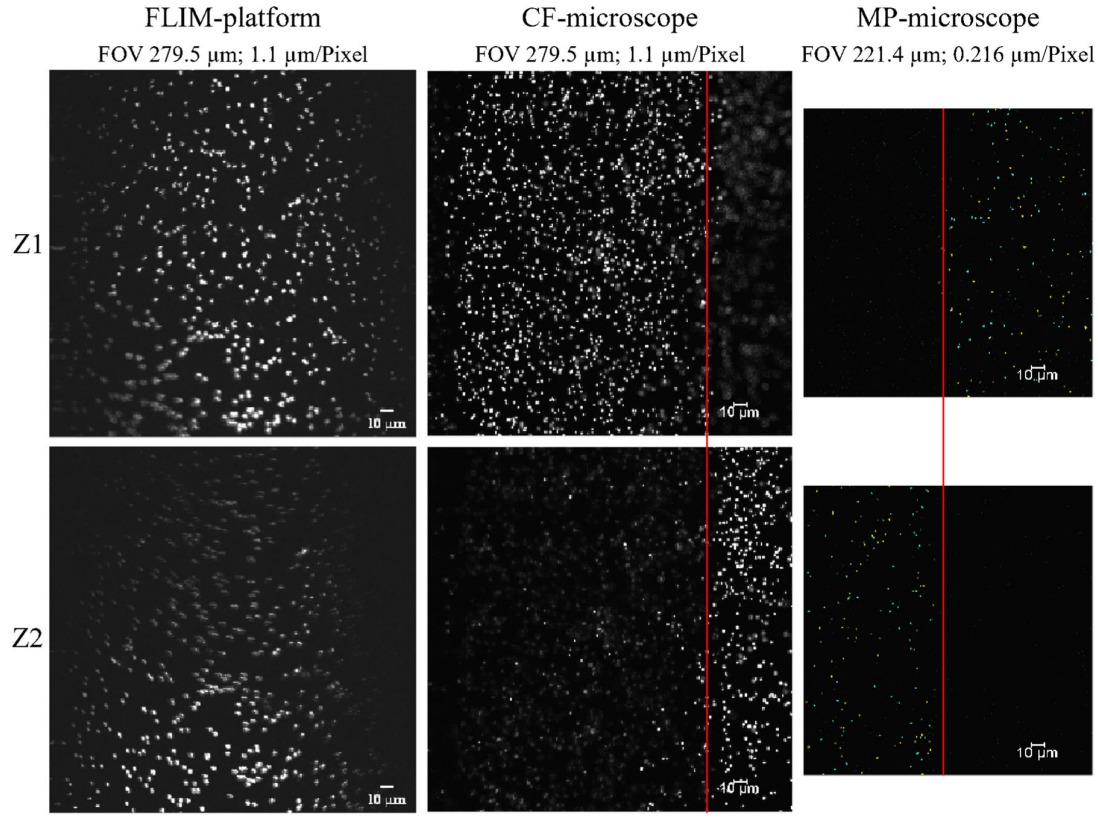

FIGURE 14 Comparison of images obtained with the FLIM-platform (left) and the CF-microscope (middle) with the same field of view (FOV) and resolution settings and the MP-microscope (imaging parameters see Table 2 setting 2) at two different *z*-positions; images are sized to have the same scale; histogram stretching was applied to increase the contrast of the images (original data are provided in the Supporting Information Material); visible transitions between steps in the images are highlighted by red line; CF-microscope objective HC PL APO CS2 40x/1.30 OIL.

In the case of the MP-microscope with NA = 1.0 used for generating the images excited at 780 nm and shown in Figure 14 (3rd column), the theoretical[38] lateral and axial resolution are ≈330 *nm* and ≈1400 *nm*, respectively, which provides the demanded resolution for resolving spheres of 1 µm diameter (corresponding to the size of mitochondria in cells). The images were recorded with a lateral scanning resolution of 0.216 µm and are consistent with the specified theoretical resolution. In case of the CF-microscope with NA = 1.3 used for generating the images in Figure 14 (2nd column), the theoretical[39] lateral and axial resolution are ≈160 *nm* and ≈480 *nm*, respectively, which also meets the specifications for resolving spheres of 1 µm diameter. However, for direct comparability of the images, the lateral scan resolution was set to 1.1µm/pixel to match the scan resolution with that of the FLIM-platform. In contrast to the MP- and CF-microscope, the NA of the custom-built FLIM-platform was not known, but assumed to be >0.5, so that at least a lateral and axial resolution of ≈670 *nm* and ≈5800 *nm* could be expected. Such lateral resolution would be sufficient for resolving mitochondria of about 1 µm diameter as desired, but could not be taken as granted. Since the scan-resolution of the FLIM-platform was fixed at 1.1µm/pixel, the lateral resolution could not be determined quantitatively.

DISCUSSION

It was the objective of the current study to create an artificial phantom which enables the comparison of different imaging systems in a reproducible way. The primary intention of the development was to quantify the maximum imaging depth reachable with a given optical system. The maximum imaging depth is limited, on one hand, by the mechanical contact between sample and objective, on the other hand, via the demand of a certain signal-to-noise level, by the available laser power and integration time. Which of these two limitations is reached first for a given system/sample combination depends on the optical system (supplied light intensity, focus quality, light collection, and detection efficiency) and on the optical properties of the sample, in this study of the scattering layer (adaptable to mimic different types of tissue) above the fluorescent beads. A determination

of the optical resolution was originally not intended since it was not expected to change with imaging depth.[34] But it would be of interest to deepen the investigation in this regard taking the intensity distribution of the fluorescent beads in scattering media into account, which is described in Durr et al.[34] and Dunn et al.[40]

To reach the specified objective, fluorescent beads were arranged within surface-parallel treads at different, but well-known depths within a medium. The bead positions within these sheets are arbitrary, but time-independent, because the beads are fixed on the surface of the prepared treads. The geometry of the treads is determined by the morphology of the laser-manufactured structures. The characterization of the glass structures indicates a good reproducibility of the manufacturing process with regard to the tread length of the inscribed steps, whereas the step height varies considerably and systematically with the step-index. By suitable characterization, however, the depth of each individual tread below the surface of the glass substrate can be determined, so the variation of the step height does not reduce the functionality of the artificial phantom. For enhanced ease of use, a refinement of the manufacturing protocol would be desirable to achieve a constant step height for all steps. The variability of the tread length is very small, as seen in Table 3 ([199.36 ± 1.23] µm for all 590 individual steps). This very small variability should not affect the usability of the phantoms for the intended purpose of depth-dependent optical characterizations. In addition, the treads are slightly inclined with respect to the surface of the glass substrate, which could also be characterized with additional effort, if needed. Furthermore, the treads are not perfectly smooth, but slightly rough on a ≈1 µm micrometer scale, as expected for the used laser microstructuring technique.[41] In comparison to the step height of about 5 µm, this roughness did not affect the functionality of the artificial phantom in this study. The same holds for the step flatness, which, according to Figure 6, obviously increases with increasing depth, but remains smaller than the step height for all depths up to step 60. This is obviously not crucial, given that the axial resolution in the case of the experiments with the FLIM-platform was theoretically estimated to be $\approx 5800\,nm$. However, the step flatness may pose a limitation in the characterization of imaging systems, depending on the axial resolution of the system under investigation. Due to the mentioned limitations, it might be worthwhile to also explore alternative manufacturing processes like etching[42] or multiphoton lithography.[43]

The method chosen to fix the fluorescent beads on the prepared treads follows a known approach in the field of microscopy for the fixation of micro- or nanoparticles to surfaces.[44] The fixation of the fluorescent beads proved to be stable for at least 14 days and the PVA did obviously not inhibit their fluorescence. The fluorescent beads were chosen based on the similarity of their spectral excitation and emission characteristics with those of NADH and FAD, because the phantom was codeveloped with the modification of a multiphoton tomography system for metabolic FLIM investigations.[45,46] The prepared structures are not limited to this use case, since fluorescent spheres are available in a variety of diameters and spectral excitation and emission characteristics. These properties can be chosen to match the requirements for the system to be tested. The proposed phantom was especially designed for mimicking features encountered when trying to optically diagnose the metabolic states of cells within the epithelial layers in the upper respiratory tract. A minimum accessible depth range of ≈100 µm was desired in the present case. The optical properties of biological tissue reported in literature vary considerably, even for one specific species, tissue type and tissue state.[32] For the primary target tissues of this study, the mucosa of human larynx and especially human vocal cords, optical parameters were not available from literature for the used wavelengths which where adapted to the excitation wavelength used for the target chromophores (NADH and FAD) in metabolic imaging. Instead, literature values for human maxillary sinus[32] were chosen, as those were available for the used wavelengths. The reduced scattering coefficients μ_s' of the different tissues may differ slightly, but were deemed to be similar enough for this study, especially when keeping in mind that the crucial characteristic of a phantom is the reproducibility of its properties, rather than exactly matching property values.[1]

To mimic the scattering behaviour of biological tissue, embedding polymer microspheres in a medium of different refractive index is widely used,[1] because it is conceptually simple and the scattering behaviour can be calculated analytically using Mie theory and thereby conveniently adjusted via suitable selection of compositions and particle diameters.[26,27] In Figure 10, the measured data curve for the scattering suspension designed for excitation at 880 nm follows the Mie calculation with only slight deviations. The measured values for the suspension designed for excitation at 780 nm are lower than those of the Mie calculation, and in the range 550–750 nm, the measured curve appears slightly shifted and/or squeezed along the wavelength axis with respect to the curve obtained from Mie calculation. The cause for this observation could not be ascertained as both suspensions were mixed from the same stock materials, and the same Mie calculation algorithm was used for both compositions. Despite the observed deviation, the difference between measurement and calculation is within acceptable limits considering that the refractive indices of the Pluronic solution and the non-fluorescent beads could differ from the assumptions made for the calculations. The integrating sphere measurement system[29] used for determining the optical parameters of the scattering medium is based on the adding-doubling method that is known to yield optical parameters with a

precision of 2%–3%.[47] With this in mind, the reproducibility of the reduced scattering coefficient of the scattering medium is as expected ($\mu_s' = (0.96 \pm 0.02)\ mm^{-1}$ for 780 nm and $\mu_s' = (0.8 \pm \epsilon)\ mm^{-1}$ with $\epsilon < 0.008)\ mm^{-1}$ for 880 nm, see Table 4). Furthermore, the deviation of these measured values of μ_s' and the respective target values (1.002 and 0.802 mm^{-1}, respectively, see also Table 4) is acceptable.

The concentration of the Pluronic solution in which the polymer microspheres were dissolved to form the scattering medium was a compromise between the mechanical and temporal stability of the phantom and the feasibility of preparation and handling of the medium. The ability of Pluronic to form a gel and the stiffness of the resulting gel depends on concentration and temperature.[48–50] Exploratory attempts to immobilize fluorescent beads within a microchannel (μ-Slide VI 0.4, Cat. no. 80606, ibidi GmbH) were performed with a 20%w/w Pluronic/water solution, which forms a relatively stiff gel. These experiments showed no detectable sedimentation of the fluorescent beads for approximately 10 months if kept at room temperature. Preparing the scattering medium with Pluoronic solutions of such high concentrations, however, proved to be very time-consuming (approx. 1 week for preparing one scattering dispersion) and made it very difficult to apply the medium to the glass structures, because this required cooling the syringes or pipettes and/or the glass structure to $\approx 1°C$ to assure a homogeneous distribution of the medium within the glass structure. Suspensions of non-fluorescent beads in pure water, however, sedimented within an hour after preparation and applying the cover glass. Therefore, as a compromise, a 13%w/w Pluronic solution was finally used to prepare the phantoms. At this concentration the solution forms a viscous fluid at room temperature that is relatively easy to apply and kept the non-fluorescent beads in suspension long enough to conduct all necessary imaging experiments. The resulting durability of the phantom of about 1 day is nevertheless not satisfactory. Therefore in a further development of the scattering medium formulation it should be tried to increase the Pluronic concentration to a point where the solutions are still relatively easy to prepare and handle, but result in a longer suspension time of the non-fluorescent beads. Alternatively, another matrix material for the scattering layer, like silicon resins or a different hydrogel may be investigated in terms of usability and durability.

Multiphoton images could be obtained from depth up to ≈300 μm, corresponding to $3 \times l_s$, within the scattering medium, which is consistent with literature. The image quality was found, as expected in accordance with literature, to not decrease with increasing depth. Both findings prove that the designed artificial tissue phantom behaves as expected from theory based on its design parameters and literature. The observed change in fluorescence lifetime with increasing depth for both types of fluorescent beads adhered to the steps of the structured glass slides is unlikely to be caused by a quenching effect, because the environment surrounding the spheres does not change chemically with increasing depth. They are only buried deeper inside the scattering medium. The equal change in fluorescent lifetime versus depths for both fluorescent beads indicates that the cause of the lifetime change is present at and equal for both types of beads and both detectors used, since they are affected in the same way. The only apparent difference, set aside the necessary increase in excitation laser power to be able to excite the fluorescent beads, is the increasing amount of scattering medium on top of the fluorescent beads and therefore a change in system geometry. Since a change of geometry can influence fluorescent lifetimes measured in scattering media,[51] it is assumed that this is the cause for the observed changes in fluorescent lifetime. To study these effects further was not the scope of the presented work. These findings have to be addressed in further studies since techniques like metabolic imaging depend on the accurate determination of fluorescence lifetimes and are, if used in vivo, likewise conducted in scattering tissue. Therefore, geometry-related shifts in the apparent/fitted fluorescent lifetimes of the involved fluorophores should be taken into consideration in such investigations.

The performed feasibility test of comparing MP-, CF-microscope and FLIM-platform incl. endoscope should show how a potential characterization scenario could look like for a system with unknown properties and if any differences between a known and an unknown system become recognizable as shown in Figure 14. It was possible to obtain images of the prepared step structures with the FLIM-platform and the custom-made endoscope. A direct comparison of the spatial resolution between the MP-microscope and the FLIM-platform was unfortunately not possible due to limitations in the instrument settings of the FLIM-platform. Therefore, additional images were recorded with the CF-microscope, with a spatial resolution corresponding to that of the FLIM-platform. The comparison revealed a reduced image quality of the FLIM-platform. It was not possible to distinguish adjacent steps with this system, the images seemed to be vignetted, a kind of a cylindrical distortion was observed in the images, and the fluorescent beads exhibited semicircular shapes in some areas of the images. Images recorded with this system on real biological tissue showed similar artifacts. Simulation data and transmitted light images of an USAF target made with the custom-made endoscope showed no severe distortions.

Also, an examination of immobilized fluorescent beads at a multiphoton microscope (system described previously[21]) did not indicate that using a cling film instead of a cover glass would distort the images in a way as seen with the FLIM-platform. Therefore, it is assumed that optical components upstream from the endoscope or a mismatch

of the interface between endoscope and FLIM-platform are responsible for the observed features and distortions. This should be part of further investigations.

The developed concept of a modifiable artificial tissue phantom based on a microstructured slide proved to be promising to be able to compare different microscopic and microendoscopic imaging devices and should be explored and developed in further studies.

The maximum imaging depth of a particular system/sample combination can be determined by recording images of the steps inside the phantom, starting from the level of the cover slip and descending the staircase structure step by step, until the image quality drops below an acceptable level (or a mechanical contact between objective and sample occurs). This procedure is also conceivable with endoscope and microendoscope systems. By matching the optical properties of the proposed phantom to the properties of the tissue of interest and the fluorescent beads to the excitation wavelengths of interest, it should be possible to characterize, for example, the depth of field and the maximally reachable imaging depth of endoscopes and micro-endoscopes for fluorescence-assisted diagnosis and treatment.[52–54]

Potential other areas of application could be the characterization of hyperspectral imaging (HSI) cameras, especially endoscopic versions thereof. By replacing the fluorescent by an absorptive coating and adapting the geometric dimensions of the structure, it is conceivable to examine which perfusion parameter[55] determined by the HSI camera can be measured up to which depth in the tissue phantom and, thus, also in vivo. The possible applications are not limited to the ones stated above and should be explored further.

CONCLUSION

In general, laser-machined glass structures could be successfully used to characterize differences in the imaging quality of an endoscopic two-photon FLIM system under development and a high-end research microscope as a reference, as well as to identify possible problems and the related system components. The challenge in designing artificial tissue phantoms for high spatial resolution imaging systems is the adaptation to the specific intended use. Based on the investigation reported here, a large range of different systems could be experimentally characterized with the proposed phantom.

ACKNOWLEDGMENTS

The authors thank J. Janusch, T. Kellerer, M. Saller, S. Dietzel and M. G. Pisfil for their assistance, the Core Facility Bioimaging at the Biomedical Center (BMC) of the Ludwig-Maximilians Universität München (LMU), microscope system funded by a grant of the Deutsche Forschungsgemeinschaft (DFG) (INST 86/1909-1) as well as the Core Facilities of the Musculoskeletal University Center Munich of the Ludwig-Maximilians-Universität München (LMU), microscope system funded by a grant of the Deutsche Forschungsgemeinschaft (DFG) (409-220-1 FUGG) and D. Smeets (Leica Microsystems) for discussions and advice. The work described in this manuscript was performed with the support of the German Federal Ministry of Education and Research (BMBF, project OMOXI, grant no. 13N14507). S. Ströbl was financially supported by Österreichische Forschungsförderungsgesellschaft (grant no. 855657). M. Aumiller was financially supported by the German Research Foundation (DFG) within research training group (RTG) GRK2274. Open Access funding enabled and organized by Projekt DEAL.

CONFLICT OF INTEREST

The authors declare no conflict of interest.

ORCID

Christian Freymüller https://orcid.org/0000-0002-3014-297X
Stephan Ströbl https://orcid.org/0000-0002-0384-0318
Maximilian Aumiller https://orcid.org/0000-0002-1343-6669
Maximilian Eisel https://orcid.org/0000-0002-7321-7302
Ronald Sroka https://orcid.org/0000-0001-7952-2407

REFERENCES

1. Pogue BW, Patterson MS. Review of tissue simulating phantoms for optical spectroscopy, imaging and dosimetry. J Biomed Opt. 2006;11:041102.
2. Markwardt NA, Haj-Hosseini N, Hollnburger B, Stepp H, Zelenkov P, Rühm A. 405 nm versus 633 nm for protoporphyrin IX excitation in fluorescence-guided stereotactic biopsy of brain tumors. J Biophoton. 2016;9:901–912.
3. Theer P, Denk W. On the fundamental imaging-depth limit in two-photon microscopy. J Optical Soc Am A. 2006;23:3139.
4. Dong C-Y, Koenig K, So P. Characterizing point spread functions of two-photon fluorescence microscopy in turbid medium. J Biomed Opt. 2003;8:450.
5. Fixler D, Nayhoz T, Ray K. Diffusion reflection and fluorescence lifetime imaging microscopy study of fluorophore-conjugated gold nanoparticles or nanorods in solid phantoms. ACS Photon. 2014;1:900–905.
6. Wang D, Chen Y, Liu JTC. A liquid optical phantom with tissue-like heterogeneities for confocal microscopy. Biomed Opt Express. 2012;3:3153.
7. König K, Ehlers A, Riemann I, Schenkl S, Bückle R, Kaatz M. Clinical two-photon microendoscopy. Microsc Res Techniq. 2007;70:398–402.
8. Bao H, Allen J, Pattie R, Vance R, Gu M. Fast handheld two-photon fluorescence microendoscope with a 475 μm × 475 μm field of view for in vivo imaging. Opt Lett.2008;33:1333–1335.
9. Kiekens KC, Romano G, Galvez D, et al. Reengineering a falloposcope imaging system for clinical use. Transl Biophoton. 2020;2: e202000011.
10. Weyers BW, Marsden M, Sun T, et al. Fluorescence lifetime imaging for intraoperative cancer delineation in transoral robotic surgery. Transl Biophoton. 2019;1:e201900017.

11. Huizen LMG, Radonic T, Mourik F, et al. Compact portable multiphoton microscopy reveals histopathological hallmarks of unprocessed lung tumor tissue in real time. Transl Biophoton. 2020;2: e202000009.
12. Anastasopoulou M, Koch M, Gorpas D, et al. Comprehensive phantom for interventional fluorescence molecular imaging. J Biomed Opt. 2016;21:091309.
13. Gorpas D, Koch M, Anastasopoulou M, Klemm U, Ntziachristos V. Benchmarking of fluorescence cameras through the use of a composite phantom. J Biomed Opt. 2017;22:016009.
14. Hinsdale T, Olsovsky C, Rico-Jimenez JJ, Maitland KC, Jo JA, Malik BH. Optically sectioned wide-field fluorescence lifetime imaging microscopy enabled by structured illumination. Biomed Opt Express. 2017;8:1455.
15. Markwardt NA, Stepp H, Franz G, et al. Remission spectrometry for blood vessel detection during stereotactic biopsy of brain tumors. J Biophoton. 2017;10:1080–1094.
16. Chen AI, Balter ML, Chen MI, et al. Multilayered tissue mimicking skin and vessel phantoms with tunable mechanical, optical, and acoustic properties. Med Phys.2016; 43:3117–3131.
17. Pinkert MA, Cox BL, Dai B, Hall TJ, Eliceiri KW. 3-D-printed registration phantom for combined ultrasound and optical imaging of biological tissues. Ultrasound Med Biol. 2020;46: 1808–1814.
18. Horng H, O'Brien K, Lamont A, Sochol RD, Pfefer TJ, Chen Y. 3D printed vascular phantoms for high-resolution biophotonic image quality assessment via direct laser writing. Opt Lett.2021;46:1987.
19. Nečas D, Klapetek P. Gwyddion: an open-source software for SPM data analysis. Open Phys. 2012;10.
20. Gwyddion—Free SPM (AFM, SNOM/NSOM, STM, MFM, ⋯) data analysis software. Available from: http://gwyddion.net/download.php#stable-windows. Accessed 12 Aug 2020.
21. Freymüller C, Kalinina S, Rück A, Sroka R, Rühm A. Quenched coumarin derivatives as fluorescence lifetime phantoms for NADH and FAD. J Biophoton. 2021;14:e202100024.
22. Daimon M, Masumura A. Measurement of the refractive index of distilled water from the near-infrared region to the ultraviolet region. Appl Opt. 2007;46:3811.
23. Refractive index of H2O, D2O (Water, heavy water, ice)—Daimon-20.0C. Available from: https://refractiveindex.info/?shelf=main&book=H2O&page=Daimon-20.0C. Accessed 5 Nov 2020.
24. Sultanova NG, Kasarova SN, Nikolov ID. Characterization of optical properties of optical polymers. Optical Quantum Electron. 2013;45:221–232.
25. Refractive index of (C8H8)n (Polystyrene, PS)—Sultanova. Available from https://refractiveindex.info/?shelf=organic&book=polystyren&page=Sultanova. Accessed 8 Aug 2020.
26. Mie G. Beiträge zur Optik trüber Medien, speziell kolloidaler Metallösungen. Annalen der Physik. 1908;330:377–445.
27. Maetzler's MATLAB code for Mie theory. Available from https://omlc.org/software/mie/. Accessed 23 Aug 2019.
28. Bohren CF, Huffman DR. Absorption and scattering of light by small particles. 1st ed.Wiley; 1998.
29. Eisel M, Ströbl S, Pongratz T, Stepp H, Rühm A, Sroka R. Investigation of optical properties of dissected and homogenized biological tissue. J Biomed Opt. 2018;23:1.
30. Lemaillet P, Bouchard J-P, Hwang J, Allen DW. Double-integrating-sphere system at the national institute of standards and technology in support of measurement standards for the determination of optical properties of tissue-mimicking phantoms. J Biomed Opt. 2015;20:121310.
31. Bashkatov AN, Genina ÉA, Kochubey VI, et al. Optical properties of mucous membrane in the spectral range 350-2000 nm. Opt Spectrosc. 2004;97:978–983.
32. Tuchin VV. Tissue optics: light scattering methods and instruments for medical diagnosis. Bellingham, WA: SPIE; 2015.
33. Rohatgi A. Webplotdigitizer: Version 4.3; 2020. Available from: https://automeris.io/WebPlotDigitizer/index.htm.
34. Durr NJ, Weisspfennig CT, Holfeld BA, Ben-Yakar A. Maximum imaging depth of two-photon autofluorescence microscopy in epithelial tissues. J Biomed Opt. 2011;16:026008.
35. Schindelin J, Arganda-Carreras I, Frise E, et al. Fiji: an open-source platform for biological-image analysis. Nat Methods.2012;9:676–682.
36. Berrocal E, Sedarsky DL, Paciaroni ME, Meglinski IV, Linne MA. Laser light scattering in turbid media part I: experimental and simulated results for the spatial intensity distribution. Opt Express.2007;15:10649.
37. Benedetto JJ, Ferreira PJSG, editors. Modern sampling theory. Boston: Birkhäuser; 2001.
38. Young MD, Field JJ, Sheetz KE, Bartels RA, Squier J. A pragmatic guide to multiphoton microscope design. Adv Opt Photon. 2015;7:276.
39. Amos B, McConnell G, Wilson T. 2.2 confocal microscopy. In: Comprehensive biophysics, Elsevier; 2012. p. 3–23.
40. Dunn AK, Wallace VP, Coleno M, Berns MW, Tromberg BJ. Influence of optical properties on two-photon fluorescence imaging in turbid samples. Appl Opt.2000;39:1194.
41. Wang T, Chen J, Zhou T, Song L. Fabricating microstructures on glass for microfluidic chips by glass molding process. Micromachines. 2018;9:269.
42. Hülsenberg D, Harnisch A, Bismarck A. Microstructuring of glasses; Vol 87 of *Springer Series in Materials Science*. Berlin, Heidelberg: Springer; 2008.
43. Harinarayana V, Shin YC. Two-photon lithography for three-dimensional fabrication in micro/nanoscale regime: a comprehensive review. Opt Laser Technol. 2021;142:107180.
44. Talbot CB, Patalay R, Munro I, et al. Application of ultrafast gold luminescence to measuring the instrument response function for multispectral multiphoton fluorescence lifetime imaging. Opt Express.2011;19:13848.
45. Kalinina S, Bisinger D, Breymayer J, Rück A. Cell metabolism, FLIM and PLIM and applications. In: Periasamy A, So PTC, König K, editors. Multiphoton microscopy in the biomedical sciences XV. Vol. 9329. San Francisco, CA: International Society for Optics and Photonics SPIE; 2015. p. 39–43.
46. Kalinina S, Freymueller C, Naskar N, et al. Bioenergetic alterations of metabolic redox coenzymes as NADH, FAD and FMN by means of fluorescence lifetime imaging techniques. Int J Mol Sci. 2021;22:5952.
47. Prahl SA, Gemert MJC, Welch AJ. Determining the optical properties of turbid media by using the adding-doubling method. Appl Opt.1993;32:559.
48. Gioffredi E, Boffito M, Calzone S, et al. Pluronic F127 hydrogel characterization and biofabrication in cellularized constructs for tissue engineering applications. Proc CIRP. 2016;49:125–132.
49. Suntornnond R, Tan EYS, An J, Chua CK. A highly printable and biocompatible hydrogel composite for direct printing of soft and perfusable vasculature-like structures. Sci Reports. 2017;7: 16902.
50. Schmolka IR. Artificial skin I. Preparation and properties of pluronic F-127 gels for treatment of burns. J Biomed Mater Res. 1972;6:571–582.
51. Nishimura G, Awasthi K, Furukawa D. Fluorescence lifetime measurements in heterogeneous scattering medium. J Biomed Opt. 2016;21:075013.
52. Waidelich R, Stepp H, Baumgartner R, Weninger E, Hofstetter A, Kriegmair M. Clinical experience with 5-aminolevulinic acid and photodynamic therapy for refractory superficial bladder cancer. J Urol. 2001;165:1904–1907.

53. Stummer W, Stepp H, Möller G, Ehrhardt A, Leonhard M, Reulen HJ. Technical principles for protoporphyrin-IX-fluorescence guided microsurgical resection of malignant Glioma tissue. Acta Neurochirurgica.1998;140:995–1000.
54. Stepp H, Stummer W. 5-ALA in the management of malignant glioma. Lasers Surgery Med. 2018;50:399–419.
55. Kulcke A, Holmer A, Wahl P, Siemers F, Wild T, Daeschlein G. A compact hyperspectral camera for measurement of perfusion parameters in medicine. Biomed Eng/Biomedizinische Technik. 2018;63:519–527.

How to cite this article: Freymüller C, Ströbl S, Aumiller M, Eisel M, Sroka R, Rühm A. Development of a microstructured tissue phantom with adaptable optical properties for use with microscopes and fluorescence lifetime imaging systems. Lasers Surg Med. 2022;1–17. https://doi.org/10.1002/lsm.23556

6 Literatur

[1] O. Warburg, K. Posener und E. Negelein, "Über den Stoffwechsel der Carcinomzelle", *Biochemische Zeitschrift*, Nr. 152, S. 309–344, 1924.

[2] B. Alberts, A. Johnson, J. H. Lewis, D. Morgan, M. C. Raff, R. Keith, P. Walter und U. Schäfer, *Molekularbiologie der Zelle*. Wiley & Sons, Incorporated, John, 2017, S. 1676, OCLC: 984237313, ISBN: 978-3-527-69845-5.

[3] J. M. Berg, J. L. Tymoczko, G. J. Gatto jr. und L. Stryer, *Stryer Biochemie*. Springer-Verlag GmbH, 5. Dez. 2017, 1401 S., ISBN: 9783662546208.

[4] J. R. Lakowicz, *Principles of fluorescence spectroscopy*, 3rd ed. New York: Springer, 2006, 954 S., ISBN: 978-0-387-31278-1.

[5] K. König, "Clinical multiphoton tomography", *Journal of Biophotonics*, Jg. 1, Nr. 1, S. 13–23, 2008. DOI: https://doi.org/10.1002/jbio.200710022.

[6] M. C. Skala, K. M. Riching, A. Gendron-Fitzpatrick, J. Eickhoff, K. W. Eliceiri, J. G. White und N. Ramanujam, "*In vivo* multiphoton microscopy of NADH and FAD redox states, fluorescence lifetimes, and cellular morphology in precancerous epithelia", *Proceedings of the National Academy of Sciences*, Jg. 104, Nr. 49, S. 19 494–19 499, 2007. DOI: 10.1073/pnas.0708425104.

[7] C. Stringari, A. Cinquin, O. Cinquin, M. A. Digman, P. J. Donovan und E. Gratton, "Phasor approach to fluorescence lifetime microscopy distinguishes different metabolic states of germ cells in a live tissue", *Proceedings of the National Academy of Sciences*, Jg. 108, Nr. 33, S. 13 582–13 587, 2011. DOI: 10.1073/pnas.1108161108.

[8] S. R. Alam, H. Wallrabe, Z. Svindrych, A. K. Chaudhary, K. G. Christopher, D. Chandra und A. Periasamy, "Investigation of Mitochondrial Metabolic Response to Doxorubicin in Prostate Cancer Cells: An NADH, FAD and Tryptophan FLIM Assay", *Scientific Reports*, Jg. 7, Nr. 1, S. 10 451, 2017. DOI: 10.1038/s41598-017-10856-3.

[9] S. Kalinina, C. Freymüller, N. Naskar, B. von Einem, K. Reess, R. Sroka und A. Rück, "Bioenergetic alterations of metabolic redox coenzymes as NADH, FAD and FMN by means of fluorescence lifetime imaging techniques", *International Journal of Molecular Sciences*, Jg. 22, Nr. 11, S. 5952, 31. Mai 2021. DOI: 10.3390/ijms22115952.

[10] A. J. Walsh und M. C. Skala, "Optical metabolic imaging quantifies heterogeneous cell populations", *Biomed. Opt. Express*, Jg. 6, Nr. 2, S. 559–573, Feb. 2015. DOI: 10.1364/BOE.6.000559.

[11] S. Ranjit, L. Malacrida, M. Stakic und E. Gratton, "Determination of the metabolic index using the fluorescence lifetime of free and bound nicotinamide adenine dinucleotide using the phasor approach", *Journal of Biophotonics*, Jg. 12, Nr. 11, e201900156, 2019. DOI: https://doi.org/10.1002/jbio.201900156.

[12] V. V. Tuchin, *Tissue Optics: Light Scattering Methods and Instruments for Medical Diagnosis*. Society of Photo-Optical Instrumentation Engineers (SPIE), Jan. 2015, S. 1–935. DOI: 10.1117/3.1003040.

[13] B. W. Pogue und M. S. Patterson, "Review of tissue simulating phantoms for optical spectroscopy, imaging and dosimetry", *Journal of Biomedical Optics*, Jg. 11, Nr. 4, S. 1–16, 2006. DOI: 10.1117/1.2335429.

[14] A. J. W. G. Visser, "Kinetics of stacking interactions in flavin adenine dinucleotide from time-resolved flavin fluorescence", *Photochemistry and Photobiology*, Jg. 40, Nr. 6, S. 703–706, 1984. DOI: https://doi.org/10.1111/j.1751-1097.1984.tb04640.x.

[15] P. A. W. van den Berg, K. A. Feenstra, A. E. Mark, H. J. C. Berendsen und A. J. W. G. Visser, "Dynamic conformations of flavin adenine dinucleotide: Simulated molecular dynamics of the flavin cofactor related to the time-resolved fluorescence characteristics", *The Journal of Physical Chemistry B*, Jg. 106, Nr. 34, S. 8858–8869, 1. Aug. 2002, Publisher: American Chemical Society. DOI: 10.1021/jp020356s.

[16] M. S. Islam, M. Honma, T. Nakabayashi, M. Kinjo und N. Ohta, "pH Dependence of the Fluorescence Lifetime of FAD in Solution and in Cells", *International Journal of Molecular Sciences*, Jg. 14, Nr. 1, S. 1952–1963, 2013. DOI: 10.3390/ijms14011952.

[17] T. M. Cannon, J. L. Lagarto, B. T. Dyer, E. Garcia, D. J. Kelly, N. S. Peters, A. R. Lyon, P. M. W. French und C. Dunsby, "Characterization of NADH fluorescence properties under one-photon excitation with respect to temperature, pH, and binding to lactate dehydrogenase", *OSA Continuum*, Jg. 4, Nr. 5, S. 1610–1625, Mai 2021. DOI: 10.1364/OSAC.423082.

[18] S. Ogikubo, T. Nakabayashi, T. Adachi, M. S. Islam, T. Yoshizawa, M. Kinjo und N. Ohta, "Intracellular pH Sensing Using Autofluorescence Lifetime Microscopy", *The Journal of Physical Chemistry B*, Jg. 115, Nr. 34, S. 10 385–10 390, 2011, PMID: 21776989. DOI: 10.1021/jp2058904.

[19] T. Kellerer, J. Janusch, C. Freymüller, A. Rühm, R. Sroka und T. Hellerer, "Comprehensive Investigation of Parameters Influencing Fluorescence Lifetime Imaging Microscopy in Frequency- and Time-Domain Illustrated by Phasor Plot Analysis", *International Journal of Molecular Sciences*, Jg. 23, Nr. 24, 2022. DOI: 10.3390/ijms232415885.

[20] A. N. Bashkatov, É. A. Genina, V. I. Kochubey, V. V. Tuchin, E. É. Chikina, A. B. Knyazev und O. V. Mareev, "Optical properties of mucous membrane in the spectral range 350–2000 nm", *Optics and Spectroscopy*, Jg. 97, Nr. 6, S. 978–983, 1. Dez. 2004. DOI: 10.1134/1.1843961.

[21] C. F. Bohren und D. R. Huffman, "Appendix A: Homogeneous Sphere", in *Absorption and Scattering of Light by Small Particles*. John Wiley & Sons, Ltd, 1998, S. 477–482, ISBN: 9783527618156. DOI: https://doi-org.emedien.ub.uni-muenchen.de/10.1002/9783527618156.app2. eprint: https://onlinelibrary-wiley-com.emedien.ub.uni-muenchen.de/doi/pdf/10.1002/9783527618156.app2.

[22] *Maetzler's matlab code for mie theory*, https://omlc.org/software/mie/, Accessed: 2019-08-23.

[23] G. Mie, "Beiträge zur Optik trüber Medien, speziell kolloidaler Metallösungen", *Annalen der Physik*, Jg. 330, Nr. 3, S. 377–445, 1. Jan. 1908, Publisher: John Wiley & Sons, Ltd. DOI: 10.1002/andp.19083300302.

[24] JenLab GmbH. MPT*flex* Flexible in-vivo multiphoton tomography. Zugriff am 18.02.2021, Adresse: https://jenlab.de/wp-content/uploads/2020/10/Multiphoton_-_Tomograph_-_MPTflex_-_JenLab_-_Prism_AwardB.pdf.

[25] P. Leisching und L. Schlag. Förderinitiative „Photonische Systemlösungen für Medizin und Biotechnologie (PSL)", Endoskopisches, optisches Imaging von Zellmetabolismus und Sauerstoffkonzentration für Diagnostik,Therapiemonitoring und Therapiekontrolle (OMOXI). Zugriff: 03.10.2022, Adresse: https://www.photonikforschung.de/media/lebenswissenschaften/pdf/OMOXI-Systeml%C3%B6sungen-Projektsteckbrief-Korr2021-06-bf-C1.pdf.

[26] B. Chance, B. Schoener, R. Oshino, F. Itshak und Y. Nakase, "Oxidation-reduction ratio studies of mitochondria in freeze-trapped samples. NADH and flavoprotein fluorescence signals.", *Journal of Biological Chemistry*, Jg. 254, Nr. 11, S. 4764–4771, 10. Juni 1979, Publisher: Elsevier. DOI: 10.1016/S0021-9258(17)30079-0.

[27] J. R. Lakowicz, H. Szmacinski, K. Nowaczyk und M. L. Johnson, "Fluorescence lifetime imaging of free and protein-bound NADH.", *Proceedings of the National Academy of Sciences*, Jg. 89, Nr. 4, S. 1271–1275, Feb. 1992. DOI: 10.1073/pnas.89.4.1271.

[28] S. Kalinina, D. Bisinger, J. Breymayer und A. Rück, "Cell metabolism, FLIM and PLIM and applications", in *Multiphoton Microscopy in the Biomedical Sciences XV*, A. Periasamy, P. T. C. So und K. König, Hrsg., International Society for Optics und Photonics, Bd. 9329, SPIE, 2015, S. 39–43. DOI: 10.1117/12.2079166.

[29] M. A. Yaseen, J. Sutin, W. Wu, B. Fu, H. Uhlirova, A. Devor, D. A. Boas und S. Sakadžić, "Fluorescence lifetime microscopy of NADH distinguishes alterations in cerebral metabolism in vivo", *Biomed. Opt. Express*, Jg. 8, Nr. 5, S. 2368–2385, Mai 2017. DOI: 10.1364/BOE.8.002368.

[30] T. Hinsdale, C. Olsovsky, J. J. Rico-Jimenez, K. C. Maitland, J. A. Jo und B. H. Malik, "Optically sectioned wide-field fluorescence lifetime imaging microscopy enabled by structured illumination", *Biomed. Opt. Express*, Jg. 8, Nr. 3, S. 1455–1465, März 2017. DOI: 10.1364/BOE.8.001455.

[31] N. Nakashima, K. Yoshihara, F. Tanaka und K. Yagi, "Picosecond fluorescence lifetime of the coenzyme of D-amino acid oxidase.", *Journal of Biological Chemistry*, Jg. 255, Nr. 11, S. 5261–5263, 1980. DOI: https://doi.org/10.1016/S0021-9258(19)70779-0.

[32] D. Chorvat und A. Chorvatova, "Spectrally resolved time-correlated single photon counting: A novel approach for characterization of endogenous fluorescence in isolated cardiac myocytes", *European Biophysics Journal*, Jg. 36, Nr. 1, S. 73–83, 1. Dez. 2006. DOI: 10.1007/s00249-006-0104-4.

[33] N. Boens, W. Qin, N. Basarić, J. Hofkens, M. Ameloot, J. Pouget, J.-P. Lefèvre, B. Valeur, E. Gratton, M. vandeVen, N. D. Silva, Y. Engelborghs, K. Willaert, A. Sillen, G. Rumbles, D. Phillips, A. J. W. G. Visser, A. van Hoek, J. R. Lakowicz, H. Malak, I. Gryczynski, A. G. Szabo, D. T. Krajcarski, N. Tamai und A. Miura, "Fluorescence lifetime standards for time and frequency domain fluorescence spectroscopy", *Analytical Chemistry*, Jg. 79, Nr. 5, S. 2137–2149, 1. März 2007, Publisher: American Chemical Society. DOI: 10.1021/ac062160k.

[34] F. Erdmann, C. Spix, A. Katalinic, M. Christ, J. Folkerts, J. Hansmann, K. Kranzhöfer, B. Kunz, K. Manegold, A. Penzkofer, K. Treml, G. Vollmer, S. Weg-Remers, B. Barnes, N. Buttmann-Schweiger, S. Dahm, J. Fiebig, M. Franke, I. Gurung-Schönfeld, J. Haberland, M. Imhoff, K. Kraywinkel, A. Starker, P. von Berenberg-Gossler und A. Wienecke, *Krebs in deutschland für 2017/2018*, 2021. DOI: http://dx.doi.org/10.25646/8353.

[35] S. Shah-Becker, "Operative management of benign nonepithelial solid laryngeal tumors", *Operative Techniques in Otolaryngology-Head and Neck Surgery*, Jg. 30, Nr. 4, S. 269–272, 1. Dez. 2019. DOI: 10.1016/j.otot.2019.09.009.

[36] Leitlinienprogramm Onkologie (Deutsche Krebsgesellschaft, Deutsche Krebshilfe, AWMF): S3-Leitlinie Diagnostik und Therapie des Mundhöhlenkarzinoms, Kurzversion 3.0, 2021, AWMF Registernummer: 007/100OL. Zugriff am 07.02.2022, Adresse: https://www.leitlinienprogramm-onkologie.de/leitlinien/mundhoehlenkarzinom/.

[37] J.-P. Machiels, C. René Leemans, W. Golusinski, C. Grau, L. Licitra und V. Gregoire, "Squamous cell carcinoma of the oral cavity, larynx, oropharynx and hypopharynx: EHNS–ESMO–ESTRO clinical practice guidelines for diagnosis, treatment and follow-up†", *Annals of Oncology*, Jg. 31, Nr. 11, S. 1462–1475, 1. Nov. 2020. DOI: 10.1016/j.annonc.2020.07.011.

[38] Leitlinienprogramm Onkologie (Deutsche Krebsgesellschaft, Deutsche Krebshilfe, AWMF): Diagnostik, Therapie und Nachsorge des Larynxkarzinoms, Kurzversion 1.1 – Januar 2019, AWMF-Registernummer: 017 - 076OL. Zugriff am 07.02.2022, Adresse: http://www.leitlinienprogramm-onkologie.de/leitlinien/larynxkarzinom/.

[39] Leitlinienprogramm Onkologie (Deutsche Krebsgesellschaft, Deutsche Krebshilfe, AWMF): Diagnostik, Therapie und Nachsorge des Larynxkarzinoms, Langversion 1.1, 2019, AWMF-Registernummer: 017/076OL. Zugriff am 06.04.2022, Adresse: http://www.leitlinienprogramm-onkologie.de/leitlinien/larynxkarzinom/.

[40] Leitlinienprogramm Onkologie (Deutsche Krebsgesellschaft, Deutsche Krebshilfe, AWMF): S3-Leitlinie Diagnostik und Therapie des Mundhöhlenkarzinoms, Langversion 3.0, 2021, AWMF Registernummer: 007/100OL. Zugriff am 06.04.2022, Adresse: https://www.leitlinienprogramm-onkologie.de/leitlinien/mundhoehlenkarzinom/.

[41] A. Watanabe, H. Tsujie, M. Taniguchi, M. Hosokawa, M. Fujita und S. Sasaki, "Laryngoscopic detection of pharyngeal carcinoma in situ with narrowband imaging:" *The Laryngoscope*, Jg. 116, Nr. 4, S. 650–654, Apr. 2006. DOI: 10.1097/01.mlg.0000204304.38797.34.

[42] A. Watanabe, M. Taniguchi, H. Tsujie, M. Hosokawa, M. Fujita und S. Sasaki, "The value of narrow band imaging for early detection of laryngeal cancer", *European Archives of Oto-Rhino-Laryngology*, Jg. 266, Nr. 7, S. 1017–1023, 1. Juli 2009. DOI: 10.1007/s00405-008-0835-1.

[43] C. Arens, C. Betz, M. Kraft und S. Voigt-Zimmermann, "„Narrow band imaging" zur Früherkennung epithelialer Dysplasien und mikroinvasiver Karzinome im oberen Luft-Speise-Weg", *HNO*, Jg. 64, Nr. 1, S. 19–26, Jan. 2016. DOI: 10.1007/s00106-015-0108-4.

[44] C. Simões, M. Durazzo, F. de Aquino Xavier, M. C. Gallottini, S. Lourenço, D. S. Pinto Júnior, N. Magacho de Andrade, A. Miazaki, R. Dedivitis und C. Cernea, "Lugol chromoscopy in the follow-up of head and neck carcinoma", *Annals of Maxillofacial Surgery*, Jg. 7, Nr. 2, S. 188, 2017. DOI: 10.4103/ams.ams_95_17.

[45] C. Betz, M. Mehlmann, K. Rick, H. Stepp, G. Grevers, R. Baumgartner und A. Leunig, "Autofluorescence imaging and spectroscopy of normal and malignant mucosa in patients with head and neck cancer", *Lasers in Surgery and Medicine*, Jg. 25, Nr. 4, S. 323–334, 1999. DOI: https://doi.org/10.1002/(SICI)1096-9101(1999)25:4<323::AID-LSM7>3.0.CO;2-P.

[46] R. Saetti, F. Derosas, M. Silvestrini und S. Narne, "Efficacy of autofluoroscence videoendoscopy in the diagnosis of laryngeal lesions.", *Acta otorhinolaryngologica Italica : organo ufficiale della Societa italiana di otorinolaringologia e chirurgia cervico-facciale*, Jg. 27, Nr. 4, S. 181–185, Aug. 2007.

[47] W. B. Armstrong, J. M. Ridgway, D. E. Vokes, S. Guo, J. Perez, R. P. Jackson, M. Gu, J. Su, R. L. Crumley, T. Y. Shibuya, U. Mahmood, Z. Chen und B. J. F. Wong, "Optical coherence tomography of laryngeal cancer:" *The Laryngoscope*, Jg. 116, Nr. 7, S. 1107–1113, Juli 2006. DOI: 10.1097/01.mlg.0000217539.27432.5a.

[48] A. Sepehr, W. B. Armstrong, S. Guo, J. Su, J. Perez, Z. Chen und B. J. Wong, "Optical coherence tomography of the larynx in the awake patient", *Otolaryngology–Head and Neck Surgery*, Jg. 138, Nr. 4, S. 425–429, Apr. 2008. DOI: 10.1016/j.otohns.2007.12.005.

[49] N. Davaris, S. Voigt-Zimmermann, A.-M. Cyran und C. Arens, "Endoskopische Frühdiagnostik von Karzinomen im oberen Aerodigestivtrakt", *Laryngo-Rhino-Otologie*, Jg. 97, Nr. 4, S. 276–286, Apr. 2018. DOI: 10.1055/a-0575-3564.

[50] M. Goncalves, M. Aubreville, S. K. Mueller, M. Sievert, A. Maier, H. Iro und C. Bohr, "Probe-based confocal laser endomicroscopy in detecting malignant lesions of vocal folds", *Acta Otorhinolaryngologica Italica*, Jg. 39, Nr. 6, S. 389–395, Dez. 2019. DOI: 10.14639/0392-100X-2121.

[51] J. D. Brierley, M. K. Gospodarowicz, C. Wittekind und J. D. Brierley, *TNM Classification of Malignant Tumours*. John Wiley & Sons, Incorporated, 2017, ISBN: 978-1-119-26356-2.

[52] J. Shah, "Endoscopy through the ages", *BJU International*, Jg. 89, Nr. 7, S. 645–652, 1. Mai 2002, Publisher: John Wiley & Sons, Ltd. DOI: 10.1046/j.1464-410X.2002.02726.x.

[53] G. Berci und K. A. Forde, "History of endoscopy", *Surgical Endoscopy*, Jg. 14, Nr. 1, S. 5–15, 1. Jan. 2000. DOI: 10.1007/s004649900002.

[54] C. Saraniti, E. Chianetta, G. Greco, N. Mat Lazim und B. Verro, "The impact of narrow-band imaging on the pre- and intra- operative assessments of neoplastic and preneoplastic laryngeal lesions. a systematic review", *International Archives of Otorhinolaryngology*, Jg. 25, Nr. 3, e471–e478, Juli 2021. DOI: 10.1055/s-0040-1719119.

[55] T. D. Wang und J. Van Dam, "Optical biopsy: A new frontier in endoscopic detection and diagnosis", *Clinical gastroenterology and hepatology : the official clinical practice journal of the American Gastroenterological Association*, Jg. 2, Nr. 9, S. 744–753, Sep. 2004. DOI: 10.1053/S1542-3565(04)00345-3.

[56] C. Betz, V. Volgger, S. Silverman, M. Rubinstein, M. Kraft, C. Arens und B. Wong, "Clinical optical coherence tomography in head & neck oncology: Overview and outlook", *Head and Neck Oncology*, Jg. 5, März 2013.

[57] V. Volgger, S. Girschick, S. Ihrler, A. S. Englhard, H. Stepp und C. S. Betz, "Evaluation of confocal laser endomicroscopy as an aid to differentiate primary flat lesions of the larynx: A prospective clinical study", *Head & Neck*, Jg. 38, Nr. S1, E1695–E1704, 2016. DOI: https://doi.org/10.1002/hed.24303.

[58] D. G. Rey Caro, E. P. Rey Caro und E. A. Rey Caro, "Chromoendoscopy associated with endoscopic laryngeal surgery: A new technique for treating recurrent respiratory papillomatosis", *Journal of Voice*, Jg. 28, Nr. 6, S. 822–829, Nov. 2014. DOI: 10.1016/j.jvoice.2014.02.006.

[59] D. Townsend, F. D'Aiuto und J. Deanfield, "Super actinic 420 nm light-emitting diodes for estimating relative microvascular hemoglobin oxygen saturation", *Journal of Medical and Biological Engineering*, Jg. 34, S. 172–177, Jan. 2014. DOI: 10.5405/jmbe.1643.

[60] A. Bashkatov, E. Genina, V. Kochubey und V. Tuchin, "Optical properties of human skin, subcutaneous and mucous tissues in the wavelength range from 400 to 2000 nm", *Journal of Physics D: Applied Physics*, Jg. 38, Nr. 15, S. 2543–2555, Juli 2005. DOI: 10.1088/0022-3727/38/15/004.

[61] C. Piazza, F. Del Bon, G. Peretti und P. Nicolai, "Narrow band imaging in endoscopic evaluation of the larynx:" *Current Opinion in Otolaryngology & Head and Neck Surgery*, Jg. 20, Nr. 6, S. 472–476, Dez. 2012. DOI: 10.1097/MOO.0b013e32835908ac.

[62] G. Pliske, S. Voigt-Zimmermann, S. Glaßer und C. Arens, "Objective quantification of the vocal fold vascular pattern: Comparison of narrow band imaging and white light endoscopy", *European Archives of Oto-Rhino-Laryngology*, Jg. 273, Nr. 9, S. 2599–2605, 1. Sep. 2016. DOI: 10.1007/s00405-016-4071-9.

[63] C. Arens, D. Reußner, H. Neubacher, J. Woenckhaus und H. Glanz, "Spectrometric measurement in laryngeal cancer", *European Archives of Oto-Rhino-Laryngology and Head & Neck*, Jg. 263, Nr. 11, S. 1001–1007, 1. Nov. 2006. DOI: 10.1007/s00405-006-0099-6.

[64] K. Malzahn, T. Dreyer, H. Glanz und C. Arens, "Autofluorescence endoscopy in the diagnosis of early laryngeal cancer and its precursor lesions", *The Laryngoscope*, Jg. 112, Nr. 3, S. 488–493, 1. März 2002, Publisher: John Wiley & Sons, Ltd. DOI: 10.1097/00005537-200203000-00015.

[65] M. Csanády, J. G. Kiss, L. Iván, J. Jóri und J. Czigner, "ALA (5-aminolevulinic acid)-induced protoporphyrin IX fluorescence in the endoscopic diagnostic and control of pharyngo-laryngeal cancer", *European Archives of Oto-Rhino-Laryngology and Head & Neck*, Jg. 261, Nr. 5, S. 262–266, 1. Mai 2004. DOI: 10.1007/s00405-003-0660-5.

[66] R. Waidelich, H. Stepp, R. Baumgartner, E. Weninger, A. Hofstetter und M. Kriegmair, "Clinical experience with 5-aminolevulinic acid and photodynamic therapy for refractory superficial bladder cancer", *The Journal of Urology*, Jg. 165, Nr. 6, S. 1904–1907, 2001. DOI: https://doi.org/10.1016/S0022-5347(05)66239-8.

[67] P. Jichlinski, M. Forrer, J. Mizeret, T. Glanzmann, D. Braichotte, G. Wagniéres, G. Zimmer, L. Guillou, F. Schmidlin, P. Graber, H. van den Bergh und H.-J. Leisinger, "Clinical evaluation of a method for detecting superficial transitional cell carcinoma of the bladder by light-induced fluorescence of protoporphyrin IX following topical application of 5-aminolevulinic acid: Preliminary results", *Lasers in Surgery and Medicine*, Jg. 20, Nr. 4, S. 402–408, 1997. DOI: https://doi.org/10.1002/(SICI)1096-9101(1997)20:4<402::AID-LSM5>3.0.CO;2-U.

[68] M. Przygoda und D. Aebisher, "Bladder cancer and fluorescence cystoscopy", *Biology and Life Sciences Forum*, Jg. 12, Nr. 1, 2022. DOI: 10.3390/IECN2022-12402.

[69] M. Rubinstein, E. L. Fine, A. Sepehr, W. B. Armstrong, R. L. Crumley, J. H. Kim, Z. Chen und B. J. F. Wong, "Optical coherence tomography of the larynx using the Niris system", *Journal of otolaryngology - head & neck surgery = Le Journal d'oto-rhino-laryngologie et de chirurgie cervico-faciale*, Jg. 39, Nr. 2, S. 150–156, Apr. 2010.

[70] G. J. Tearney, M. E. Brezinski, B. E. Bouma, S. A. Boppart, C. Pitris, J. F. Southern und J. G. Fujimoto, "In vivo endoscopic optical biopsy with optical coherence tomography", *Science*, Jg. 276, Nr. 5321, S. 2037–2039, 1997. DOI: 10.1126/science.276.5321.2037.

[71] M. R. Munk, H. Giannakaki-Zimmermann, L. Berger, W. Huf, A. Ebneter, S. Wolf und M. S. Zinkernagel, "OCT-angiography: A qualitative and quantitative comparison of 4 OCT-a devices", *PLOS ONE*, Jg. 12, Nr. 5, e0177059, 10. Mai 2017, Publisher: Public Library of Science. DOI: 10.1371/journal.pone.0177059.

[72] V. Volgger, G. K. Sharma, J. C. Jing, Y.-S. A. Peaks, A. C. Loy, F. Lazarow, A. Wang, Y. Qu, E. Su, Z. Chen, G. S. Ahuja und B. J.-F. Wong, "Long-range fourier domain optical coherence tomography of the pediatric subglottis", *International Journal of Pediatric Otorhinolaryngology*, Jg. 79, Nr. 2, S. 119–126, 2015. DOI: https://doi.org/10.1016/j.ijporl.2014.11.019.

[73] A. S. Englhard, T. Betz, V. Volgger, E. Lankenau, G. J. Ledderose, H. Stepp, C. Homann und C. S. Betz, "Intraoperative assessment of laryngeal pathologies with optical coherence tomography integrated into a surgical microscope", *Lasers in Surgery and Medicine*, Jg. 49, Nr. 5, S. 490–497, 2017. DOI: https://doi.org/10.1002/lsm.22632.

[74] L. Wittig, C. Betz und D. Eggert, "Optical coherence tomography for tissue classification of the larynx in an outpatient setting-a translational challenge on the verge of a resolution?", *Translational Biophotonics*, Jg. 3, Nr. 1, e202000013, 2021. DOI: https://doi.org/10.1002/tbio.202000013.

[75] A. Englhard, S. Girschick, B. Mack, V. Volgger, O. Gires, C. Conderman, H. Stepp und C. S. Betz, "Probe-based confocal laser endomicroscopy in head and neck malignancies: Early preclinical experience", in *Head and Neck Optical Diagnostics*, Optica Publishing Group, 2013, S. 880 506.

[76] P. S. Thong, M. C. Olivo, R. Bhuvaneswari, S. S. Tandjung, M. M. Movania, W.-M. Chiew, H.-S. Seah, F. Lin, K. Qian und K.-C. Soo, "Toward real-time virtual biopsy of oral lesions using confocal laser endomicroscopy interfaced with embedded computing", *Journal of Biomedical Optics*, Jg. 17, Nr. 5, S. 1–11, 2012. DOI: 10.1117/1.JBO.17.5.056009.

[77] T. N. Seyfried, R. E. Flores, A. M. Poff und D. P. D'Agostino, "Cancer as a metabolic disease: implications for novel therapeutics", *Carcinogenesis*, Jg. 35, Nr. 3, S. 515–527, Dez. 2013. DOI: 10.1093/carcin/bgt480.

[78] T. Seyfried, "Cancer as a mitochondrial metabolic disease", *Frontiers in Cell and Developmental Biology*, Jg. 3, 2015. DOI: 10.3389/fcell.2015.00043.

[79] A. M. Otto, "Warburg effect(s)—a biographical sketch of Otto Warburg and his impacts on tumor metabolism", *Cancer & Metabolism*, Jg. 4, Nr. 1, S. 5, 8. März 2016. DOI: 10.1186/s40170-016-0145-9.

[80] S. Devic, "Warburg effect - a consequence or the cause of carcinogenesis?", *Journal of Cancer*, Jg. 7, Nr. 7, S. 817–822, 2016. DOI: 10.7150/jca.14274.

[81] R. Datta, T. M. Heaster, J. T. Sharick, A. A. Gillette und M. C. Skala, "Fluorescence lifetime imaging microscopy: fundamentals and advances in instrumentation, analysis, and applications", *Journal of Biomedical Optics*, Jg. 25, Nr. 7, S. 1–43, 2020. DOI: 10.1117/1.JBO.25.7.071203.

[82] J. A. Palero, A. N. Bader, H. S. de Bruijn, A. van der Ploeg van den Heuvel, H. J. C. M. Sterenborg und H. C. Gerritsen, "In vivo monitoring of protein-bound and free NADH during ischemia by nonlinear spectral imaging microscopy", *Biomed. Opt. Express*, Jg. 2, Nr. 5, S. 1030–1039, Mai 2011. DOI: 10.1364/BOE.2.001030.

[83] Persönliche Kommunikation AG Rück, 02.08.2022.

[84] A. C. Rück, C. Hauser, S. Mosch und S. Kalinina, "Spectrally resolved fluorescence lifetime imaging to investigate cell metabolism in malignant and nonmalignant oral mucosa cells", *Journal of Biomedical Optics*, Jg. 19, Nr. 9, S. 1–9, 2014. DOI: 10.1117/1.JBO.19.9.096005.

[85] J. P. Villabona-Monsalve, O. Varnavski, B. A. Palfey und T. Goodson, "Two-photon excitation of flavins and flavoproteins with classical and quantum light", *Journal of the American Chemical Society*, Jg. 140, Nr. 44, S. 14 562–14 566, 2018. DOI: 10.1021/jacs.8b08515.

[86] A. J. Walsh, R. S. Cook, H. C. Manning, D. J. Hicks, A. Lafontant, C. L. Arteaga und M. C. Skala, "Optical Metabolic Imaging Identifies Glycolytic Levels, Subtypes, and Early-Treatment Response in Breast Cancer", *Cancer Research*, Jg. 73, Nr. 20, S. 6164–6174, Okt. 2013. DOI: 10.1158/0008-5472.CAN-13-0527.

[87] M. N. Pastore, H. Studier, C. S. Bonder und M. S. Roberts, "Non-invasive metabolic imaging of melanoma progression", *Experimental Dermatology*, Jg. 26, Nr. 7, S. 607–614, 2017. DOI: https://doi.org/10.1111/exd.13274.

[88] C. Stringari, L. Abdeladim, G. Malkinson, P. Mahou, X. Solinas, I. Lamarre, S. Brizion, J.-B. Galey, W. Supatto, R. Legouis, A.-M. Pena und E. Beaurepaire, "Multicolor two-photon imaging of endogenous fluorophores in living tissues by wavelength mixing", *Scientific Reports*, Jg. 7, Nr. 1, S. 3792, 19. Juni 2017. DOI: 10.1038/s41598-017-03359-8.

[89] "Frequency-domain lifetime measurements", in *Principles of Fluorescence Spectroscopy*, J. R. Lakowicz, Hrsg., Boston, MA: Springer US, 2006, S. 157–204, ISBN: 978-0-387-46312-4. DOI: 10.1007/978-0-387-46312-4_5.

[90] A. T. N. Kumar, S. B. Raymond, B. J. Bacskai und D. A. Boas, "Comparison of frequency-domain and time-domain fluorescence lifetime tomography", *Opt. Lett.*, Jg. 33, Nr. 5, S. 470–472, März 2008. DOI: 10.1364/OL.33.000470.

[91] D. Phillips and R.C. Drake and D.V. O'Connor and R.L. Christensen, "Time Correlated Single-Photon Counting (Tcspc) Using Laser Excitation", *Instrumentation Science & Technology*, Jg. 14, Nr. 3-4, S. 267–292, 1985. DOI: 10.1080/10739148508543581.

[92] S. Kalinina, J. Breymayer, P. Schäfer, E. Calzia, V. Shcheslavskiy, W. Becker und A. Rück, "Correlative NAD(P)H-FLIM and oxygen sensing-PLIM for metabolic mapping", *Journal of Biophotonics*, Jg. 9, Nr. 8, S. 800–811, 2016. DOI: https://doi.org/10.1002/jbio.201500297.

[93] W. Becker, *The bh TCSPC Handbook. 9th Edition (2021)*. 2021, https://www.becker-hickl.com/wp-content/uploads/2021/10/SPC-handbook-9ed-05a.pdf.

[94] C. B. Talbot, R. Patalay, I. Munro, S. Warren, F. Ratto, P. Matteini, R. Pini, H. G. Breunig, K. König, A. C. Chu, G. W. Stamp, M. A. A. Neil, P. M. W. French und C. Dunsby, "Application of ultrafast gold luminescence to measuring the instrument response function for multispectral multiphoton fluorescence lifetime imaging", *Opt. Express*, Jg. 19, Nr. 15, S. 13 848–13 861, Juli 2011. DOI: 10.1364/OE.19.013848.

[95] M. I. Rowley, A. C. C. Coolen, B. Vojnovic und P. R. Barber, "Robust Bayesian Fluorescence Lifetime Estimation, Decay Model Selection and Instrument Response Determination for Low-Intensity FLIM Imaging", *PLOS ONE*, Jg. 11, Nr. 6, S. 1–28, Juni 2016. DOI: 10.1371/journal.pone.0158404.

[96] V. Mannam, Y. Zhang, X. Yuan, C. Ravasio und S. Howard, "Machine learning for faster and smarter fluorescence lifetime imaging microscopy", *Journal of Physics: Photonics*, Jg. 2, Nr. 4, S. 042 005, Aug. 2020. DOI: 10.1088/2515-7647/abac1a.

[97] D. Xiao, N. Sapermsap, M. Safar, M. R. Cunningham, Y. Chen und D. D. Li, "On synthetic instrument response functions of time-correlated single-photon counting based fluorescence lifetime imaging analysis", *Frontiers in Physics*, Jg. 9, 2021. DOI: 10.3389/fphy.2021.635645.

[98] PicoQuant. SymPhoTime 64 A software package for cutting edge fluorescence applications. Abgerufen am 24.06.2022, Adresse: https://www.picoquant.com/images/uploads/downloads/symphotime64_brochure.pdf.

[99] J. H. Lee, J. M. Ha und C. H. Leem, "A novel nicotinamide adenine dinucleotide correction method for mitochondrial Ca^{2+}measurement with FURA-2-FF in single permeabilized ventricular myocytes of rat", *The Korean Journal of Physiology & Pharmacology*, Jg. 19, Nr. 4, S. 373–382, 2015. DOI: 10.4196/kjpp.2015.19.4.373.

[100] A. U. Rehman, A. G. Anwer, M. E. Gosnell, S. B. Mahbub, G. Liu und E. M. Goldys, "Fluorescence quenching of free and bound NADH in HeLa cells determined by hyperspectral imaging and unmixing of cell autofluorescence", *Biomedical optics express*, Jg. 8, Nr. 3, S. 1488–1498, 10. Feb. 2017, Publisher: Optical Society of America. DOI: 10.1364/BOE.8.001488.

[101] E. A. Owens, M. Henary, G. El Fakhri und H. S. Choi, "Tissue-specific near-infrared fluorescence imaging", *Accounts of Chemical Research*, Jg. 49, Nr. 9, S. 1731–1740, 2016, PMID: 27564418. DOI: 10.1021/acs.accounts.6b00239.

[102] L. Sordillo, Y. Pu, S. Pratavieira, Y. Budansky und R. Alfano, "Deep optical imaging of tissue using the second and third near-infrared spectral windows", *Journal of biomedical optics*, Jg. 19, S. 56 004, Mai 2014. DOI: 10.1117/1.JBO.19.5.056004.

[103] J. Ying, F. Liu und R. R. Alfano, "Spatial distribution of two-photon-excited fluorescence in scattering media", *Appl. Opt.*, Jg. 38, Nr. 1, S. 224–229, Jan. 1999. DOI: 10.1364/AO.38.000224.

[104] P. Theer und W. Denk, "On the fundamental imaging-depth limit in two-photon microscopy", *J. Opt. Soc. Am. A*, Jg. 23, Nr. 12, S. 3139–3149, Dez. 2006. DOI: 10.1364/JOSAA.23.003139.

[105] N. J. Durr, A. Ben-Yakar, C. T. Weisspfennig und B. A. Holfeld, "Maximum imaging depth of two-photon autofluorescence microscopy in epithelial tissues", *Journal of Biomedical Optics*, Jg. 16, Nr. 2, S. 1–13, 2011. DOI: 10.1117/1.3548646.

[106] M. Oheim, E. Beaurepaire, E. Chaigneau, J. Mertz und S. Charpak, "Two-photon microscopy in brain tissue: Parameters influencing the imaging depth", *Journal of Neuroscience Methods*, Jg. 111, Nr. 1, S. 29–37, 2001. DOI: https://doi.org/10.1016/S0165-0270(01)00438-1.

[107] P. Theer, M. T. Hasan und W. Denk, "Two-photon imaging to a depth of 1000 µm in living brains by use of a Ti:Al_2O_3 regenerative amplifier", *Opt. Lett.*, Jg. 28, Nr. 12, S. 1022–1024, Juni 2003. DOI: 10.1364/OL.28.001022.

[108] F. Helmchen und W. Denk, "Deep tissue two-photon microscopy", *Nature Methods*, Jg. 2, Nr. 12, S. 932–940, 2005. DOI: 10.1038/nmeth818.

[109] M. Göppert-Mayer, "Über Elementarakte mit zwei Quantensprüngen", *Annalen der Physik*, Jg. 401, Nr. 3, S. 273–294, 1931. DOI: https://doi.org/10.1002/andp.19314010303.

[110] W. Kaiser und C. G. B. Garrett, "Two-photon excitation in CaF_2: Eu^{2+}", *Phys. Rev. Lett.*, Jg. 7, S. 229–231, 6 Sep. 1961. DOI: 10.1103/PhysRevLett.7.229.

[111] W. Denk, J. H. Strickler und W. W. Webb, "Two-photon laser scanning fluorescence microscopy", *Science*, Jg. 248, Nr. 4951, S. 73–76, 1990. DOI: 10.1126/science.2321027.

[112] A. Diaspro, G. Chirico und M. Collini, "Two-photon fluorescence excitation and relate techniques in biological microscopy", *Quarterly reviews of biophysics*, Jg. 38, S. 97–166, Juni 2005. DOI: 10.1017/S0033583505004129.

[113] B. N. Ozbay, G. L. Futia, M. Ma, V. M. Bright, J. T. Gopinath, E. G. Hughes, D. Restrepo und E. A. Gibson, "Three dimensional two-photon brain imaging in freely moving mice using a miniature fiber coupled microscope with active axial-scanning", *Scientific Reports*, Jg. 8, Nr. 1, S. 8108, 25. Mai 2018. DOI: 10.1038/s41598-018-26326-3.

[114] A. J. Walsh, R. S. Cook, M. E. Sanders, L. Aurisicchio, G. Ciliberto, C. L. Arteaga und M. C. Skala, "Quantitative Optical Imaging of Primary Tumor Organoid Metabolism Predicts Drug Response in Breast Cancer", *Cancer Research*, Jg. 74, Nr. 18, S. 5184–5194, Sep. 2014. DOI: 10.1158/0008-5472.CAN-14-0663.

[115] V. Di Gialleonardo, D. M. Wilson und K. R. Keshari, "The potential of metabolic imaging.", *Seminars in nuclear medicine*, Jg. 46, Nr. 1, S. 28–39, Jan. 2016. DOI: 10.1053/j.semnuclmed.2015.09.004.

[116] W. Becker, A. Bergmann, A. Jelzow, A. Neubauer, A. Rück, K. Birkmeier und P. Leisching, "Metabolic imaging by simultaneous 2-photon FLIM of NAD(P)H and FAD", in *Multiphoton Microscopy in the Biomedical Sciences XX*, A. Periasamy, P. T. C. So und K. König, Hrsg., International Society for Optics und Photonics, Bd. 11244, SPIE, 2020, S. 1–5. DOI: 10.1117/12.2550962.

[117] C. Freymüller, S. Ströbl, M. Aumiller, M. Eisel, R. Sroka und A. Rühm, "Development of a microstructured tissue phantom with adaptable optical properties for use with microscopes and fluorescence lifetime imaging systems", *Lasers in Surgery and Medicine*, S. 1–17, 2022, Publisher: John Wiley & Sons, Ltd. DOI: 10.1002/lsm.23556.

[118] V. V. Tuchin, *Tissue optics light scattering methods and instruments for medical diagnosis, light scattering methods and instruments for medical diagnosis*. SPIE Press, 2015, S. 934, ISBN: 9781628415162.

[119] M. Eisel, S. Ströbl, T. Pongratz, H. Stepp, A. Rühm und R. Sroka, "Investigation of optical properties of dissected and homogenized biological tissue", *Journal of Biomedical Optics*, Jg. 23, Nr. 9, S. 1–9, 2018. DOI: 10.1117/1.JBO.23.9.091418.

[120] C.-Y. Dong, K. Koenig und P. T. C. So, "Characterizing point spread functions of two-photon fluorescence microscopy in turbid medium", *Journal of Biomedical Optics*, Jg. 8, Nr. 3, S. 450–459, 2003. DOI: 10.1117/1.1578644.

[121] D. Fixler, T. Nayhoz und K. Ray, "Diffusion reflection and fluorescence lifetime imaging microscopy study of fluorophore-conjugated gold nanoparticles or nanorods in solid phantoms", *ACS Photonics*, Jg. 1, Nr. 9, S. 900–905, 2014, PMID: 25541621. DOI: 10.1021/ph500214m.

[122] D. Wang, Y. Chen und J. T. C. Liu, "A liquid optical phantom with tissue-like heterogeneities for confocal microscopy", *Biomed. Opt. Express*, Jg. 3, Nr. 12, S. 3153–3160, Dez. 2012. DOI: 10.1364/BOE.3.003153.

[123] M. Anastasopoulou, M. Koch, D. Gorpas, A. Karlas, U. Klemm, P. B. Garcia-Allende und V. Ntziachristos, "Comprehensive phantom for interventional fluorescence molecular imaging", *Journal of Biomedical Optics*, Jg. 21, Nr. 9, S. 1–10, 2016. DOI: 10.1117/1.JBO.21.9.091309.

[124] D. Gorpas, M. Koch, M. Anastasopoulou, U. Klemm und V. Ntziachristos, "Benchmarking of fluorescence cameras through the use of a composite phantom", *Journal of Biomedical Optics*, Jg. 22, Nr. 1, S. 1–12, 2017. DOI: 10.1117/1.JBO.22.1.016009.

[125] N. A. Markwardt, H. Stepp, G. Franz, R. Sroka, M. Goetz, P. Zelenkov und A. Rühm, "Remission spectrometry for blood vessel detection during stereotactic biopsy of brain tumors", *Journal of Biophotonics*, Jg. 10, Nr. 8, S. 1080–1094, 2017. DOI: https://doi.org/10.1002/jbio.201600193.

[126] A. I. Chen, M. L. Balter, M. I. Chen, D. Gross, S. K. Alam, T. J. Maguire und M. L. Yarmush, "Multilayered tissue mimicking skin and vessel phantoms with tunable mechanical, optical, and acoustic properties", *Medical Physics*, Jg. 43, Nr. 6Part1, S. 3117–3131, 2016. DOI: https://doi.org/10.1118/1.4951729.

[127] C. Freymüller, S. Kalinina, A. Rück, R. Sroka und A. Rühm, "Quenched coumarin derivatives as fluorescence lifetime phantoms for NADH and FAD", *Journal of Biophotonics*, Jg. 14, Nr. 7, e202100024, Apr. 2021. DOI: https://doi.org/10.1002/jbio.202100024.

[128] D. Gonçalves und D. Griffith, "Estimating uncertainty in resolution tests", *Optical Engineering*, Jg. 45, Mai 2006. DOI: 10.1117/1.2202914.

[129] H. Gross, H. Zügge, M. Peschka und F. Blechinger, *Handbook of Optical Systems, Aberration Theory and Correction of Optical Systems*. Wiley-VCH, 2007, S. 780, ISBN: 9783527403790.

[130] G. Jones, W. R. Jackson, C. Y. Choi und W. R. Bergmark, "Solvent effects on emission yield and lifetime for coumarin laser dyes. requirements for a rotatory decay mechanism", *The Journal of Physical Chemistry*, Jg. 89, Nr. 2, S. 294–300, 1985. DOI: 10.1021/j100248a024.

[131] A. S. Kristoffersen, S. R. Erga, B. Hamre und Ø. Frette, "Testing Fluorescence Lifetime Standards using Two-Photon Excitation and Time-Domain Instrumentation: Rhodamine B, Coumarin 6 and Lucifer Yellow", *Journal of Fluorescence*, Jg. 24, Nr. 4, S. 1015–1024, 1. Juli 2014. DOI: 10.1007/s10895-014-1368-1.

[132] O. Stern und M. Volmer, "Über die Abklingungszeit der Fluoreszenz", *Physikalische Zeitschrift*, Nr. 20, S. 183–188, 1919.

[133] M. H. Gehlen, "The centenary of the Stern-Volmer equation of fluorescence quenching: From the single line plot to the SV quenching map", *Journal of Photochemistry and Photobiology C: Photochemistry Reviews*, Jg. 42, S. 100 338, März 2020. DOI: 10.1016/j.jphotochemrev.2019.100338.

[134] S. Kalinina, J. Breymayer, K. Reeß, L. Lilge, A. Mandel und A. Rück, "Correlation of intracellular oxygen and cell metabolism by simultaneous PLIM of phosphorescent TLD1433 and FLIM of NAD(P)H", *Journal of Biophotonics*, Jg. 11, Nr. 10, e201800085, 2018. DOI: https://doi.org/10.1002/jbio.201800085.

[135] H. Stiel, K. Teuchner, A. Paul, D. Leupold und I. E. Kochevar, "Quantitative comparison of excited state properties and intensity-dependent photosensitization by rose bengal", *Journal of Photochemistry and Photobiology B: Biology*, Jg. 33, Nr. 3, S. 245–254, 1996. DOI: https://doi.org/10.1016/1011-1344(95)07248-9.

[136] Y. Sun und A. Periasamy, "Localizing protein–protein interactions in living cells using fluorescence lifetime imaging microscopy", in *Methods in Molecular Biology*, Springer New York, Okt. 2014, S. 83–107. DOI: 10.1007/978-1-4939-2080-8_6.

[137] S.-C. Liao, Y. Sun und U. Coskun, *Flim analysis using the phasor plots*, http://www.iss.com/resources/pdf/technotes/FLIM_Using_Phasor_Plots.pdf, ISS, Inc.1602, Newton Drive, Champaign, IL 61822, 2014.

7 Danksagung

Mit dem Beginn der Doktorarbeit im LIFE-Zentrum 2018 hatte ich die Möglichkeit für viele Gespräche und Diskussionen und habe von verschiedenen Seiten Hilfe und Unterstützung bekommen, ohne die die vorliegende Arbeit nicht möglich gewesen wäre.
Ein spezieller Dank gilt Ronald Sroka als meinem Doktorvater und den im fachlichen wie auch im privaten Umfeld hilfreichen Diskussionen. Ebenso meinem Betreuer, Adrian Rühm. Es war immer eine Freude, mit ihm einem Problem oder einer Fragestellung auf den Grund zu gehen.
Meinen Mit-Dokoranten, Maximilian Eisel, Maximilian Aumiller und Christian Heckl gilt ebenso mein Dank für ihre Unterstützung, Diskussionen und ihre Freundschaft. Ebenso gilt mein Dank den Bachelorstudenten Nico Imberger und Janko Janusch.
Weiterhin möchte ich mich bei Angelika Rück, Sviatlana Kalinina und Kirsten Reess für die Zusammenarbeit, die Möglichkeit das FLIM-Mikroskop ihrer Arbeitsgruppe zu nutzen und für die vielen Diskussionen und die Zeit in Ulm bedanken. Dies wird, trotz Sviatlanas Tod im September 2021, in schöner Erinnerung bleiben.
Neben dem beruflichen gilt mein Dank auch meinem privaten Umfeld. Dieses hat jahrelang zum einen Erzählungen über Physik ertragen, aber ebenso eine permanente Unterstützung und Reflexionsfläche geboten. Meiner Schwester gilt ein ganz besonderer Dank für Ihre Motivation und Unterstützung.

8 Eidesstattliche Versicherung

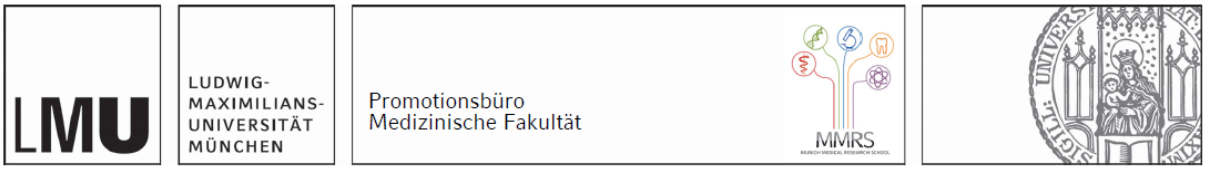

Eidesstattliche Versicherung

Freymüller Christian
Name, Vorname

Ich erkläre hiermit an Eides statt, dass ich die vorliegende Dissertation mit dem Titel:

Untersuchungen zur Standardisierung der Messung mikroskopischer Strukturen hinsichtlich Fluoreszenzlebensdauer und bildgebender Lumineszenz zur endoskopischen Anwendung

selbständig verfasst, mich außer der angegebenen keiner weiteren Hilfsmittel bedient und alle Erkenntnisse, die aus dem Schrifttum ganz oder annähernd übernommen sind, als solche kenntlich gemacht und nach ihrer Herkunft unter Bezeichnung der Fundstelle einzeln nachgewiesen habe.

Ich erkläre des Weiteren, dass die hier vorgelegte Dissertation nicht in gleicher oder in ähnlicher Form bei einer anderen Stelle zur Erlangung eines akademischen Grades eingereicht wurde.

München, 19.12.2022
Ort, Datum

Christian Freymüller
Unterschrift Doktorand